# Molecular Dynamics Simulation of Sputtering

Thesis by

Davy Lo

In Partial Fulfillment of the Requirements
for the Degree of
Doctor of Philosophy

California Institute of Technology
Pasadena, California

1989

(Submitted February 20, 1989)

## Acknowledgement

I like to acknowledge the National Science Foundation and the California Institute of Technology for their part in supporting this work. I would also like to thank the San Diego Super Computer Center and the physics department of California State University at Fullerton for providing access to their computing facility.

I give many thanks to the friends that I made at Caltech who have enriched my life as a graduate student immeasurably. I have learnt a great deal from them, and we also shared many happy hours together. In addition, I would like to specifically thank the Brown Baggers for making our office feel like a home.

I am grateful to my thesis advisor Tom Tombrello for his sagacious guidance and patience throughout some difficult periods of my graduate study. This work would not have been possible without the direction of Mark Shapiro, who introduced me to molecular dynamics. Helpful and enjoyable conversations with Peter Haff have been invaluable. Special thanks to Barbara Garrison and Don Harrison for their guidance and collaboration are also due.

This thesis is dedicated to my parents.

# Abstract

The sputtering of metals by low-energy (keV) ion bombardment has been investigated with the molecular dynamics technique. This study, based on computer simulations, aims to elucidate experimental observations and to provide valuable theoretical insight. The systems studied include $Ar^+$ ion bombardment of metals, alloys, and isotopic mixtures in either the solid or liquid state. Effects of many-body interactions on the spectrum of sputtered atoms were also examined. Simulation results generally support experimental findings and render many basic assumptions of analytic sputtering theory dubious.

This thesis consists of molecular dynamics studies of several sputtering topics not directly related to each other and is organized accordingly into separate chapters. Each of these chapters will be a summary of corresponding publications published by the author during the course of his graduate study. Reprints of publications are included as appendices at the end of each chapter.

# Table of Contents

# Chapter 1 - Introduction

## 1.1 Overview

The field of surface physics and interfacial phenomena in general poses great fascination and challenge for physicists. The physics at interfaces (surfaces are a special case of an interface between a material and a surrounding vapor or vacuum) of materials is responsible for a variety of phenomena around us, ranging from the electrical characteristics of microelectronic devices to erosion and wear of industrial materials. Although enormous progress has been made in the past forty years, we are still only scratching the surface in our understanding of processes at the microscopic surface. In recent years, technological advancements in a variety of fields have depended on our understanding of interfacial phenomena on an atomic scale. The continuing search for smaller and faster devices used in computers, harder and more resilient materials for industrial applications, and more efficient surface catalysis mechanisms in environmental applications, just to name a few, have fueled interest in the interface of materials to unprecedented levels. It is not surprising that interface physics enters into so many areas of applications since the interaction of different materials takes place at the interface. The understanding of interfacial phenomena is both experimentally and theoretically challenging. On the theoretical front, the abrupt discontinuity of periodicity and symmetry at interfaces has imposed limits on powerful analytical techniques that are so triumphant in the field of solid state physics. The structure, composition, and electrical properties near the interfaces are complicated by the interface and various approximate extensions of solid state theory have attempted to explain them, but the theory of interfaces is far from complete. Our theoretical understanding of interfacial modification techniques such as sputtering or ion beam mixing are further complicated by the non-equilibrium nature of the processes making them analytically intractable. These complications make computer simulation a logical complement to analytic techniques. It may be safely said that it will take more than two-dimensional thinking to understand microscopic interfaces/surfaces.

Computational physics is taking on a more important role in all fields of physics, and interfacial physics is no exception. With the recent development of super computers and powerful work stations, it is becoming even more attractive to proceed in this direction. The computer, strictly speaking, is a mathematical tool used to solve intractable analytic equations. The results of a calculation are only as good as the theoretical assumptions and should not be thought of as experimental results. However, computational physics possesses the flavor of experimental uncertainty, hence, the phrase 'computer experiments.' In laboratory experiments one has to worry constantly about unaccounted-for effects that can affect experimental results.

Analogous situations arise on the computer - such as the effects of system or sampling size. A good experiment, as a good computer simulation, must be carefully isolated from unwanted effects that are outside the theory's assumptions. Beyond laboratory experiments, a computer simulation can give information about a process that experimentalists can at best infer indirectly. We can, for example, see the momentum distribution in a group of cascading subsurface atoms, the atomic arrangements in an interface, or the time evolution of atomic positions during phase transitions with computer simulations. With enough care in setting up the computer model, computer simulations can be a powerful tool that compliments theory and experiment by giving guidance to further developments in each. With this philosophy in mind, computer simulation is used here to investigate the surface phenomenon of sputtering, which is the topic of this thesis.

When the surface of a material is bombarded by energetic particles, it undergoes erosion and absorbs energy from the incident particles. Part of the energy absorbed goes to produce damage inside the material, and the rest may be imparted to atoms near the surface. Those atoms near the surface with enough momentum to overcome the surface binding energy will subsequently eject and leave the target. This ejection process is called *sputtering*. The sputtered material may come off as neutral atoms, or as ions in the form of both monomers or multimers. The majority come off as neutral monomers. The number of particles that eject per incident particle is called the *sputtering yield.* Sputtering yields will in general depend on the target material and incident particle characteristics such as energy, mass, and to a lesser extent, charge state. The incident energetic particles may be molecules, atoms, ions, nucleons, electrons, or photons. Much experimental and theoretical effort has been directed towards ion bombardment of metals. Ions with definite mass and energy are relatively easy to produce, and their interaction with the material is well understood.

The atomic displacement mechanism in metals is essentially by atomic (nuclear) collisions [1,2], since the relaxation time of the electrons is too short to drive atomic displacements directly; the electric field produced by electron excitations is quickly compensated for by a redistribution of the electron density before it can cause atomic displacement. Furthermore the excited electrons cannot directly transfer their kinetic energy to nuclear motion because of the extreme mass mismatch between the electron and the nucleus. In insulators, electric fields may exist long enough to cause atomic displacements, so that more than just nuclear collisions are involved. For these reasons, ion bombardments of metals provide ideal systems for studying the basic mechanisms of sputtering. When an ion penetrates a material, it loses energy by two mechanisms, elastic nuclear collision and electron excitation. Because of the extreme electron-nucleus mass mismatch, these two mechanisms are decoupled. At low ion energies the loss is dominated by nuclear collisions (*nuclear stopping regime*), while loss by electron excitation dominates at high ion energies (*electronic stopping regime*). Sputtering of *metals* is more interesting in the nuclear stopping regime since electronic stopping contributes little to atomic displacements and ultimate ejection of atoms. This thesis will deal only with sputtering of metals by ions in the nuclear stopping regime.

From the technological standpoint, sputtering can be an unwanted dirt effect or a powerful tool for surface analysis and modification. Some areas of technological interest in which sputtering plays an important role are listed below [3]:

> Destroys cathodes and grids in discharge tubes while contaminating the plasma and surrounding walls.
>
> Contaminates plasma in tokamaks, and bremsstrahlung involving these heavy sputtered atoms inhibits nuclear fusion.
>
> Destroys accelerator components and damages targets in electron microscopes.
>
> Limits implanted ion concentration that is due to surface layer removal.
>
> Controlled removal of atoms with submicron resolution (ion milling).

Sputtered ion sources that can provide highly clean sources of ions.

Depth profiling of thin films (secondary ion/neutral spectroscopy).

Controlled deposition of atomic layers (thin film deposition).

A basic understanding of sputtering will enhance our ability to control its dirt effects and improve or expand its applications. Of course, sputtering is also an interesting physics problem in its own right.

This thesis consists of molecular dynamics studies of several sputtering topics not directly related to each other and is organized accordingly into separate chapters. Each of these chapters will be a summary of corresponding publications published by the author during the course of his graduate study. Reprints of publications are included as appendices at the end of each chapter. The present chapter gives a basic introduction to the historical, theoretical, experimental, and computational aspects of sputtering. Chapter 2 gives a detailed description of the molecular dynamics code. Subsequent chapters deal with particular topics.

## 1.2 Historical Survey

By general consensus the sputtering phenomenon was first observed by *Grove* in 1853 when he reported a metallic deposit on the glass wall of a discharge tube during his discharging experiments [4]. Early attempts at explaining the phenomenon were focussed on evaporation. It was thought that metal atoms evaporated from the cathode and were due to macroscopic heating by the surrounding gas. This view was later abandoned when it was shown that the sputtering rate was insensitive to the cathode temperature. The cause of the phenomenon was not properly identified until half a century after its discovery when it was shown by *Goldstein* that the metallic deposit came from the cathode and resulted from bombardment by the positive ions generated in the discharge [5].

Around the turn of the century, *Stark* proposed that the impinging ion causes microscopic heating of the region local to the point of impact, resulting in local evaporation from these "hot spots" [6]. The local heating was viewed by Stark as a consequence of a series of binary elastic collisions between atoms initiated by the ion impact. During the first half of this century, although the important role of elastic collisions in sputtering was recognized, the emphasis was on evaporation models; *Hippel* and *Townes* [7].

Modern theories see sputtering as three sequential processes [8,9]. First the impinging ion transfers energy to target atoms through elastic/inelastic collisions. The primary recoils then collide with other atoms and generate a collision cascade. As the collision cascade intersects the surface, atoms with enough energy escape the surface by overcoming surface binding forces. The first two processes are understood in terms of radiation damage in matter. Therefore, it is fair to say that the ground work for modern theoretical understanding of sputtering was laid down by Bohr and others in the first half of this century, during their investigation of the penetration of matter by atomic particles [1]. An excellent exposition of the subject is given in the classic review, *The Penetration of Atomic Particles Through Matter* by Bohr [1].

As collision models developed in the description of radiation damage in the 1950's and 1960's, parallel developments in sputtering theories took place. Linhard, Schariff, and Schiott made significant contributions to our theoretical understanding of ion stopping powers in matter [10]. Their theory was in accord with experimental measurements on ion ranges by *Davies* et al. [11]. Later measurements on the energy dependence of sputtering yields showed a remarkable correlation with the calculated energy dependence of the ion's stopping power; *Brandt* and *Laubert* [12]. The topics of sputtering and ion penetration of matter are closely related. This was first recognized and exploited by *Keywell* when he combined ideas from radiation damage and neutron transport theory [13]. During the same period, inadequacies of the evaporation model were unambiguously demonstrated by *Wehner's* observation of spot patterns produced by atoms sputtered from single crystals [14]. The spot patterns reflected the underlying crystal symmetry, which cannot be explained with any evaporation mechanism. This fueled unprecedented interest in the *collision cascade* [8,9] model and set the stage for its rapid development.

In the late 1950's and early 1960's computers were introduced into the field of radiation damage and sputtering. The molecular dynamics technique was first introduced in 1957 by Alder and Wainwright in the study of hard sphere fluids [15]. First application of molecular dynamics to radiation damage was by Gibson, Goland, Milgram, and Vineyard in 1960, when they also introduced more realistic interaction potentials into the technique [16]. The first use of computer simulation in sputtering was by Harrison [17] in 1959, using a Monte Carlo technique (later this technique developed into what is now known as the *binary collision approximation* or BCA). Later Harrison departed from BCA models and developed the more conservative *molecular dynamics* (MD) approach to sputtering because of his belief that BCA may be neglecting many important mechanisms important for sputtering [18]. Today there exist two schools of sputtering simulators - the BCA and MD schools. The debates generated by these two different approaches go on. For an insightful review on the subject of computer simulations in sputtering see Harrison [18]. Since the introduction of the simulators as a player on the field of sputtering some thirty years ago, they have stimulated heated and animated debates with the analytical theorists. The present situation may be summarized by a quotation taken from a recent review on the subject by Andersen [19] - "Analytical theorists and computer simulists still beat each other's heads."

Today, the generally accepted theory of sputtering is the *linear cascade* model of Sigmund [8]. Sigmund's theory is based upon kinetic transport formalism and is rather mathematically involved. An equivalent theory developed by Thompson [9] gives a succinct description of the simple physical mechanism involved. These theories assume that collisions are binary (ie. an atom collides with only one other atom at a time), and collisions always involve a moving atom and an atom at rest. Therefore, linear cascade theory is limited to dilute *cascade densities* (densities of moving atoms).

The breakdown of the linear cascade theory at high deposition energy densities was clearly demonstrated by the experimental observation of Andersen and Bay [20]. They bombarded gold with $Te^+$ and $Te_2^+$ and found that the molecular ion resulted in a yield (per atom) that was 67% higher than the single ion. Presumably, the $Te_2^+$ breaks up after impact, but the constituent atoms stay close enough to each other, causing a much higher cascade density than the $Te^+$ alone would have initiated. The linear cascade model assumes that atoms in a cascade do not interact with each other and would have predicted equal yields (per atom) for the $Te^+$ and $Te_2^+$ bombardment. This experiment and later ones revived interest in evaporation like models for the regime of high deposition energy densities, now mostly referred to as the *thermal spike regime*. Spike models were developed during the late 1970's, most notably by Kelly and Sigmund [21,22]. These models generally attempted to apply thermodynamic ideas such as temperature and heat conduction to a local "hot spot" created by the ion impact from which the atoms "evaporate". It is questionable that such thermodynamic concepts are even valid for a process that is highly localized (~100 Å) and is taking place over an extremely short time ($10^{-11}$ s.). Although questionable, it is at present the only model that addresses the thermal spike regime and that has had some success in comparison to experiments; Claussen [23].

In many fields of science *fractals* have in recent years given us new dimensionalities to think about, and sputtering/radiation damage is no exception. The mathematical concept of fractal dimensions is being used to illustrate how linear cascades, given enough energy, evolve into spikes [24].

## 1.3 Theoretical Aspects

A major task of all sputtering theories is to predict the sputtering yield for a given set of bombardment parameters. Sputtering yields may be as low as $10^{-5}$ and as high as $10^{+3}$ secondary particles per incident particle [2]. Spanning eight orders of magnitude, it is not surprising that no universal mechanism exists that will explain all sputtering phenomena. What follows will be a brief description of the *linear cascade theory*, which assumes bombarding conditions that are most relevant to this thesis. The discussion will follow that of Thompson [9] with slight deviations reflecting my own perception of the subject.

We start within an infinite isotropic media and assume a constant source of primary recoils generated by a flux of ions. The number of primary recoils with energy $E_1$ generated per unit volume per unit time is $\chi(E_1)\,dE_1$. Assuming binary elastic collisions, this is given by:

$$(1.1) \qquad \chi(E_1)\,dE_1 = n\,J_o\,\frac{d\sigma}{dE_1}(E_0, E_1)\,dE_1,$$

where $\frac{d\sigma}{dE_1}(E_0, E_1)$ is the differential cross section for an ion with initial energy $E_0$ being scattered by a recoiling atom initially at rest, which gains an energy $E_1$ from the ion. $J_o$ is the flux of incoming ions per unit area per unit time, and **n** is the target density. It is also assumed in eq. 1.1 that the ion has a constant stopping power within the region of interest and does not reflect and traverse this region more than once. We want to know the distribution of moving atoms generated by this source in a steady-state situation. The primary recoils collide with other atoms and create higher generations of recoils while losing energy. As primary recoils slow down from an energy of **E'+dE'** to **E'**, additional recoils must be generated at the source to maintain the steady state. So the density of primary recoils at energy **E'** with initial energy $E_1$ is:

$$\rho_1(E_1,E')\, dE_1\, dE' = \chi(E_1)\, dE_1\, dt, \tag{1.2}$$

where **dt** is the average time it takes for a primary recoil to slow down from an energy of **E'+dE'** to **E'** and is given by:

$$dt = \frac{1}{v'\; dE'/dx}\, dE'. \tag{1.3}$$

Here, $\frac{dE'}{dx}$ is the primary recoil's stopping power and **v'** is its velocity. To obtain the density of all moving atoms at energy **E'**, we also need to consider the higher generation recoils generated by the primaries. Consider a cascade of moving atoms initiated by a single primary recoil of energy $E_1$. If we assume on the average that energy is equally partitioned within the cascade, then the average number of moving atoms with energy **E'** generated by each primary recoil of energy $E_1$ will be $kE_1/E'$. **k** is a constant on the order of one. Since the cascade of atoms is in reality not an ideal gas, **k** is somewhat less than one and ranges from .5 to 1.0, but for simplicity will be assumed to be 1.0 in the following discussion. It follows that the density of moving atoms with energy **E'** is given by:

$$(1.4) \qquad \rho(E')\,dE' = \int_{E'}^{\gamma E_0} \frac{E_1}{E'}\,\rho_1(E_1,E')\,dE_1 \;\; dE'$$

$$= \int_{E'}^{\gamma E_0} E_1\,\chi(E_1)\,dE_1 \left(\frac{1}{v'\,E'\,dE'/dx}\,dE'\right).$$

Here, $E_0$ is the incident ion energy, and $\gamma E_0$ is the maximum energy that an incident ion of mass $m_0$ can transfer to a primary recoil atom of mass $m_1$ during a binary elastic collision. The factor $\gamma$ is given by:

$$(1.5) \qquad \gamma = \frac{4\,m_0\,m_1}{(m_0 + m_1)^2}.$$

The majority of sputtered atoms come from high-generation recoils with energy $E' \ll \gamma E_0$, so the integral in (1.4) can be approximated by replacing the lower limit by zero. Combining this approximation with (1.1):

(1.6)

$$\rho(E')\, dE' = J_o \left( n \int_0^{\gamma E_0} E_1 \frac{d\sigma}{dE_1}(E_0,E_1)\, dE_1 \right) \left( \frac{1}{v' E' dE'/dx}\, dE' \right)$$

The first bracketed quantity we recognize as the stopping power of the ion $\frac{dE_0}{dx}$, which depends on the incident ion and target characteristics. The only **E'** dependence is within the second bracketed quantity, which will ultimately determine the relative spectra of sputtered atoms and is independent of the bombarding ion. Bombarding ion characteristics, then, will be relevant only to the absolute sputtering yield within this approximation. Rewriting (1.6):

$$(1.7) \qquad \rho(E')\ dE' = J_o \frac{dE_0/dx}{v'\ E'\ dE'/dx}\ dE'.$$

The self-stopping power of the target atom $\frac{dE'}{dx}$ may be written as:

$$(1.8) \qquad \frac{dE'}{dx} = n \int_0^{E'} T\ \frac{d\sigma}{dT}(E',T)\ dT.$$

$\frac{d\sigma}{dT}(E', T)$ is the differential cross section for an target atom at rest to gain an energy **T** from scattering with another target atom of energy **E'** during a binary collision. The integral may be evaluated by assuming that the atom-atom interaction may be described by a pair potential of the form $\frac{1}{r^s}$. This is known as the power-law approximation, and a generalized Rutherford cross section may be derived:

$$(1.9) \qquad \frac{d\sigma}{dT}(E', T) = \frac{C_m}{E'^m \, T^{m+1}}, \quad m = \frac{1}{s}.$$

Integrating (1.8) gives:

$$(1.10) \qquad \frac{dE'}{dx} = \frac{n \, C_m}{1 - m} E'^{1-2m}.$$

The pair potential parameter **m** varies from 0 for hard spheres to 1 for pure Coulomb collisions. The flux of moving atoms is next assumed to be isotropic and is expressed in terms of the density:

$$(1.11) \qquad J'(E') \, dE' \, d\Omega' = \rho(E') \, v' \, dE' \, \frac{d\Omega'}{4\pi}.$$

Now we introduce a planar surface and assume that it does not appreciably alter the flux. Consider a flux of atoms moving in a direction $\theta'$ as measured from the outward surface normal and in a particular azimuthal direction (Figure 1). The number of atoms with energy **E'** moving in this direction crossing the surface plane per unit area per unit time is:

$$(1.12)\quad J'_n(E',\theta')\,dE'\,d\Omega' = \rho(E')\,v'\,dE'\,\cos\theta'\frac{d\Omega'}{4\pi}.$$

Using (1.7) and (1.10), we obtain the final expression for the flux inside the target:

$$(1.13)\qquad J'_n(E',\theta')\,dE'\,d\Omega'$$

$$= D_m\,J_0\left(\frac{1}{n}\frac{dE_0}{dx}\right)E'^{2(m-1)}\,dE'\,\cos\theta'\frac{d\Omega'}{4\pi}.$$

The constant $D_m = \frac{C_m}{1-m}$ depends only on the potential parameter **m**. So far we have neglected the binding energy between the atoms. The binding force between atoms will alter the energy and direction of atoms as they eject from the surface. This effect will be approximated by introducing a planar surface potential barrier of energy $E_b$. A planar surface potential by definition only produces forces that are normal to the surface. Let an atom with energy **E'**, and moving in a direction $\theta'$ have corresponding values of **E** and $\theta$ after traversing the planar potential barrier (Figure 1).

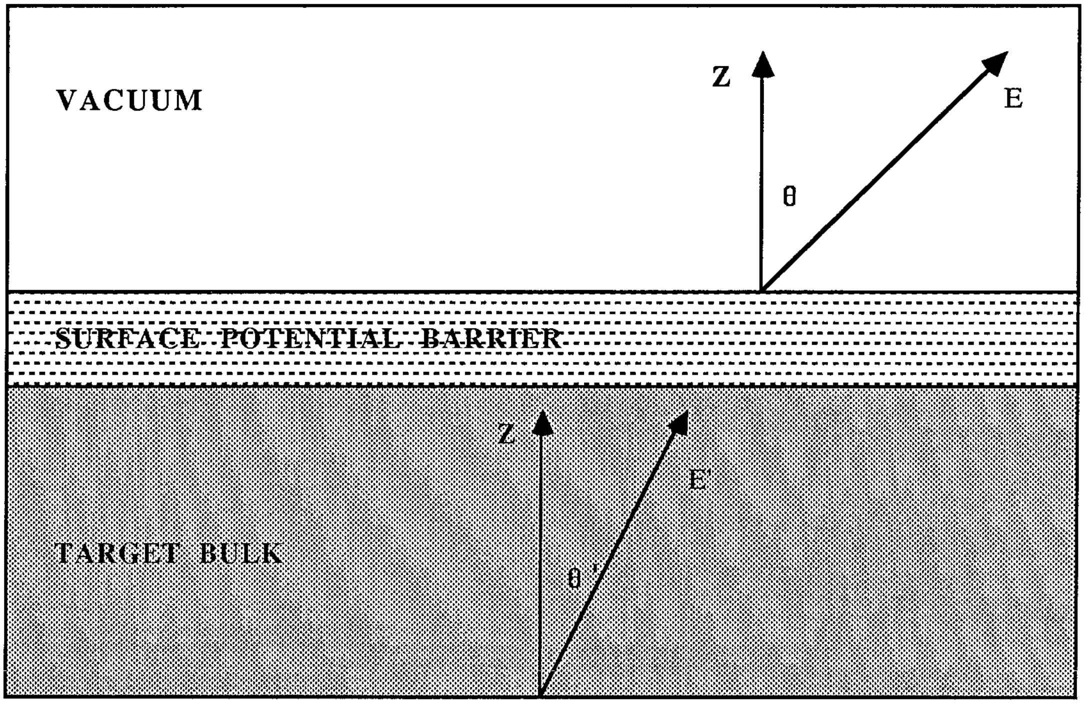

Figure 1: Geometry showing the refraction of a flux of target atoms with energy **E'** moving in a direction **θ '** with respect to the surface normal **z**. The surface potential barrier alters the energy and direction of the atoms as they emerge from the barrier with new energy and direction **E** and **θ** respectively.

Conservation of energy and transverse momentum give:

$$E = E' - E_b \tag{1.14a}$$

$$\sqrt{E}\,\sin\theta = \sqrt{E'}\,\sin\theta'. \tag{1.14b}$$

These equations define the Jacobian of the transformation to the new coordinates **E** and **θ**. From flux conservation we find the flux outside the surface potential barrier as:

$$(1.15)\qquad \mathbf{J_n(E,\theta)\,dE\,d\Omega = J'_n(E',\theta')\,dE'\,d\Omega'.}$$

We obtain the Jacobian elements from (1.14):

$$(1.16a)\qquad \mathbf{\frac{dE'}{dE} = 1}$$

$$(1.16b)\qquad \mathbf{\frac{d\Omega'}{d\Omega} = \frac{\sin\theta'}{\sin\theta}\frac{d\theta'}{d\theta} = \frac{E}{E'}\frac{\cos\theta}{\cos\theta'}}\ .$$

The final expression for the flux of sputtered atoms across the surface is then:

$$(1.17)\qquad \mathbf{J_n(E,\theta)\,dE\,d\Omega}$$

$$= \mathbf{D_m\,J_0\left(\frac{1}{n}\frac{dE_0}{dx}\right)\frac{E}{(E+E_b)^{3-2m}}\,dE\,\cos\theta\,\frac{d\Omega}{4\pi}}\ .$$

Note that we have not assumed a direction of incidence for the ion beam, and the number of sputtered atoms crossing the surface per unit area per unit time is independent of this direction. To obtain the sputtering yield, consider a beam of incident ions of cross section $A_0$

and an angle of incidence $\theta_0$ measured with respect to the surface normal. The beam will intersect a surface area of $A = \frac{A_0}{\cos\theta_0}$. The current of sputtered atoms is $AJ_n(E,\theta)dEd\Omega$, while the current of incident ions is $A_0J_0$. The sputtering yield is given by the ratio of these currents:

(1.18)

$$\frac{dS^2}{dEd\Omega}(E,\theta) = \frac{D_m}{4\pi} \sec\theta_0 \left(\frac{1}{n}\frac{dE_0}{dx}\right)\frac{E}{(E + E_b)^{3-2m}} \cos\theta \ .$$

This is the differential sputtering yield giving the number of atoms sputtered per ion per unit energy per unit solid angle.

Several features of this model should be noted:

1. The incident ion characteristics affect only the overall yield.
2. The yield increases with increasing angle of ion incidence.
3. The yield has the same functional dependence on the incident ion energy as the ion stopping power.
4. The inverse dependence on target density is deceptive since the ion stopping power is proportional to the target density.

5. The angular spectra of sputtered atoms have a universal $\cos\theta$ dependence, which is independent of the ion and target.

6. The energy spectrum of sputtered atoms has a universal form $\frac{E}{(E + E_b)^{3-2m}}$.

7. The energy and angular spectra of sputtered atoms are decoupled from each other; the energy spectrum is independent of the angle of ejection, and the angular spectrum is independent of the energy.

Let us look at some of the physical reasons behind these features and see how they compare with experiments. (1) and (2) stem from the assumption that majority of the sputtered atoms are high generation recoils and have no memory of the ion that initiated the cascade. Experimentally, dependence on incident ion characteristics of the sputtered atom spectra has been reported. Increase of sputtering yield with increasing angle of ion incidence has been observed to follow approximately the $\sec\theta_0$ dependence [25]. However, an oblique angle of incidence has, in addition, been observed to cause asymmetries in the angular spectra of sputtered atoms [26]. A simple argument for (2) is that a beam of ions at oblique incidence will intersect a larger area (larger by a factor of $\sec\theta_0$) of the surface than at normal incidence. Or equivalently, each atom will traverse a longer path (longer by a factor of $\sec\theta_0$) within a given surface layer in the oblique case. Experiments deviate from this at glancing angles of incidence, presumably because of the scattering of ions at the surface. (3) reflects the linear assumption that collisions do not take place between two particles that are simultaneously moving. Experimentally, non-linear dependence of the yield on ion stopping power (thermal spike effect) is observed in molecular-ion and heavy-ion bombardments. (5) stems directly from the assumed isotropy of the moving atom flux within the target. Experimentally, a $\cos^n\theta$ dependence is observed with $n$ between 1 and 4. The energy spectrum (6) is especially sensitive to the surface binding energy $E_b$ at low energies, and a major assumption is that of a planar surface potential barrier. Experimentally, (6) is qualitatively correct with $E_b$ chosen around the sublimation energy of the target material and $m$ close to 0, suggesting hard sphere collisions. However, the exact choice for $E_b$ to fit experimental data is often a black art [27]. Finally, it should be mentioned that until recently most experimental conditions restrict observations to either the energy integrated angular spectrum or the energy spectra at a particular ejection angle. Recent experimental measurements of energy and angular resolved spectra by Winograd [28] show deviations from (7).

## 1.4 Experimental Aspects

Experimental studies of sputtering generally have three basic requirements:

1. A stable and well-focused ion beam with well-defined charge state, mass, and energy.
2. Ability to measure precisely the ion fluence (dose).
3. Ability to resolve and measure the sputtered particles.

Until the 1960's when ion accelerators came into wide use in these studies, most experiments were done in plasma discharges. In these measurements the plasma is definitely not a well defined beam while fluence measurements are complicated by secondary electron emissions, which were impossible to suppress in a discharge tube. These experiments are more suited for gaining empirical information for practical applications and are not suited for studying basic sputtering mechanisms.

Modern sputtering experiments generally use ion accelerators to produce well-defined beams. The ion accelerator consists of the basic components of an ion source, an ion extraction stage, an ion accelerating stage, an analyzing magnet, and series of intermediate focusing and steering magnets and einzel lenses. Ions are extracted from an ion source (usually a plasma discharge) by an extraction voltage and simultaneously focused into the accelerating stage by einzel lenses. They are then accelerated through a high voltage and passed through an analyzing magnet that passes only ions of desired mass, charge, and energy. After passing through the analyzing magnet, the beam is focused and steered through a series of magnetic quadropoles and finally passes through a collimator and is focused on the target.

The ion fluence is measured by integrating the beam current. Most current integration is done with a Faraday cup. If measurements are to be made during bombardment, the target becomes a part of the Faraday cup. Real-time current integration is more reliable but is often complicated by the emission of secondary electrons and ions from the target and surrounding material. In the case of insulating targets, additional complications result from the charging of the surface during bombardment. Despite the difficulties, many reliable techniques exist for current integration.

The measurement of the sputtered material poses the greatest challenge. The two basic approaches are either to measure directly the material that comes off or to measure the amount of material left after bombardment. Most of the earlier experiments were concerned with overall yields and used the more primitive method of measuring what was left on the target. Techniques for measuring target weight loss include post bombardment micro-balance measurements and *in situ* quartz-oscillator methods. These methods cannot give any information on the spectra of sputtered particles and are now mostly obsolete. Since most of the sputtered material comes off as neutrals, direct *in situ* techniques such as SIMS are not applicable. For this reason direct measurements often involve collecting the sputtered material for post bombardment analysis. Various methods exist for collecting and analyzing the sputtered material. A common and more reliable method is to collect the sputtered atoms on a foil and perform post sputtering analyses, e.g., by *Rutherford Backscattering Spectrometry* (RBS) [29] or *Secondary Ion Mass Spectrometry* (SIMS) [30].

Angular and energy spectra measurements are done mostly by the collector foil technique [31]. The angular spectrum is deduced from the surface density of sputtered atoms on the collector foil by unfolding the sputtering geometry. The energy spectrum may be obtained from time-of-flight techniques such as employing a fly wheel simultaneously as a collector and beam chopper [32]. The wheel is placed between the beam and target. An opening on the wheel in effect pulses the beam as the wheel spins. The sputtered atoms are collected and their energy is deduced from its position on the flywheel relative to the opening. These methods, although ingenious, do not easily allow the determination of energy and angle resolved spectra (i.e., the differential sputtering yield). Until recently all experiments measured incomplete domains of the differential sputtering yield. Either the energy spectrum was observed at one direction of ejection, or the angular spectrum was observed for all energies together. Development of the laser-induced ionization technique by Winograd [33] and others now make measurements of the full differential sputtering yield possible. The target is sputtered by a pulsed ion beam. A pulsed laser of variable frequency is used to ionize selectively ejected particles of definite species. This laser is pulsed at a known delay with respect to the ion beam. The ionized particles are then drifted through an electric field towards a phosphor screen detector most conveniently situated parallel to the target surface. The time for the particles to pass through this electric field determines the mass. The two-dimensional image from the phosphor screen and the time information are ultimately fed into a computer. The delay between the laser pulse and the beam together with the spatial information allow for energy resolution by time of flight. Angle resolution is accomplished by unfolding the two-dimensional projection on the detector. The timing electronics and the detector-computer interface are fairly sophisticated.

## 1.5 Computer Modeling

Computer simulations of physical systems generally take on two approaches - stochastic or deterministic. The stochastic method takes advantage of an underlying probability distribution often derived from first principles, and it generates randomly an ensemble of system states conforming to this distribution. A deterministic approach, on the other hand, numerically integrates the system's equations of motion and generates a temporal evolution of the system states. Hybrids of these two methods are also possible. The advantage of the deterministic approach is a well-defined, temporal description of how the system evolves. The stochastic approach propagates the system via a Markov chain and neglects the detailed mechanisms of system evolution. For this reason, times for processes are often ill defined in this approach. However, the stochastic approach has a computational advantage since it is much faster to select the next state randomly than to increment the equations of motion in time. Stochastic methods are then able to handle much larger systems than deterministic approaches. The stochastic approach is also desired when the underlying equations of state are unknown or irrelevant. Two well-known examples of the stochastic and deterministic approaches are the Monte Carlo (MC) [34] and molecular dynamics (MD) [15] techniques, respectively. This thesis will take the latter approach under the conviction that sputtering is a highly non-equilibrium phenomenon where the details of the collision mechanisms are essential; thus, the MD technique is necessary.

Computer simulations of sputtering may be divided into two major groups based on technique - binary collision (BC) and MD. The

BC technique, as the name implies, considers the collision of only two particles at a time. BC methods often incorporate MC techniques by randomly selecting impact parameters and using differential cross sections for calculating the binary collision outcomes. Therefore, in the sputtering literature, BC models are often referred to as MC models. The first use of computer simulation in sputtering was a BC model, Harrison [17]. Over the years as computers got faster, MD methods became more feasible. The MD method includes the full multiple interaction of all particles and is clearly more precise. Although many of the BC approximations may prove later to be justified, it is prudent to begin studies with MD whenever it is computationally feasible. Following will be a brief description of the MD technique.

## References

1. N. Bohr, *The Penetration of Atomic Particles Through Matter*, Bianco Lunos Bogtrykkeri, Denmark (1948).

2. P. Sigmund, *Sputtering by Particle Bombardment I*, Springer-Verlag, Berlin, (1981), chapter 2.

3. P. D. Townsend, J. C. Kelley, and N. E. W. Hartley, *Ion Implantation, Sputtering, and Their Applications*, Academic Press, New York, (1976).

4. W. R. Grove, Phil. Mag. **5**, 203 (1853).

5. E. Goldstein, Verh. Dtsch. Phys. Ges. **4**, 228, 237 (1902).

6. J. Stark, G. Wendt, Ann. Phys. (Leipzig) **38**, 921, 941 (1912).

7. A. von Hippel, Ann. Phys. (Leipzig) **80**, 1043 (1926).
   C. H. Townes, Phys. Rev. **65**, 319 (1944).

8. P. Sigmund, Phys. Rev. **184**, 383 (1969).

9. M. W. Thompson, Phys. Rep. (Rev. Sec. of Phys. Let.) **69**, No. 4, 335 (1981).

10. J. Lindhard, M. Scharff, and H. E. Schiott, Mat. Fys. Medd. Dan. Vid. Selsk. **33**, No. 14 (1963).

11. J. A. Davies, J. Friesend, and J. D. McIntyre, Can. J. Chem. **38**, 1526 (1960).
    J. A. Davies, G. C. Ball, F. Brown, and B. Domeij, Can. J. Phys. **42**, 1070 (1964).

12. W. Brandt and R. Laubert, Nucl. Instr. and Meth. **47**, 201 (1967).

13. F. Keywell, Phys. Rev. **87**, 160 (1952); Phys. Rev. **97**, 1611 (1955).

14. G. K. Wehner, J. Appl. Phys. **26**, 1056 (1955); Phys. Rev. **102**, 690 (1956).

15. B. J. Alder and T. E. Wainwright, J. Chem. Phys. **27**, 2147 (1957).

16. J. B. Gibson, A. N. Goland, M. Milgram, and G. H. Vineyard, Phys. Rev. **120**, 1229 (1960).

17. D. T. Goldman, D. E. Harrison, Jr., and R. R. Coveyeau, ORNL **2729** (1959).

18. D. E. Harrison, Jr., Radiat. Eff. **70**, 1 (1983).

19. H. H. Andersen, Nucl. Instr. and Meth. **B18**, 321 (1987).

20. H. H. Andersen and H. L. Bay, J. Appl. Phys. **45**, 953 (1974); **46**, 2416 (1975).

21. R. Kelly, Radiat. Eff. **32**, 91 (1977).

22. P. Sigmund, Appl. Phys. Lett. **25**, 169 (1974); **27**, 52 (1975).

23. C. Claussen, Nucl. Instr. and Meth. **194**, 567 (1982).

24. Y.-T. Cheng, M-A. Nicolet, W. L. Johnson, Phys. Rev. Lett. **58**, 2083 (1987).

25. H. H. Andersen and H. L. Bay, *Sputtering by Particle Bombardment I*, Springer-Verlag, Berlin, (1981), chapter 4.

26. E. S. Mashkova and V. A. Molchanov, Radiat. Eff. **102**, 125 (1987).

27. B. J. Garrison, N. Winograd, D. Y. Lo, T. A. Tombrello, M. H. Shapiro, and D. E. Harrison, Jr., Surf. Sci. **180**, L129 (1987).

28. J. P. Baxter, J. Singh, G. A. Schick, P. H. Kobrin, and N. Winograd, Nucl. Instr. and Meth. **B17**, 300 (1986).

29. W. K. Chu, J. W. Mayer, and M. A. Nicolet, *Backscattering Spectrometry*, Academic Press, London (1978).

30. R. J. Colton, J. Vac. Sci. Tech., **18**, 737 (1981).

31. Y. Qiu, J. E. Griffith, and T. A. Tombrello, Nucl. Instr. and Meth. **B1**, 118 (1984).

32. M. W. Thompson, Nucl. Instr. and Meth. **B18**, 411 (1987).

33. J. P. Baxter, G. A. Schick, J. Singh, P. H. Kobrin, and N. Winograd, J. Vac. Sci. Tech. **4**, 1218 (1986).

34. N. Metropolis, A. W. Rosenbluth, M. N. Rosenbluth, A. H. Teller, E. Teller, J. Chem. Phys. **21**, 1087 (1953).

# Chapter 2 - Molecular Dynamics

## 2.1 Physical Model

Atomic collisions are, in the most general case, quantum many-body problems. The enormous number of degrees of freedom in this case is beyond any analytical or computational technique. However, we are not interested in the details of electron motion and will seek a classical approximation to the atomic motions. The extreme mass mismatch between the electrons and nuclei allows decoupling of the nucleus coordinates from the electron coordinates (*Born-Oppenheimer approximation*) [1]. As atoms collide, electrons will be excited and in some cases lost or captured. The instantaneous electron distributions will through screening and binding determine *instantaneous* interactions between the atomic centers. This instantaneous interaction will fluctuate and is approximated by an *averaged* atomic interaction that is constant in time. The concept of an averaged interaction is more justified in metals where the electron relaxation time is short, causing the instantaneous interaction to fluctuate with a frequency large compare to the collisional frequency. Conversely, the electron relaxation time in insulators is long enough to affect atomic trajectories, making an interaction constant in time less valid. Energy is transferred elastically (nuclear stopping) through the interaction between the atomic centers and inelastically through electron excitation (electronic stopping) [2]. For our metallic systems in the nuclear stopping regime, it is therefore reasonable to consider atoms as structureless points. Any effects that are due to internal structure will be implied in the many-body nature of the atomic interactions.

The assumption that atomic trajectories are governed by classical mechanics during sputtering is not a trivial one and has been addressed by Bohr [2]. Simple analysis of atomic scattering by a Coulomb potential shows that quantum diffraction caused by spatial localization of its impact parameter is negligible compared with the scattering angle, provided that the atom's reduced wavelength ($\lambda / 2\pi$) is much shorter than the collision diameter. Here the collision diameter is the distance of closest approach to the scattering center in a head-on collision. In the case of a screened Coulomb potential, the reduced wavelength must also be much shorter than the screening radius **a** over which the potential varies significantly. As opposed to pure Coulomb scattering, there will also be a critical angle of deflection $\theta_c = \lambda / 2\pi \mathbf{a}$, below which classical mechanics is invalid. An 1 eV Cu atom has a reduced wavelength of .006 Å, while a typical Cu screening radius is ~.100 Å. The critical deflection angle here is .55 degrees. In a collision cascade initiated by keV ions, the majority of atoms satisfy the conditions for which the classical trajectory is a good approximation. There will always be a fraction of thermal energy atoms and atoms that undergo small angle scattering for which the classical treatment becomes questionable. It should also be stressed that Bohr's analysis is purely for two-body collisions. Thus, the validity of the classical point-atom picture is best justified by comparison with experimental results.

The state of a classical system of **n** particles may be represented numerically in a computer by **2fn** numbers, where **f** is the degrees of freedom for each particle. In our case **f = 3** and we have three position and three momentum variables for each atom. The starting point for any simulation is to model the forces that govern the particle motions as realistically as possible. The interaction between particles is conveniently stated by a total potential energy function **U**. For a closed system of **n** particles free from any external fields, **U** is a function of the spatial coordinates only:

$$U = U(X_1, \ldots, X_{3n}). \tag{2.1}$$

Here, $X_i$ is the position coordinate. The force components on any particular particle are then given by:

$$F_i = -\frac{\partial U}{\partial X_i}. \tag{2.2}$$

The MD method evolves the state of the system by propagating it with a set of equations of motion. The atomic motion in our case will be described by Newtonian mechanics. The equations of motion are:

$$(2.3a) \qquad \frac{dX_i}{dt} = V_i$$

$$(2.3b) \qquad \frac{dV_i}{dt} = \frac{F_i}{m_i} \equiv A_i(X_1, \ldots, X_{3n}).$$

Here we have chosen to write it in terms of the velocity variables $V_i$ rather than momentum. This is a system of **6n** coupled, first-order differential equations and is integrated numerically. Many techniques for numerical integration have been developed and most fall into the general category of *predictor-corrector* algorithms [3]. The choice of algorithms is made based on the particular problem at hand.

## 2.2 Interatomic Potentials

The atomic interaction (2.1) is in general many-body and may have a directional dependence. Directional dependences are important for highly non-spherical atoms. For a system of atoms free from external fields, two-body interactions are non-directional by spatial symmetry, and any directional dependence must be in the n-body terms, where n > 2. A classic example is the Si tetrahedral bond, where the directionality of the interaction is reflected in the crystal structure. Three-body forces are required to describe the Si interatomic potential [4]. In most metals (those that form a close-packed crystal structure), atoms are more or less spherical, and spherically symmetric interatomic potentials are adequate. We will not consider non-spherically symmetric potentials in this thesis. Many-body forces arise from induced disturbances of the electron cloud in the presence of neighboring atoms. Thus, such forces are especially important for atoms with unfilled electron shells and for all atoms at distances where the shells overlap. As the atomic separations become smaller the many-body forces become more important until we reach the extremely small separations (comparable to the screening radius), where the two-body nucleus-nucleus interaction will dominate. In metals, where the conduction electrons are easily disturbed by any motion of the nuclei, many-body forces are expected to be important even for low-energy (few tens of eV) atomic displacements . This is reflected by the fact that purely two-body forces can not correctly account for the experimentally observed Cauchy inequality among the elastic constants in metals [5]. However, until recently no satisfactory methods existed for taking into account many-body forces in the collisional dynamics of metal atoms. For this reason, the atomic interactions are approximated by two-body forces in most parts of adjusted to fit the lattice constant and the sublimation energy of the substance in question. A more general form of the Lennard-Jones potential treats the exponents as free parameters and requires additional experimental data such as viscosity to determine the potential uniquely. Torrens provides an excellent comprehensive review of interatomic potentials [6].

The simple Lennard-Jones potential, while useful for describing the interactions between relatively inert atoms at distances close to the equilibrium separation (nearest neighbor distance in a crystal at equilibrium), is not sufficient for metals and close atomic encounters that are expected in a collisional phenomenon such as sputtering. Instead, we will use a Moliere pair potential for the short-range (shorter than the equilibrium separation) and a Morse potential for the long range (close to and beyond equilibrium separations). The Moliere and Morse potentials are both based on quantum mechanical considerations [6]. However, the former is valid only at short range and the latter valid only at long range. The short-range potential is smoothly joined to the long-range part by a cubic spline.

## 2.3 Integration Logic

Once a suitable interaction potential has been determined, thus defining the equations of motion, a method must be chosen to integrate this set of differential equations. The general approach is best illustrated by considering a one-dimensional, first-order equation:

$$(2.4) \qquad \frac{dy}{dx} \equiv y' = f(x,y)$$

The numerical approach is to transform this differential equation into a difference equation. Consider a small finite increment **h** of the independent variable **x**:

$$(2.5) \quad y(x+h) - y(x) = \int_{x}^{x+h} f(t,y(t))\,dt \equiv D(x,h).$$

Next, we grid x-space and consider a discrete set of x-values $\{x_i\}$. A numerical solution of (2.4) is a discrete sequence $y_i$ that approximates $y(x_i)$. Consider the discrete form of (2.5):

$$(2.6) \qquad y_{i+1} - y_i = D(x_i,h_i) \equiv D_i \; ; \quad h_i \equiv x_{i+1} - x_i \,.$$

The various methods for solving (2.4) such as the Euler, Runge-Kutta, and predictor-corrector differ in the way that $D_i$ is approximated. Once a scheme for approximating $D_i$ is invented, the solution set $\{y_i\}$ follows from applying (2.6), recursively, starting with an initial condition $y(x) = y_0$. As an example consider the first-order predictor-corrector method. Starting at the point $(x_i,y_i)$, a first approximation for $y_{i+1}$ (the predictor) is:

$$(2.7)\quad y_{i+1} \approx y_i + y'(x_i)h_i = y_i + f(x_i,y_i)h_i \equiv y_p .$$

This is equivalent to treating the integrand in $D_i$ as constant. With the predictor $y_p$ we can estimate $y'(x_{i+1}) \approx f(x_{i+1},y_p)$ and obtain a better approximation for $y_{i+1}$ (the corrector) as:

$$(2.8)\qquad y_{i+1} \approx y_i + \frac{h_i}{2}\left( f(x_i,y_i) + f(x_{i+1},y_p) \right).$$

The corrector is now compared with the predictor for an error check. If the difference is outside an acceptable error, the corrector is used as a predictor in (2.8) to generate a new corrector and, the steps may be repeated until one is content with the error. After passing the error test, the corrector is set to $y_{i+1}$, thereby completing the recursion loop. There are many different methods of changing the predictor-corrector pair and they are classified by the order of $h_i$ that appears in the predictor-corrector expressions.

A predictor-corrector scheme is used to solve (2.3) in the present MD code. The predictor-corrector method has the advantage that local errors created during each integration step are easily kept in check. The predictors for the positions and velocities are:

**(2.9a)**

$$V_i(t+\delta t) \approx V_i(t) + \delta t\, A_i(X_1(t), \ldots, X_{3n}(t)) \equiv V_{pi}$$

**(2.9b)**

$$X_i(t+\delta t) \approx X_i(t) + \frac{\delta t}{2} ( V_{pi} + V_i(t) ) \equiv X_{pi} .$$

It is convenient to define:

**(2.10a)** $A_i(t) \equiv A_i(X_1(t), \ldots, X_{3n}(t))$, and

**(2.10b)** $A_i(t+\delta t) \equiv A_i(X_{p1}, \ldots, X_{p3n})$.

The correctors are then:

**(2.11a)**

$$V_i(t+\delta t) \approx V_i(t) + \frac{\delta t}{2} (A_i(t+\delta t) + A_i(t)) \equiv V_{ci} \text{ , and}$$

**(2.11b)**

$$X_i(t+\delta t) \approx X_i(t) + \frac{\delta t}{2} (V_{ci} + V_i(t)) \equiv X_{ci} .$$

Next, we perform the error test by checking the difference between the corrector and predictor against an allowed threshold. Note that $X_{c_i}-X_{p_i}$ is proportional to $V_{c_i}-V_{p_i}$; hence, it is sufficient to check only the velocity error after each integration step and require its absolute value to be within a preset value. The time step $\delta t$ is allowed to vary throughout the integration. $\delta t$ is increased steadily with each successful pass of the velocity-error test. If the test should fail, $\delta t$ is drastically decreased and the time step re-performed. At the end of a successful time step, the positions and velocities are set to their corrector values, and a new integration step begins. The integration parameters of this scheme consist of the velocity error threshold and the rate of increase and decrease of the time step. These parameters are chosen to optimize total energy conservation. Typically, the total energy fluctuation is kept at a few percent of the total kinetic energy.

## 2.4 Geometry and Boundary Condition

Substrate geometry and boundary condition must be cautiously defined with the underlying physical process in mind. Improper choice may result in artificial effects that are peculiar to the particular geometry or boundary condition. On time scales of the system relaxation time, the choice of initial substrate geometry may affect the ultimate relaxed and/or reconstructed substrate structure

[7]. This is less of a problem in the case of sputtering, where the time scale is much shorter than the crystal relaxation times. However, boundary conditions will be important on all time scales. For sputtering, a periodic boundary condition results in flows of energy from neighboring periodic cells, which will cause an artificial spike within the target. Periodicity also results in hyper-surface collisions between sputtered atoms originating from neighboring cells, a condition that is unrealistic. Because sputtering times are much shorter than target relaxation times, the target may be treated with free boundary conditions during the sputtering simulation as long as boundary effects are eliminated from the quantity of interest by taking a sufficiently large system.

Harrison has shown that relative sputtering yields are fairly insensitive to target size for targets consisting of more than 400 atoms (14x14 atomic layers in the plane of the target surface) in the case of low keV ion bombardment [8]. This size may be inadequate when one is interested in effects extremely sensitive to the absolute yields such as *isotopic fractionation* (Chapter 7). Simulations in this thesis have been performed with targets of 400 to 700 atoms.

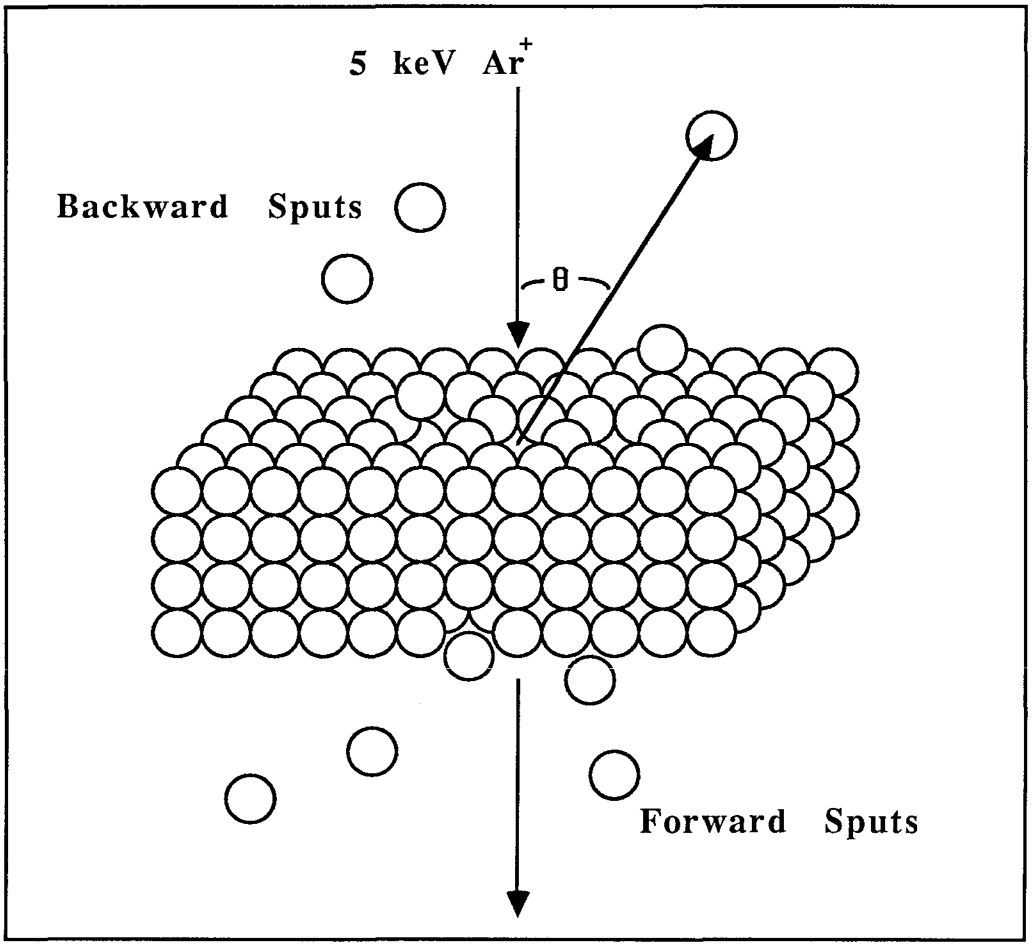

Figure 2: Target geometry showing the target orientation relative to incident ion beam direction and ejection angle θ of sputtered atoms.

Target geometry used throughout simulations in this thesis is illustrated in Figure 2. The actual target dimensions used range from 14x14 to 16x16 atomic layers in the lateral dimensions and 4 to 6 atomic layers in the direction perpendicular to the surface. In all cases the ion approaches the target at normal incidence.

## References

1. M. Born and J. R. Oppenheimer, Ann. Phys. **84**, 457 (1927).

2. N. Bohr, *The Penetration of Atomic Particles Through Matter*, Bianco Lunos Bogtrykkeri, Denmark (1948).

3. F. Scheid, *Theory and Problems of Numerical Analysis*, McGraw-Hill, New York (1968).

4. F. Stillinger and T. Weber, Phys. Rev. **B 31**, 5262 (1985).

5. M. S. Daw and M. I. Baskes, Phys. Rev. **B 29**, 6443 (1984).

6. I. M. Torrens, *Interatomic Potentials*, Academic Press, New York (1972).

7. M. Moody, J. R. Ray, and A. Rahman, Phys. Rev. **B35**, 557 (1987).

8. D. E. Harrison, Jr., Radiat. Eff. **70**, 1 (1983).

# Chapter 3 - Sputtering from Liquid Cu

## 3.1 Introduction

Both experimental and computer simulation studies of sputtering have concentrated on solid targets. There are fundamental differences between the solid and liquid phase that may affect the sputtered atom spectra. The bulk structure of a liquid possesses spherical symmetry as opposed to the highly directional structure of single crystals. In polycrystalline materials the directional effects will be lost in the averaging of atoms ejecting from single grains oriented in random directions. However, since the grains in a polycrystalline material are large compared to the range of the interatomic force, a polycrystalline surface will appear very different from a liquid surface to an ejecting atom. Furthermore, the surface structure between the two phases is also fundamentally different during ion bombardment. In the liquid case, atoms diffuse from the bulk to the surface during ion bombardment so as to keep the surface composition (in the case of multicomponent materials) and surface topography constant. For solids, aside from the relatively small effects of radiation enhanced diffusion, surface composition and topography change drastically with ion fluence. Experimentally, this effect is observed in the sputtering of multicomponent targets [1]. In solids, preferential sputtering of one component is observed at low ion fluences, while the composition of the sputtered material approaches stoichiometric values as the ion fluence is increased. For liquids, preferential sputtering persists with increasing ion fluence, while the preferentially sputtered component near the surface is replenished by diffusion from the bulk. These fundamental differences make sputtering from targets in the liquid phase an interesting topic.

The objectives of this MD study of sputtering from liquid Cu are the following:

1. Develop methods to simulate sputtering from liquids in general.
2. Investigate the energy and angular spectra of sputtered atoms from liquid targets and compare them to results from crystal targets.
3. Determine the depth of origin of the sputtered atoms.

## 3.2 Summary

The generation of liquid targets for subsequent sputtering simulations is accomplished by melting a slab initially in the crystalline phase. The melting process is simulated by additions of heat through uniform scaling of each atom's velocity while evolving the system under a spatial boundary condition. Two alternate boundary conditions, semiperiodic and box boundaries were investigated. The box-boundary condition simply reflects the atoms elastically as they approach the boundary walls. The semiperiodic boundary condition translates the entire slab periodically in the plane normal to the target surfaces, while the two surfaces are evolved free of any boundary conditions (i.e. free surfaces). The box boundary condition was found to give anomalous atomic densities near the boundary walls and was thus deemed inadequate as a realistic description of liquid surfaces (Fig. 5 of App. 3.1). Satisfactory results were found using the semiperiodic boundary conditions for liquid target generations.

The melting process may be monitored by the time evolution of the pair correlation function as shown in Figure 3. At 100 femtoseconds the fcc structure is clearly visible. After 1 picosecond the pair correlation function closely resembles that of a liquid, although long range structure may still be seen in crossectional views of the atomic positions. Long-range order vanishes completely after a few picoseconds. The final liquid Cu pair correlation function from simulation agrees well with the experimental function obtained from neutron scattering (Fig. 4 of App. 3.1).

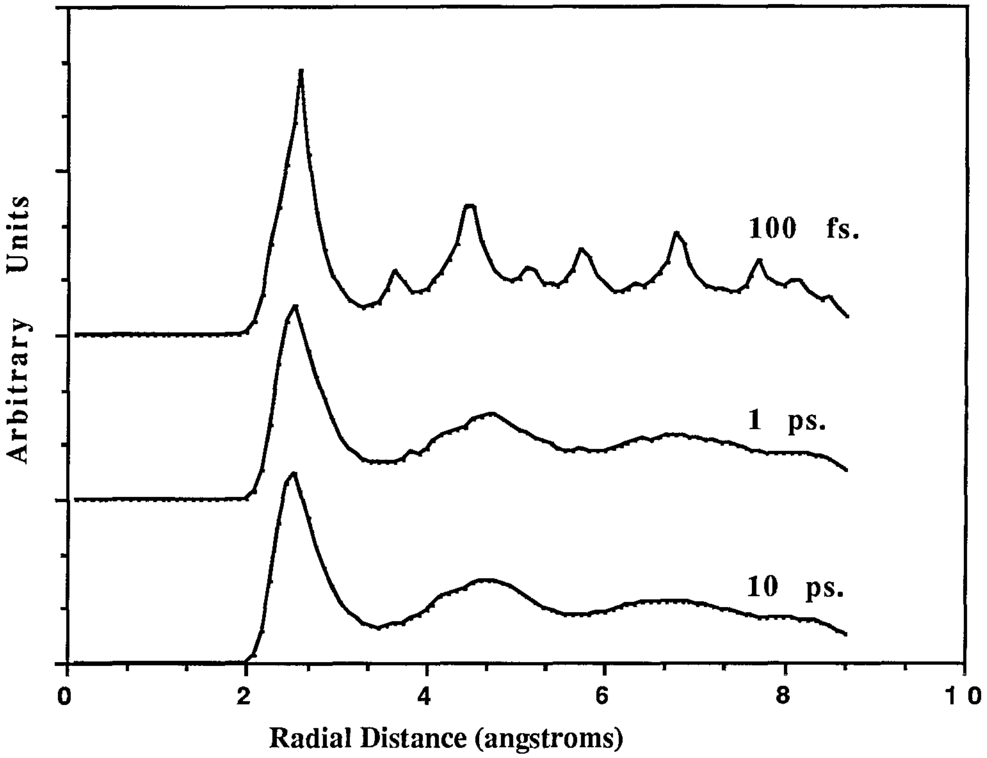

Figure 3: Pair correlation functions at 100 femtoseconds, 1 picosecond, and 10 picoseconds from the time when heat was initially added to the perfect crystal.

The angular distributions obtained from simulations of sputtering from liquid targets, as expected, lack the Wehner spots observed for sputtering from single crystals and are similar in shape to those observed experimentally for sputtering from polycrystalline and liquid targets (Fig. 2 of App. 3.2). The simulated angular distributions from liquid targets follow a cosine power ($\cos^n\theta$). The exponent **n** is 2 for the free-surface targets, while **n** is 3 for targets generated under the box boundary condition (Tab. 5 of App. 3.1). Two mechanisms may be responsible for the broader angular distribution in the free surface case. The free surface is much rougher on an atomic scale than the surface generated by the box boundary, which constrains the surface atoms to a plane. A rough surface can randomize or broaden the angular distribution as ejecting atoms collide with dangling atoms protruding from the surface plane. Furthermore the artificially high surface particle density created by the box-boundary condition will make grazing ejections more difficult.

The angular distributions are generally broader for higher target temperatures (Tab. 5 of App. 3.2). Higher temperature targets have slightly less uniform surfaces because of the kinetic motions of the surface atoms. This fact supports the conclusion that dangling atoms protruding from the surface are responsible for the angular distribution broadening.

A definite trend for atoms ejecting from below the first surface layer to have a much sharper angular distribution (larger **n**) is seen in these simulations (Tab. 5 of App. 3.2). Atoms from below the surface will collide with more atoms during grazing angle ejections and in a sense will be "channeled" into the normal direction, resulting in a sharper angular distribution. This phenomenon has been observed experimentally in the sputtering of binary targets [1,2].

A qualitative comparison of the simulated energy distributions of sputtered atoms from liquid and single crystal [3] targets shows no significant difference in the overall angle-integrated energy distributions (Tab. 4 of App. 3.2). Although differences in angular-resolved energy distributions that are due to the Wehner spot effect are expected. Within the Wehner spots the energies of sputtered atoms are significantly higher [4].

These simulations show that over 80% of the sputtered atoms originate in the first surface layer (Tab. 3 of App. 3.2). The relative sputtering yields from the first and second surface layers are in excellent agreement with the simulated results from single crystals averaged over the three low index orientations [3]. They are also in agreement with sputtering experiments with binary targets [1,2].

The approach described in this chapter for simulating sputtering from targets in the liquid phase has yielded results that are in reasonable agreement with experiments. The importance for simulating liquid phase sputtering is clear, and we have demonstrated the usefulness of molecular dynamics simulations in this regard.

## References

1. M. F. Dumke, T. A. Tombrello, R. A. Weller, R. M. Housley, and E. H. Cirlin, Surf. Sci. **124**, 407 (1983).

2. K. M. Hubbard, R. A. Weller, D. L. Weathers, and T. A. Tombrello, Nucl. Instr. and Meth., to appear in the Proceedings of the Accelerator Conference (1989).

3. M. H. Shapiro, P. K. Haff, T. A. Tombrello, and D. E. Harrison, Jr., Nucl. Instr. and Meth. **B12**, 137 (1985).

4. N. Winograd, P. H. Kobrin, G. A. Schick, J. Singh, J. P. Baxter, and B. J. Garrison, Surf. Sci. **176**, L817 (1986).

Nuclear Instruments and Methods in Physics Research B17 (1986) 207-212
North-Holland, Amsterdam

# LIQUID TARGET GENERATION TECHNIQUES IN MOLECULAR DYNAMICS STUDIES OF SPUTTERING *

D.Y. LO and T.A. TOMBRELLO

*Division of Physics, Mathematics and Astronomy, California Institute of Technology, Pasadena, CA 91125, USA*

M.H. SHAPIRO

*Department of Physics, California State University, Fullerton, CA 92634, USA and*
*Division of Physics, Mathematics and Astronomy, California Institute of Technology, Pasadena, CA 91125, USA*

Received 15 November 1985 and in revised form 20 March 1986

Techniques of generating liquid targets for molecular dynamics studies of sputtering were investigated in systems consisting of 603 Cu atoms. The effects of different boundary conditions on sputtering yield, layer yield ratio, energy distribution, and polar angular distribution of ejected particles were found to be important. A box boundary condition and a semiperiodic boundary condition were considered. The box boundary conditions required the particles to experience pure reflection at the boundaries, while semiperodic boundary conditions demanded position and momentum periodicity in the two dimensions defined by the surface of the target. Sputtering from the target generated with a box boundary condition resulted in a 60% higher total yield, a slightly higher first layer yield ratio, a 60% lower surface binding energy, and a sharper polar angular distribution than from the target generated under a semiperodic boundary condition at the same temperature. Since the results obtained with the semiperiodic boundary conditions are in better agreement with experimental sputtering results, we have concluded that the semiperiodic boundary conditions produces a target that better represents the free surface of real liquid systems.

## 1. Introduction

In recent years there has been a growing interest in the sputtering of liquid alloys. The high diffusion rate of the liquid state is able to keep target surface composition constant during bombardment. Thus, dose dependent surface compositional changes can be ignored when comparing experimental results to theoretical predictions. In the case of a Gibbsian segregated surface the segregated component is replenished from the bulk by diffusion, thereby keeping a surface of constant composition during bombardment.

When the surface composition is known (e.g. via AES or ISS), it is possible to determine the fraction of sputtered particles that originate from the segregated layer. Dumke et al. experimentally showed that 85% of the ejected atoms came from the first monolayer in the sputtering of a liquid Ga-In eutectic alloy by 15 keV incident $Ar^+$ ions [1]. In a recent paper, we performed a computer simulation of sputtering from liquid Cu targets by 5 keV incident $Ar^+$ ions [2]. Our results were in general agreement with those of Dumke.

A reasonable liquid target must first be generated in order to simulate the sputtering. (A molecular dynamics computer model of a target of $N$ particles requires a set of $6N$ numbers that specifies the positions and velocities of each of the particles.) In this paper we describe in detail the target generation techniques we attempted in the course of our simulation study and their effect on the sputtering results.

Two targets of 603 Cu atoms each were generated (referred to as targets A and B). Target A was generated by imposing a semiperiodic boundary condition while target B was evolved under a box boundary condition.

## 2. Simulation code

The multiple interaction molecular dynamics code SPUT1 was used to simulate sputtering events. A modification of SPUT1 was used to generate the liquid targets. SPUT1 also has been used in previous simulations of sputtering from solid crystalline and liquid Cu targets [2-4].

All particles are assumed to move under pairwise forces using Newtonian mechanics. The classical equations of motion are integrated with a first order predic-

---

* Supported in part by the National Science Foundation [DMR83-06541 and DMR84-21119 (Caltech) and DMR83-06548 (CSUF)], the Alexander von Humbolt Foundation, and Schlumberger-Doll Research.

tor-corrector. The large errors associated with such a low order predictor-corrector are reduced by a variable integration time step. The time step is adjusted during integration to optimize simultaneously computational speed and integration accuracy. For a more detailed description of SPUT1 see ref. [5].

## 3. Pair potentials

There are in general three ways to obtain the pair potential function which describes the interaction between atoms in the target. These are theoretical derivation from pseudo-potential theories [6], a semi-empirical approach [7], and experimental measurements based on the two-body interaction assumption [8]. Because the present theoretical understanding of metallic systems is still incomplete, we did not use the first approach. We initially attempted to invert the Cu structure factor obtained form neutron scattering [9]. The position of the minimum for the potential function obtained by this method turned out to be too large. This method was not expected to be reliable since the inversion process is itself an approximation. The resulting potential is very sensitive to unavoidable errors at the high wave number end of the experimental structure factor which ultimately affect the potential core. Furthermore this method is not applicable to the ion-atom potential. Therefore, the semi-empirical approach was used for the work reported here. The potential functions obtained by the latter two approaches are shown in fig. 1. (The potential obtained from the structure factor data is shown only for purposes of comparison.)

The semi-empirical atom–atom potential function consisted of a Molière core joined by a cubic spline to a long range attractive Morse function. The atom–atom potential function was cut off at 12 Å during target generation and 5 Å during sputtering runs. The ion and atoms interact through a Molière potential which is cut off at 2.5 Å. The potential functions and parameters are given in table 1.

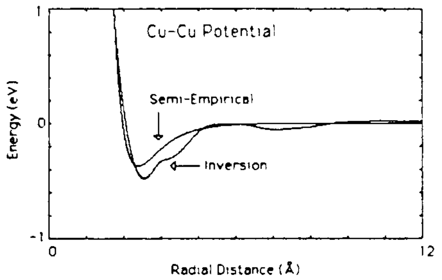

Fig. 1. Pair potential functions obtained from the semi-empirical approach and experimental structure factor inversion.

The Morse potential parameters were obtained from Girifalco and Weizer [10]. These were chosen to give the experimental lattice constant, bulk modulus, and heat of sublimation of crystalline Cu at 0 K. The well depth was slightly modified to give the correct heat of sublimation when the potential is cut off at 12 Å. To shorten computation time, a 5.25 Å cutoff was used during sputtering. Although this is not strictly consistent, the shorter cutoff will affect only the absolute sputtering yield (ref. [15]). No significant integration errors were introduced by the shorter cutoff, since overall energy conservation was maintained to better than a few tenths of a percent.

The Molière potential parameters were obtained from Torrens [7]. The Molière function is an approximate

Table 1
Potential parameters

| | |
|---|---|
| *Ion – atom* | |
| $V_{ij} = (A/r)[0.35e^{-0.3r/B} + 0.55e^{-1.2r/B} + 0.1e^{-6r/B}]$ | $r \leqslant r_a$ |
| $V_{ij} = 0$ | $r \geqslant r_a$ |
| $A = 6.01406$ keV · Å | |
| $B = 0.103481$ Å | |
| $r_a = 2.556$ Å | |
| *Atom – atom* | |
| $V_{ij} = (A/r)[0.35e^{-0.3r/B} + 0.55e^{-1.2r/B} + 0.1e^{-6r/B}]$ | $r \leqslant r_a$ |
| $V_{ij} = C_0 + C_1 r + C_2 r^2 + C_3 r^3$ | $r_a < r \leqslant r_b$ |
| $V_{ij} = D_e[e^{-2\beta(r-r_e)} - 2e^{-\beta(r-r_e)}]$ | $r_b < r \leqslant r_c$ |
| $V_{ij} = 0$ | $r > r_c$ |
| $A = 9.689326$ keV · Å  B = 0.096027 Å | |
| $C_0 = 597.3$ eV $\beta$  $C_1 = -814$ eV/Å  $C_2 = 371.7$ eV/Å$^2$  $C_3 = -57$ eV/Å$^3$ | |
| $D_e = 0.37$ eV = 1.359 Å$^{-1}$  $r_e = 2.866$ Å | |
| $r_a = 1.5$ Å  $r_b = 1.988$ Å  $r_c = 5.25$ Å (sputtering) | |
| $r_c = 12$ Å (target generation) | |

solution of the Thomas–Fermi equation. (c.f. ref. [7] for a more detailed description of the Morse and Molière potentials.)

### 4. Target generation

All targets considered have a rectangular configuration with dimensions of 34.0, 7.0, and 33.0 Å along the $x$, $y$, and $z$ axes respectively. During sputtering the incident ion velocity is in the $y$ direction, as shown in fig. 2.

Target A was generated by starting with 108 particles on a fcc close-packed lattice at liquid Cu density of 0.076 $Å^{-3}$. A Gaussian random number generator was used to assign a velocity to each particle. This resulted in a Maxwell–Boltzman distribution having a temperature of approximately 2500 K. The Maxwell–Boltzman distribution was imposed to shorten equilibration time, while the high starting temperature was needed to melt the target. The resulting crystal is a cube with six atomic layers along each of the $x$, $y$, and $z$ directions. Periodic boundary conditions are applied along the $x$ and $z$ directions leaving the two surfaces perpendicular to the $y$-axis free.

The 108 particles in the cube are bounded in the $y$ direction only by mutual periodic attraction. No additional surface binding was introduced. Once the crystal was melted and cooled to an equilibrium temperature of 1600 K (generally within the equivalent of a few picoseconds), nine identical cubes were combined to form a single target of 972 particles (see fig. 3).

Before target A was used for sputtering, two atomic layers parallel to and including one of the free surfaces were removed to reduce computation time. This left a target of 603 particles with the remaining free surface facing the incident ion. Several targets at various temperatures were prepared in this way for use in the liquid Cu sputtering simulation study (ref. [2]).

Target B was generated by applying box boundary conditions to target A. The box boundary condition was achieved by reversing the normal component of momentum (normal to the wall) of the particle when its center of mass hit a box wall. Thus, the particles were specularly reflected at the boundaries.

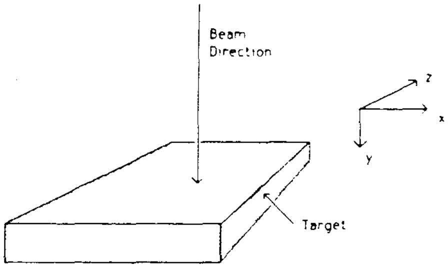

Fig. 2. Ion beam direction and target orientation.

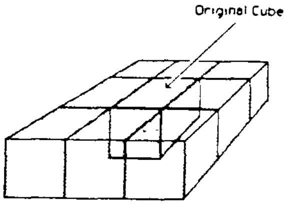

Fig. 3. Configuration for setting up semiperiodic boundary conditions.

When the box boundary conditions were first applied, the temperature rose from 1600 to 2000 K. To cool it to 1600 K, 0.60 eV/atom of energy was removed over approximately 2.5 ps (picoseconds) Target B was then allowed to further equilibrate for about 500 fs (femtoseconds).

All temperature adjustments were made by uniformly scaling the velocities of each particle during each integration step so that the kinetic energy is added or subtracted uniformly throughout the adjustment period. This is done to keep the system in a semi-equilibrium state during heating or cooling. By increasing the adjustment period, one can reduce the time required to reach equilibrium again.

### 5. Liquid properties

By assuming pairwise additivity of the potential energy of the system and neglecting electronic degrees of freedom, macroscopic properties such as diffusion, heat capacity, and surface tension are dependent only upon the pair potential function, particle mass, and boundary conditions. We have not attempted to reproduce the exact experimental data for these properties. Rather we are more interested in the general behavior of liquids and how they affect the collisional mechanism. To reproduce fully the exact experimental data, one may have to include many-body effects or at least use pair potentials that possess the long range periodic behavior common to liquid metals [11]. However, previous simulations showed that the detailed form of the potential does not play any important role as far as most sputtering features are concerned.

Target A was considered to be in the liquid state when the crystal structure could no longer be detected in cross sectional views of the target, and when the pair correlation function approached that of a typical liquid. We should note, however, the pair correlation function approached the general liquid form while crystal structure was still evident in the cross sectional views of the target.

The specific heat is related to the temporal fluctuation of the temperature by [12]:

$$C_v = (3/2)k_B\left[1 - (3/2)N\left(\langle T^2\rangle/\langle T\rangle^2 - 1\right)\right]^{-1}.$$

Here ⟨ ⟩ denotes a time average. and $N$ is the number of particles. Although the validity of this expression may be questionable for targets with only a few hundred particles, it gives a guideline for the amount of temperature fluctuation one might expect at equilibrium.

The diffusion coefficient was calculated as in [13] using:

$$D = \sum_{i=1}^{3N} \left[x_i(t) - x_i(0)\right]^2/6Nt.$$

Here $x_i(t)$ denotes the coordinate of the $i$th degree of freedom at time $t$. The time $t$ is usually taken around 400 fs. No significant change in $D$ was observed at different times once the system is in equilibrium. The surface tension was estimated by computing the surface potential energy per unit area of the surface monolayer. (At the temperature of our target, 1600 K, there is less than 20% difference between surface energy and surface tension values.) The calculated values for these properties are given together with experimental values in table 2. The experimental values for the specific heat of liquid Cu were not available.

Pair correlation function resulting from the simulation are shown along with the one obtained from neutron scattering data in fig. 4. Targets A and B both have liquid-like pair correlation functions that are not significantly different from each other. The positions of the first and second nearest neighbor peaks are in general agreement with that of experiment.

Density profiles for target B along the y-axis before and after cooling are shown in fig. 5. Target B developed adsorbed layers at the box walls within 200 fs after the box boundary conditions were applied without any cooling. After target B was cooled to 1600 K, it appeared to recrystallize into four separate layers. No such effects were observed for target A.

Table 2
Liquid properties

| | Target A | Target B | Experimental |
|---|---|---|---|
| Temperature (K) | 1600 | 1600 | |
| Specific heat ($k_B$) | 2.92 | 1.87 | – |
| Diffusion coeff. ($10^{-5}$ cm$^2$/s) | 29.5 | 3.61 | 6.027 [a]<br>(at 1533 K) |
| Surface energy (dyn/cm) | 2053 | 1285 | 1311 [b]<br>(at 1600 K) |

[a] Ref. [17].
[b] Ref. [18]

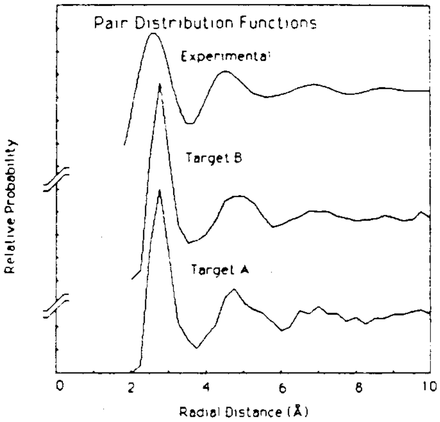

Fig. 4. Pair correlations for targets A and B resulting from molecular dynamics calculations along with one obtained from the experimental structure factor.

One possible qualitative explanation for the initial adsorbed layer at the walls is the following. The positive pressure causes bulk particles to approach the walls while particles at the walls are being reflected instanta-

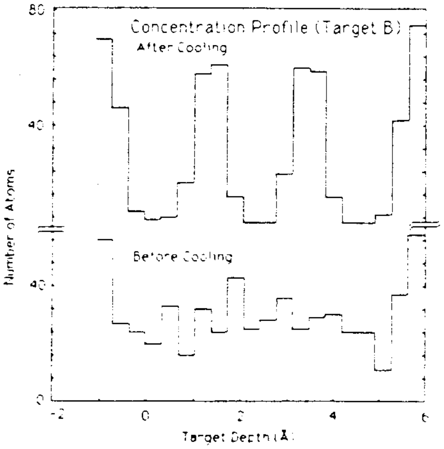

Fig. 5. Atomic concentration profiles along the beam direction (y-axis) for target B (box boundary conditions) before and after cooling

Table 3
Sputtering yields

| | Layer | Yield | Yield ratio |
|---|---|---|---|
| Target A | all | 2.94 (0.07) [a] | 1.00 |
| | 1 | 2.53 (0.05) | 0.86 (0.005) [a] |
| | 2 | 0.35 (0.01) | 0.12 (0.005) |
| | 3 | 0.05 | 0.02 |
| Target B | all | 5.05 (0.45) | 1.00 |
| | 1 | 4.75 (0.40) | 0.94 (0.005) |
| | 2 | 0.27 (0.04) | 0.05 (0.005) |
| | 3 | 0.03 | 0.01 |

[a] The quantities in parenthesis are estimated statistical uncertainties.

neously. The particles from the bulk approaching the walls do not respond quickly enough to redisperse the pressure surge at the walls, thereby maintaining an adsorbed layer. Surface adsorption at perfectly reflecting walls has been theoretically predicted [14].

## 6. Results

Sputtering simulations were carried out in which each target was exposed to 400 normally incident impacts of 5 keV $Ar^+$ ions. Each impact site was chosen so as to bombard uniformly a 4 × 4 Å area at the center of the target. In a real experiment, the damage to a liquid target during bombardment is expected to be minimal. In the simulations a virgin target is used for each impact, so target damage during sputtering is neglected.

For most parameters the uncertainties in the sputtering simulation results are largely statistical. (Absolute yields are an exception owing to lack of full containment of the collision cascade in the small targets that are used.) It has been suggested that the usual Poisson distribution of counting statistics generally overestimates the uncertainties in cases where the target impact area is scanned uniformly or quasi-uniformly [15]. Since it is not clear what type of distribution governs the uncertainties, no attempt was made to follow the error propagations. Instead the magnitude of the uncertainties was estimated by comparing two identical runs (except for impact locations) of 200 impacts for each target. The difference between the sputtering results were taken as a rough estimate of the uncertainties.

Table 4
Energy distribution parameters

| | $a$ | $b$(eV) | $c$ | $\chi^2$/deg of freedom |
|---|---|---|---|---|
| Target A | 42.200 | 4.49 (0.19) [a] | 3.50 (0.06) [a] | 1.56 |
| Target B | 19.050 | 2.49 (0.02) | 3.30 (0.09) | 2.07 |

[a] The quantities in parenthesis are estimated statistical uncertainties.

Table 5
Polar angular distribution parameters

| | Layer | $n$ | $\chi^2$/deg. of freedom |
|---|---|---|---|
| Target A | all | 1.99 (0.11) [a] | 2.19 |
| | 1 | 1.79 (0.15) | 2.46 |
| | 2 | 4.76 (0.68) | 2.74 |
| Target B | all | 3.17 (0.14) | 4.07 |
| | 1 | 3.07 (0.18) | 4.84 |
| | 2 | 5.28 (0.63) | 1.29 |

[a] The quantities in parentheses are estimated statistical uncertainties.

The total yield and yield ratio for each layer are given in table 3. The yield ratio for a layer is just the fraction of all ejected particles originating from that layer.

According to Thompson's linear cascade theory, the polar angular distribution should have a cos $\theta$ dependence ($\theta$ is the ejection angle relative to the surface normal), while the energy distribution of ejected atoms has the following form [16]:

$$N(E) = aE/(E+b)^c.$$

Here $a$ is a parameter independent of energy, $b$ is the surface binding energy, and $c$ is a parameter directly related to the decay characteristics of the atom–atom pair potential.

The cos $\theta$ dependence of the polar angular distribution has been shown repeatedly to be unrealistic by previous simulation and experimental work [1,2]. In our sputtering simulations, we have fitted the polar angular distribution results with a cosine power law of the form $\cos^n\theta$. Tables 4 and 5 give the energy and polar angular distribution parameters obtained by chi-square minimization.

## 7. Discussion

The total yield was notably higher for target B. This is consistent with its lower surface binding energy and surface tension. The total yields were exactly inversely proportional to the surface tensions of the two targets. In general, the absolute sputtering yields obtained from simulations with small targets underestimate the experimental values. However, the ratios of yields from individual target layers to total yields are much less dependent on target size (ref. [3]). The yield ratios obtained from target A (table 3) are in better agreement with Dumke's experimental results (ref. [1]) and with our previous results for solid Cu (ref. [3]), than those obtained from target B.

The polar angular distributions for target B had a

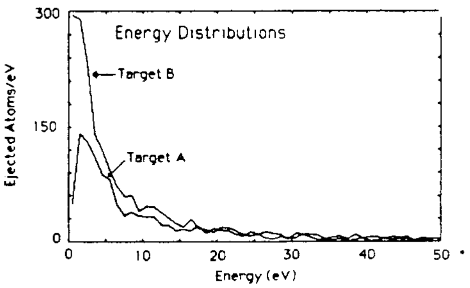

Fig. 6. Energy distributions resulting from molecular dynamics calculations of 400 impacts by 5 keV $Ar^+$ ions for targets A and B.

sharper peak while having a higher fractional yield from the surface layer. This may be attributable to the artificially smooth surface imposed by the box boundary conditions. While no data are available for liquid Cu, Dumke [1] found that the polar angular distributions of atoms sputtered by normally incident $Ar^+$ on both liquid In and liquid Ga targets were very close to $\cos^2\theta$. Again our simulation results from target A (semiperiodic boundary conditions) are very close to the experimental results (table 5).

The energy distribution for the two targets were distinctively different (see fig. 6). The binding energy obtained for target A was higher and closer to the experimental value of solid Cu. The reason for this appears to be that the top monolayer for target B is separated from bottom layers by a gap, leaving the surface particles weakly bound.

From these studies we have concluded that the semiperiodic boundary conditions results in thin liquid targets that are more suitable for sputtering simulations. The gap separating the surface layer in target B causes an artificially high yield of low energy particles. These gaps are not likely to exist in real liquid systems. The box boundary conditions also produce an artificially smooth surface layer. The semiperiodic boundary conditions allow the liquid surface to evolve freely and therefore represents a more realistic system.

We wish to thank Professor Don L. Harrison Jr and Dr. Peter K. Haff for many helpful discussions during the course of this work. The support of the staffs of the California State University Data Center and the California State University, Fullerton Computer Center is gratefully acknowledged.

## References

[1] M.F. Dumke, T.A. Tombrello, R.A. Weller, R.M. Housley, and E.H. Cirlin, Surf. Sci. 124 (1983) 407.
[2] M.H. Shapiro, D.Y. Lo, P.K. Haff, and T.A. Tombrello, Nucl. Instr. and Meth. B13 (1986) 348.
[3] M.H. Shapiro, P.K. Haff, T.A. Tombrello, D.E. Harrison Jr, and R.P. Webb, Radiat. Eff. 89 (1985) 243.
[4] M.H. Shapiro, P.K. Haff, T.A. Tombrello, and D.E. Harrison Jr, Nucl. Instr. and Meth. B12 (1985) 137.
[5] M.H. Shapiro, Technical Report BB-1, California Institute of Technology, (1983).
[6] P.A. Egelstaff, An Introduction to the Liquid State (Academic Press, London and New York, 1967).
[7] I.M. Torrens, Interatomic Potentials (Academic Press, New York, 1972).
[8] J.K. Lee, Interatomic Potentials and Crystalline Defects (The Metallurgical Society of AIME, New York, 1981).
[9] M. Breuil and G. Tourand, J. Phys. Chem. Solids 31 (1970) 549.
[10] L.A. Girifalco and V.G. Weizer, Phys. Rev. 114 (1959) 687.
[11] J.M. Gonzalez Miranda and V. Torra, J. Phys. F13 (1983) 281.
[12] J.L. Lebowitz, J.K. Percus and L. Verlet, Phys. Rev. 153 (1967) 250.
[13] F. Reif, Fundamentals of Statistical and Thermal Physics (McGraw-Hill, New York, 1965).
[14] P. Ballone and G. Pastore, J. Stat. Phys. 38 (1985) 861.
[15] D.E. Harrison Jr, private communication.
[16] M.W. Thompson, Phys. Rep. 69 (1981) 337.
[17] J. Henderson and L. Yang, Trans. Am. Inst. Min. Metall. Engrs. 221 (1961) 72.
[18] R.C. Weast (ed.), CRC Handbook of Chemistry and Physics (CRC Press, Inc. Boca Raton, Florida, 1983).

348 Nuclear Instruments and Methods in Physics Research B13 (1986) 348-352
North-Holland, Amsterdam

# SIMULATION OF SPUTTERING FROM LIQUID Cu TARGETS*

M.H. SHAPIRO

*Department of Physics, California State University, Fullerton, CA 92634, USA and Department of Physics, California Institute of Technology, Mail Code 301-38, Pasadena, CA 91125, USA*

D.Y. LO, P.K. HAFF and T.A. TOMBRELLO

*Department of Physics, California Institute of Technology, Mail Code 301-38, Pasadena, CA 91125, USA*

The sputtering of Cu atoms from liquid targets by normally incident 5 keV $Ar^+$ ions was simulated using the multiple interaction molecular dynamics technique. Yields, energy distributions, and angular distributions of sputtered atoms were obtained at several temperatures slightly above and below the experimental melting point of copper. In all cases the resulting angular distributions of ejected atoms peaked more sharply than the cos $\theta$ behavior predicted by linear cascade theory. The ratio of yields from individual layers of the liquid targets, and the energy and angular distributions of ejected atoms generally were found to be similar to those obtained in previous simulations with solid Cu targets. Our results also are in qualitative agreement with Dumke's measurements of angular distributions and layer yield ratios of sputtered atoms from liquid Ga–In eutectic alloy targets. In particular, no marked changes in yields or energy distributions were observed when the temperature of the target was lowered below the nominal melting point of copper. The angular distributions were found to broaden with increasing temperature.

## 1. Introduction

Although the vast majority of experimental sputtering data have been obtained from solid targets, there are some distinct advantages in studying sputtering from liquid metal targets. First, the present theoretical treatments of sputtering [1] generally assume bulk isotropy and a perfectly smooth target surface. Ion bombardment of solid targets can cause changes in surface structure and composition that complicate comparisons with these theoretical treatments. This is particularly true in the case of sputtering from multicomponent targets. The diffusion rate in liquid metal targets is generally large enough to keep surface properties constant during bombardment, thereby eliminating these effects.

Second, the depth of origin of sputtered atoms can be determined by using specific two component liquid metal targets. For example, Dumke investigated sputtering from liquid Ga–In eutectic alloys [2] where Gibbsian surface segregation resulted in the formation of a surface monolayer of indium that was maintained during bombardment with $Ar^+$ ions. From these experiments Dumke was able to determine that at a bombarding energy of 15 keV more than 85% of the ejected atoms came from the first layer of the target, and that the angular distribution of sputtered atoms which originated below the first layer was much sharper than that of atoms sputtered from the first layer.

A third reason for simulating sputtering from a liquid target is the possibility of observing phase dependent effects near the solid–liquid melting point.

Dumke's experiment prompted a computer study of the angular and energy distributions of atoms ejected from different layers of a solid monocrystalline target [3]. The results agreed qualitatively with those of Dumke. The present simulation study is an attempt to duplicate more closely the liquid environment present in Dumke's experiments.

In the present simulation, liquid targets with approximately 600 Cu atoms were bombarded by 5 keV $Ar^+$ ions at normal incidence. The Ar–Cu system was chosen because the solid phase has been studied extensively, and data for the ion–atom and atom–atom potentials were readily available [3–5]. Details of the simulation procedure are given below.

## 2. Simulation code

All of the simulation results in this paper were obtained with the multiple interaction molecular dynamics code SPUT1 which had been used previously to simulate sputtering from crystalline copper [3, 6]. The code was run on the CYBER-730/760 system of the State University Data Center in Los Angeles. In SPUT1 the system of particles is assumed to interact classically under the influence of pair potentials. The Newtonian equations of motion are integrated with a

---

* Supported in part by the National Science Foundation [DMR83-06541 (Caltech) and DMR83-06548 (CSUF)], the Alexander von Humbolt Foundation, and Schlumberger-Doll Research.

simple predictor–corrector algorithm. The time step is adjusted during the integration to optimize the computational speed while maintaining a pre-determined level of accuracy.

The SPUT1 code includes several standard generators for crystalline targets that were developed originally by Harrison and co-workers [7]. For these simulations, however, it was necessary to generate targets which possessed the appropriate liquid properties. Since this turned out to be a relatively complicated procedure, only a brief description of the liquid target generator is given below. A more complete discussion of the issues involved in developing thin liquid target models suitable for sputtering simulations is given in a separate paper [8].

## 3. Target generation

The liquid targets used in these sputtering simulations were generated with semi-periodic boundary conditions. The Cu atoms initially were located on a fcc lattice with the lattice constant chosen to produce the appropriate density for liquid Cu. Initial velocity components were assigned randomly to each atom from a Gaussian random number distribution. The target was then allowed to evolve under the influence of pair potentials using the same basic time step logic present in SPUT1. Heat was added by uniformly scaling the velocities until a liquid state was reached. Velocity scaling was also used to adjust the temperature of the target once melting had occurred.

Periodicity was demanded in two directions, while in the third (normal to the sputtering surface) only surface tension (as provided by the interatomic forces) constrained the target atoms. This particular choice of boundary condition resulted in target surfaces with properties close to those of real liquids [9]. The targets were allowed to evolve until quasi-equilibrium was obtained as indicated by a zero temperature gradient, with temperature fluctuations of the order of 5%. This corresponded to specific heats of about $3k_B$, which is reasonable for liquid Cu [10].

Several hours of CPU time (corresponding to a few tens of picoseconds) were needed to equilibrate one of these liquid targets. To minimize the computer time needed to simulate sputtering from the liquid surface, the liquid target configuration (position and velocity components for each atom) was saved in a file which served as input to the SPUT1 program. During the sputtering runs the semi-periodic boundary conditions were removed. Since the time needed for the development of collision cascades is much shorter than the time required to achieve equilibrium of the liquid target, this procedure had little effect on the sputtering results. To avoid the need to generate a new liquid target before each simulated impact, a square target impact area was scanned. Before each impact the original liquid target configuration was restored by reading in the target file anew.

## 4. Potentials

Initial attempts to obtain atom–atom pair potentials for liquid Cu by inverting experimental structure factor data proved unsuccessful [8]. The atom–atom pair potential that ultimately was adopted for both the liquid target generation and sputtering simulation was a Moliere core joined to a Morse well by a cubic spline. This form of the atom–atom potential has been used widely in previous sputtering simulations [7].

It was possible to adjust the parameters of this potential both to obtain reasonable fits to the bulk

Table 1
Potential parameters

| | |
|---|---|
| Ion–atom | |
| $V_{ij} = (A/r)[0.35e^{-0.3r/B} + 0.55e^{-1.2r/B} + 0.1e^{-6r/B}]$ | $r < r_a$ |
| $V_{ij} = 0$ | $r \geq r_a$ |
| $A = 6.01406$ keV Å | |
| $B = 0.103481$ Å | |
| $r_a = 2.556$ Å | |
| Atom–atom | |
| $V_{ij} = (A/r)[0.35e^{-0.3r/B} + 0.55e^{-1.2r/B} + 0.1e^{-6r/B}]$ | $r < r_a$ |
| $V_{ij} = C_0 + C_1 r + C_2 r^2 + C_3 r^3$ | $r_a \leq r < r_b$ |
| $V_{ij} = D_e[e^{-2\beta(r-r_e)} - 2e^{-\beta(r-r_e)}]$ | $r_b \leq r < r_c$ |
| $V_{ij} = 0$ | $r \geq r_c$ |
| $A = 9.689326$ eV Å, $B = 0.096027$ Å | |
| $C_0 = 597.3$ eV, $C_1 = -814$ eV/Å, $C_2 = 371.7$ eV/Å$^2$, $C_3 = -57$ eV/Å$^3$ | |
| $D_e = 0.37$ eV, $\beta = 1.359$ Å$^{-1}$, $r_e = 2.866$ Å | |
| $r_a = 1.5$ Å, $r_b = 1.988$ Å, $r_c = 5.25$ Å (sputtering) | |
| $r_c = 12$Å (target generation) | |

properties of liquid Cu, and to obtain a pair correlation function that was close to the experimental values. During the target generation the atom–atom potential was cut off at 12 Å, while during sputtering runs it was cut off at 5 Å in order to reduce the time needed for computation. Since the other parameters were not changed, this procedure had the effect of reducing the binding energy slightly during sputtering runs.

A Moliere potential with a cut-off radius of 2.5 Å was used to represent the ion–atom interaction. The potential functions and parameters are given in table 1.

## 5. Results

A summary of the properties of the liquid targets used in the simulation runs is given in table 2. These have been ordered by increasing total internal energy from −1681 to −1591 eV corresponding to nominal temperatures ranging from 1180 to 1622 K. A total of 400 impacts were simulated for each of these targets in order to obtain yields, energy distributions, and polar angular distributions. The yield results are summarized in table 3. Both the total yields and the yields of ejected atoms from individual target layers are remarkably similar to the averages of those found in simulations with solid, crystalline copper targets [3]. The statistical uncertainty in the total yields is estimated to be about 15%. No systematic change in yield with increasing temperature was observed.

As noted in ref. [3], the absolute yields from simulations with these small targets will be less than the experimental yields owing to a lack of full containment for some cascades. However, the ratio of yields from the individual target layers are expected to be much less dependent on target size for targets in excess of 200 atoms [11]. In these simulations an average of 81% of the ejected atoms came from the first atomic layer of the target. This is quite consistent with the experimental observations of Dumke [2] and our previous simulation with solid copper [3].

A typical distribution of ejected atoms versus energy

Table 2
Properties of targets used in simulation runs

| Target | No. of atoms | Temperature (K) | Total energy (eV) | Density ($Å^{-3}$) |
|---|---|---|---|---|
| 606 | 603 | 1180 | −1681 | 0.075 |
| 573 | 603 | 1309 | −1647 | 0.076 |
| 598 | 603 | 1376 | −1619 | 0.073 |
| 583 | 603 | 1622 | −1591 | 0.076 |

Table 3
Sputtering yields

| Target | No. of atoms | Temperature (K) | Layer | Yield | Yield ratio |
|---|---|---|---|---|---|
| 606 | 603 | 1180 | All | 3.01 | 1.00 |
| | | | 1 | 2.55 | 0.85 |
| | | | 2 | 0.40 | 0.13 |
| | | | 3 | 0.06 | 0.02 |
| 573 | 603 | 1309 | All | 2.40 | 1.00 |
| | | | 1 | 1.99 | 0.83 |
| | | | 2 | 0.36 | 0.15 |
| | | | 3 | 0.04 | 0.02 |
| 598 | 603 | 1376 | All | 3.33 | 1.00 |
| | | | 1 | 2.30 | 0.69 |
| | | | 2 | 0.94 | 0.28 |
| | | | 3 | 0.08 | 0.02 |
| 583 | 603 | 1622 | All | 2.94 | 1.00 |
| | | | 1 | 2.53 | 0.86 |
| | | | 2 | 0.35 | 0.12 |
| | | | 3 | 0.05 | 0.02 |
| Solid Cu[a] | 525 | 0 | All | 3.04 | 1.00 |
| | | | 1 | 2.69 | 0.88 |
| | | | 2 | 0.31 | 0.10 |

[a] Obtained by averaging the yields from the (100), (110), and (111) orientations of ref. [3]

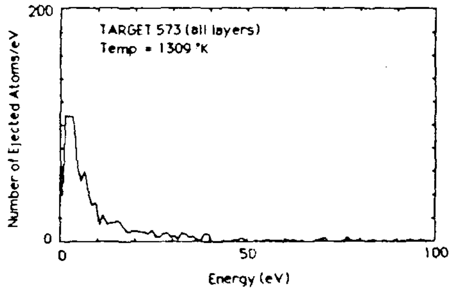

Fig. 1. Energy spectrum obtained from a simulation with 400 Ar⁺ ions normally incident on a 603 atom "liquid" Cu target with a nominal temperature of 1309 K. The binning width is 0.25 eV.

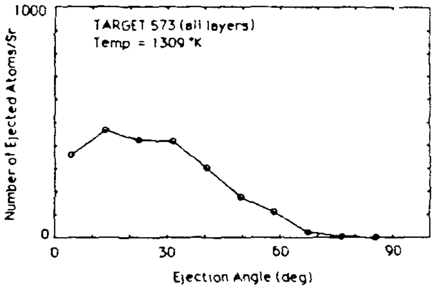

Fig. 2. Polar angular distribution of ejected particles obtained from a simulation with 400 Ar⁺ ions normally incident on a 603 atom "liquid" Cu target with a nominal temperature of 1309 K. The binning width is 9 degrees.

for one of the liquid targets is shown in fig. 1. Transport theory [1] predicts that the shape of this distribution should have the form $N(E) = AE/(E + E_b)^n$, where $A$ is a parameter independent of energy, $E_b$ is the surface binding energy, and $n$ is equal to 3 for hard sphere scattering. This leads to the well known $E^{-2}$ shape on the tail of the energy distribution.

For each of the targets listed in table 2, those values of the three parameters which produced the best fit to the energy distributions obtained from the simulations were obtained from the simulations were obtained by $\chi^2$-minimization [3]. The results are summarized in table 4. In general, the values for $n$ and $E_b$ obtained for the liquid targets are close to those obtained in ref. [3] from crystalline targets at 0 K. For the crystalline targets average $n$ and $E_b$ values of 3.2 and 5.0 eV were obtained, while for the liquid targets these values were 3.5 and 4.5 eV respectively. The small differences most likely result from the different potential parameters assumed for the liquid targets.

A typical polar angular distribution of ejected atoms obtained from one of our simulations is shown in fig. 2. Both the angular distributions of ejected atoms from the individual target layers and from the entire target were fitted with a cosine power law ($\cos^n \theta$) for each of the simulations. The results are summarized in table 5.

In general the angular distributions are considerably "over-cosine". The angular distributions of atoms ejected from the second atomic layer of the targets are much more forward peaked than those from the first atomic layers. These results are in agreement both with the solid copper simulation [3], and with Dumke's experimental results [2].

Table 4
Energy spectra parameters

| Target | $A$ | $n$ | $E_b$ (eV) | $\chi^2$/deg of freedom |
|---|---|---|---|---|
| 606 | 39 450 | 3.55 | 4.52 | 1.31 |
| 573 | 40 750 | 3.47 | 4.58 | 1.42 |
| 598 | 41 850 | 3.45 | 4.48 | 2.45 |
| 583 | 40 650 | 3.48 | 4.52 | 1.69 |

Table 5
Results of $\cos^n \theta$ fits to polar angular distributions

| Target | Temperature (K) | Layer | $n$ |
|---|---|---|---|
| 606 | 1180 | All | 2.72 |
| | | 1 | 2.45 |
| | | 2 | 5.15 |
| 573 | 1309 | All | 2.95 |
| | | 1 | 2.65 |
| | | 2 | 5.37 |
| 598 | 1376 | All | 2.51 |
| | | 1 | 1.98 |
| | | 2 | 6.11 |
| 583 | 1622 | All | 1.99 |
| | | 1 | 1.78 |
| | | 2 | 4.76 |

Both the first layer and total target angular distributions show a trend toward broadening with increased temperature. The two lower temperature first layer angular distributions were fitted best with $n$ about 2.5, while the two higher temperature first layer distributions required an $n$ value less than 2.

## 6. Discussion

The absence of a strong temperature dependence for the sputtering yield is to be expected. Even at the relatively high temperatures for the targets used in these simulations, the average kinetic energy for a given copper atom is only about 0.1 eV. Since individual atoms are bound by close to 5 eV at the surface and by close to 7 eV in the bulk [12], the additional kinetic energy contributed by thermal motion is inconsequential as far as the yields are concerned.

The broadening of the angular distributions of ejected atoms with increasing temperature probably results from surface roughening on a very small scale. Individual atoms (or small groups of atoms) which project from the mean surface plane at the instant they are struck by another atom in the collision cascade, can scatter at larger angles than would be permitted if the surface were perfectly smooth.

## References

[1] M.W. Thompson, Phys. Reports 69 (1981) p. 337.
[2] M.F. Dumke et al., Surface Sci. 124 (1983) p. 407.
[3] M.H. Shapiro et al., Radiat. Effects 89 (1985) p. 234
[4] L.A. Girifalco and V.G. Weizer, Phys. Rev. 114 (1959) p. 687.
[5] I.M. Torrens, Interatomic Potentials (Academic Press, New York, 1972).
[6] M.H. Shapiro et al., Nucl. Instr. and Meth. B12 (1985) 137.
[7] D.E. Harrison Jr, Radiat. Effects 70 (1983) 1.
[8] D.Y. Lo, T.A. Tombrello and M.H. Shapiro, Nucl. Instr. and Meth B, submitted.
[9] P.A. Egelstaff, An Introduction to the Liquid State (Academic Press, London and New York, 1967).
[10] J.L. Lebowitz, J.K. Percus and L. Verlet, Phys. Rev. 153 (1967) p. 250.
[11] D.E. Harrison Jr, in: Proc. Symp. on Sputtering, eds., P. Varga, G. Betz and F.P. Viehbock (Perchtoldsdorf, Vienna, 1980) p. 36.
[12] M.T. Robinson, in: Sputtering by Particle Bombardment I, ed., R. Behrisch (Springer, Berlin, 1981) p. 74.

# Chapter 4 - Sputtering from Liquid InGa

## 4.1 Introduction

The first quantitative experimental evidence that the majority of the sputtered atoms come from the first surface monolayer during low-energy ion bombardment came from Dumke's experiment [1]. Dumke et al. sputtered a liquid InGa eutetic alloy with 15 keV and 25 keV $Ar^+$ ions. The InGa eutetic has a surface layer that is predominantly In because of Gibbsian segregation [2]. *Ion Scattering Spectrometry* (ISS) measurements show a surface monolayer consisting of 97% In for an InGa sample with a bulk composition of 83.5% Ga. The determination of the surface composition by ISS in conjunction with partial Ga and In sputtering yields, obtained by the collector foil method and subsequent *Rutherford Backscattering Spectrometry* (RBS) analysis, allowed Dumke to deduce that 85% and 70% of the sputtered atoms originate from the first surface monolayer for the 15 keV and 25 keV cases, respectively. Recent experiments by Hubbard et al. [3] on the same InGa system concluded that 94%, 88%, and 87% of the sputtered atoms originate from the first monolayer for incident $Ar^+$ ion energies of 3 keV, 25 keV, and 50 keV, respectively.

Angular distributions were also obtained in the above experiments and fitted to a cosine power law ($\cos^n\theta$). In all experiments the In angular distribution gave an **n** value close to 2 for all energies. For the Ga angular distributions, a discrepancy exists between the two experiments at 25 keV bombarding ion energy. Dumke's measurement gave **n** values of 3.6 for the 15 keV ion and 2 for the 25 keV ion, while Hubbard obtained **n** values of 4.9 for the 3 keV ion and 3.2 for both the 25 keV and 50 keV ions. The trend in both experiments is clearly a much sharper angular distribution for Ga at low bombarding ion energies and a broadening of the Ga angular distribution with increasing ion energy.

Qualitative agreement of these experiments with our previous simulation of sputtering from liquid Cu suggests that sputtering experiments with binary targets may yield conclusions that are also applicable to single-element targets. In order to give more concrete support to the experimental results, we have simulated sputtering by 5 keV $Ar^+$ ion bombardment of a pseudoliquid InGa target that is 100% In in the first surface monolayer and 100% Ga in the subsequent layers. The goal is to take into account both mass and interatomic force differences between the In and Ga atoms and to show that these factors do not change the general conclusions drawn from the liquid Cu simulations.

## 4.2 Summary

The Morse potentials used for this simulation have been chosen in an ad hoc fashion. The In-In and Ga-Ga Morse parameters were obtained by extrapolating from the corresponding Al parameters, given by Girifalco and Weizer [4], using an empirical method described in Appendix 4.1. It is interesting to note that the In-In Morse parameters obtained by this empirical method (Tab. 1 of App. 4.1) are very close to those obtained by direct fit to crystal properties (Tab. 1 of App. 5.1). The In-Ga parameters are obtained by a linear interpolation. This method of obtaining interatomic forces between unlike atoms is, of course, completely unfounded. However, except for the well depth, one would expect the other two Morse parameters to be bounded by the cooresponding parameters [5] of the pure metals, which are very close to each other in this case. The well depth will depend on the heat of mixing between In and Ga, which was not available at the time of this simulation. A more precise way of describing interactions in metals and alloys is to use interactions that include many-body forces such as the *embedded-atom method* (EAM) [6,7], (Chapter 7).

Since we were mainly interested in sputtering and not in the segregation process, the Gibbsian segregation was, for simplicity, artificially imposed as described in Appendix 4.1, and thus this is really a simulation of sputtering from *pseudo*-InGa.

Simulation results for the liquid InGa target are in good agreement with experiments. The fraction of sputtered atoms originating from the first surface monolayer is in accord with experiments [1,3] and previous simulation with liquid Cu targets (Chapter 3). These results are shown in Table 4-1 for comparison.

**Table 4-1:** Comparison of first-layer fractional yields.

| Simulation/ Experiment | Ion Energy (keV) | Fraction From First Layer |
|---|---|---|
| Cu (simul.)* | 5 | 81% |
| InGa (simul.) | 5 | 88% |
| InGa (exp. Dumke) | 15 | 85% |
| | 25 | 70% |
| InGa (exp. Hubbard) | 3 | 94% |
| | 25 | 88% |
| | 50 | 87% |

* This is an average over simulations with liquid Cu targets at different temperatures (Tab. 3 of App. 3.2).

Simulation of sputtering from the liquid InGa target clearly results in a broader angular distribution for the In atoms (Fig. 1 of App. 4.1). The In atoms in this case come entirely from the first-surface monolayer. Agreement with the liquid Cu simulation and liquid InGa experiments at low ion bombarding energies is shown in Table 4-2. The origin of the discrepancy between the Dumke and Hubbard experiments at high ion energies (above 15 keV) is not clear. One explaination of Dumke's Ga angular distribution broadening with increasing bombarding energy is that the atoms from below the first layer (predominantly Ga) have higher energies and hence, the difference in energy lost between normal and grazing directions of ejection becomes relatively less apparent to the ejecting subsurface atoms. This trend is also clearly exibited by Hubbard's experiment when the ion energy is increased from 3 to 25 keV.

**Table 4-2:** Comparison of the $\cos^n\theta$ fit to angular distributions.

| Simulation/ Experiment | Ion Energy (keV) | Parameter | n |
|---|---|---|---|
| Cu (simul.)* | 5 | first layer | 2.2 |
| | | second layer | 5.3 |
| InGa (simul.) | 5 | In | 2 |
| | | Ga | 4 |
| InGa (exp. Dumke) | 15 | In | 2.0 |
| | | Ga | 3.7 |
| | 25 | In | 1.98 |
| | | Ga | 2.0 |
| InGa (exp. Hubbard) | 3 | In | 1.8 |
| | | Ga | 4.9 |
| | 25 | In | 1.8 |
| | | Ga | 3.3 |
| | 50 | In | 1.8 |
| | | Ga | 3.2 |

* This is an average over simulations with liquid Cu targets at different temperatures (Tab. 5 of App. 3.2).

The general agreement with the liquid Cu target simulations and experiments of Dumke and Hubbard supports the assumption that the InGa experimental conclusions regarding depth of origin and angular distribution of sputtered atoms are universal and applicable to single element targets as well.

## References

1. M. F. Dumke, T. A. Tombrello, R. A. Weller, R. M. Housley, and E. H. Cirlin, Surf. Sci. **124**, 407 (1983).

2. J. C. Hamilton, Phys. Rev. Lett. **42**, 989 (1979).

3. K. M. Hubbard, R. A. Weller, D. L. Weathers, and T. A. Tombrello, Nucl. Instr. and Meth., to appear in the Proceedings of the Accelerator Conference (1988).

4. L. A. Girifalco and V. G. Weizer, Phys. Rev. **114**, 687 (1959).

5. E. Q. Grundke, D. Henderson, and R. D. Murphy, Can. J. Phys. **49**, 1593 (1971).

6. M. S. Daw and M. I. Baskes, Phys. Rev. **B 29**, 6443 (1984).
7. S. M. Foiles, Phys. Rev. **B 32**, 7685 (1985).

# COMPUTER SIMULATION OF SPUTTERING FROM TWO COMPONENT LIQUID METAL TARGETS

M.H. SHAPIRO*, D.Y. LO** AND T.A. TOMBRELLO**
*Physics Dept., California State University, Fullerton, CA 92634, U.S.A. and Division of Physics, Mathematics and Astronomy, Caltech, Pasadena, CA 91125, U.S.A.
**Division of Physics, Mathematics and Astronomy, Caltech, Pasadena, CA 91125, U.S.A.

## ABSTRACT

The sputtering of In and Ga atoms from a "liquid" target composed of gallium covered by a surface monolayer of indium by incident 5 keV $Ar^+$ ions was simulated using the multiple interaction molecular dynamics technique. Yields, energy distributions, and angular distributions of sputtered atoms were obtained at a temperature above the melting point for the eutectic alloy. Similar information was obtained for a pure gallium and a pure indium target. Our results for layer yield ratios and angular distributions are in good qualitative agreement with Dumke's experimental data for the $Ar^+$, In-Ga system. Absolute yields, however, were found to be sensitive to the detailed nature of the two-body potentials used to describe the atom-atom interactions.

## INTRODUCTION

Although most experimental sputtering data have been obtained from solid targets, important experimental information about the fundamental nature of the sputtering process has been obtained by sputtering from liquid metal targets. For example, Dumke [1] has shown by bombarding liquid In-Ga eutectic targets with 15 and 25 keV $Ar^+$ ions that (1) Gibbsian surface segregation resulted in the formation of a surface monolayer of indium that was maintained during bombardment, and (2) that the large majority of sputtered atoms had their origin in this surface layer. In two previous papers [2,3] we have investigated the generation of thin liquid Cu targets for use in sputtering simulation, and we have used them to simulate sputtering by normally incident 5 keV $Ar^+$ ions. Generally, those results were in good qualitative agreement with Dumke's experimental data. The present study is an attempt to more closely simulate the conditions of Dumke's experiment in order to determine which

Mat. Res. Soc. Symp. Proc. Vol. 63

features of his results were general and which were dependent on the specific system which he studied.

## SIMULATION CODE

Our simulation results have been obtained with the multiple interaction code SPUT1 which has been used previously to simulate sputtering from liquid and crystalline copper [2,3,4,5]. The code was run on the CYBER 730/760 system at the State University Data Center in Los Angeles. In SPUT1 the system of particles is assumed to interact classically under the influence of pair potentials. The Newtonian equations of motion are integrated with a simple predictor-corrector algorithm. The time step is adjusted during the integration to optimize the computational speed while maintaining a pre-determined level of accuracy.

The pure gallium liquid target used in these simulations was generated with semi-periodic boundary conditions using a modified version of the SPUT1 code [2]. The Ga atoms initially were located on an fcc lattice with the lattice constant chosen to produce the appropriate density for liquid Ga. Initial velocity components were assigned randomly to each atom from a Gaussian random number distribution. The target was then allowed to evolve under the influence of pair potentials. Heat was added by uniformly scaling the velocities until a liquid state was reached. Velocity scaling also was used to adjust the temperature of the target once melting had occurred.

Periodicity was demanded in two directions, while in the direction normal to the sputtering surface only the surface tension provided by the interatomic forces constrained the target atoms. The target was allowed to evolve until quasi-equilibrium was obtained as indicated by a zero temperature gradient, with reasonable temperature fluctuations. To minimize the computer time needed to simulate sputtering from the liquid surface, the liquid target configuration (position and velocity components for each atom) were saved in a file which served as input to the SPUT1 program.

The pure indium target was prepared in the same manner as the pure gallium target, while the In-Ga eutectic target was made by changing the mass of atoms within one atomic layer of the front surface from that of gallium to that of indium after the target was equilibrated. While the latter procedure was somewhat artificial, it allowed us to investigate the effects of monolayer indium coverage within the constraints of available computer resources.

POTENTIALS

In our previous studies [2,3] we had found that it was not possible to obtain reliable two-body potentials for liquid Cu by inverting structure factor data. However, semi-empirical potentials (a Moliere core joined to a Morse well by a cubic spline) produced reasonable results in the copper case. The same approach was used for this study. The two-body atom-atom potentials were obtained by joining standard Moliere potentials [6] to Morse wells with cubic splines. Since no parameters for the Morse potentials for the three needed cases (Ga-Ga, In-In, and In-Ga) were readily available in the literature, an extrapolation procedure was used to obtain values for the various parameters.

We found that when parameters for atoms in the same column of the periodic table were plotted against the atomic number (see Table 4.1 of ref. [6]), the variation in the parameter values was small. Plots were made of the values of the three parameters, and the results were found to lie on smooth curves that were roughly parallel. Using the parameters for aluminum to establish the location of similar curves for the Al-Ga-In case, we were able to obtain Morse potential parameters for gallium and indium. The In-Ga parameters then were obtained by interpolation. Standard Moliere potentials were used to simulate the ion-atom interactions. The potential parameters are given in Table I.

Table I
Potential Parameters

| | |
|---|---|
| Ion-atom | |
| $V_{ij} = (A/r)[0.35e^{-0.3r/B} + 0.55e^{-1.2r/B} + 0.1e^{-6r/B}]$ | $r < r_a$ |
| $V_{ij} = 0$ | $r \geq r_a$ |
| A = 8046. eV Å  B = 0.10223 Å  $r_a$ = 2.868 Å | Ar-Ga |
| A = 12701 eV Å  B = 0.09335 Å  $r_a$ = 2.868 Å | Ar-In |
| Atom-atom | |
| $V_{ij} = (A/r)[0.35e^{-0.3r/B} + 0.55e^{-1.2r/B} + 0.1e^{-6r/B}]$ | $r < r_a$ |
| $V_{ij} = C_0 + C_1r + C_2r^2 + C_3r^3$ | $r_a \leq r < r_b$ |
| $V_{ij} = D_e[e^{-2b(r-r_e)} - 2e^{-b(r-r_e)}]$ | $r_b \leq r < r_c$ |
| $V_{ij} = 0$ | $r \geq r_c$ |

Ga-Ga:
A = 13857. eV Å  B = 0.93947 Å

Table I (cont.)

$C_0 = 60.59$ eV $C_1 = -56.83$ eV/Å $C_2 = 17.8921$ eV/Å$^2$
$C_3 = -1.900$ eV/Å$^3$ $D_e = 0.29$ eV $b = 1.11$ Å$^{-1}$
$r_e = 3.45$ Å $r_a = 2.20$ Å $r_b = 3.10$ Å

$r_c = 5.25$ Å (sputtering) $r_c = 12$ Å (target generation)

In-Ga:
$A = 21874.$ eV Å $B = 0.08667$ Å
$C_0 = 4.742$ eV $C_1 = -0.8610$ eV/Å $C_2 = -0.7460$ eV/Å$^2$
$C_3 = 0.1659$ eV/Å$^3$ $D_e = 0.30$ eV $b = 1.09$ Å$^{-1}$
$r_e = 3.57$ Å $r_a = 2.75$ Å $r_b = 3.25$ Å
$r_c = 5.25$ Å (sputtering) $r_c = 12$ Å (target generation)

In-In:
$A = 34574.$ eV Å $B = 0.08065$ Å
Spline 1:
$C_0 = 6.197$ eV $C_1 = -3.3233$ eV/Å $C_2 = -0.3681$ eV/Å$^2$
$C_3 = 0.01475$ eV/Å$^3$ $r_a = 2.75$ Å $r_b = 3.25$ Å
Spline 2:
$C_0 = 6063.32$ eV $C_1 = -11667.$ eV/Å $C_2 = 7506.9$ eV/Å$^2$
$C_3 = -1607.42$ eV/Å$^3$ $r_a = 1.03$ Å $r_b = 1.36$ Å

$D_e = 0.31$ eV $b = 1.07$ Å$^{-1}$
$r_e = 3.57$ Å
$r_c = 5.25$ Å (sputtering) $r_c = 12$ Å (target generation)

---

## RESULTS

Because of space limitations, in this paper we shall limit our discussion primarily to the In-Ga case. Figure 1 shows the angular distributions of sputtered In and Ga atoms from the In-Ga target resulting from 800 impacts with 5 keV Ar$^+$ ions. In this simulation the indium atoms are constrained to arise from the first layer, while almost all sputtered gallium atoms arise from the second layer. The indium angular distribution is considerably "over-cosine" in good agreement with Dumke's experimental observation (at 15 keV bombarding energy) that the sputtered indium angular distribution was fitted well with a $\cos^2\theta$ curve. The gallium angular distribution is even more sharply forward peaked, which is in good agreement with the $\cos^4\theta$ distribution measured by Dumke.

Yield information is given in Table II. Because of the low-yield obtained with the pure indium target, layer yield information is given only for the pure gallium and indium-gallium eutectic cases.

Table II
Sputtering Yields

| Target | # of atoms | Temp (K) | Layer | Yield | Yield Ratio | Experimental Value [1] |
|---|---|---|---|---|---|---|
| Ga | 612 | 401. | All | 2.06 | 1.00 | |
| | | | 1 | 1.81 | 0.88 | |
| | | | 2 | 0.22 | 0.11 | |
| In-Ga | 171 (In) | | All | 1.44 | 1.00 | |
| | 441 (Ga) | 401. | 1 | 1.26 | 0.88 | 0.85[1] |
| | | | 2 | 0.15 | 0.10 | 0.15[2] |
| In | 612 | 474. | All | 0.60[3] | | |

[1] Includes all sputtered In atoms.
[2] Includes all sputtered Ga atoms.
[3] Obtained using spline 1.

## DISCUSSION

Our liquid In-Ga eutectic simulation results support the argument that the large majority of atoms sputtered by low energy ion bombardment arise from the first layer of the target. The angular distributions of sputtered indium and gallium atoms show a behavior quite similar to the experimental results of Dumke [1]; however, the absolute yields given in Table II do not follow the same pattern observed by Dumke. In his experimental work, there was very little difference in total absolute yields for the pure liquid gallium and indium targets and the liquid indium-gallium eutectic target. In fact a slightly higher yield was observed for the pure indium case in the experimental work.

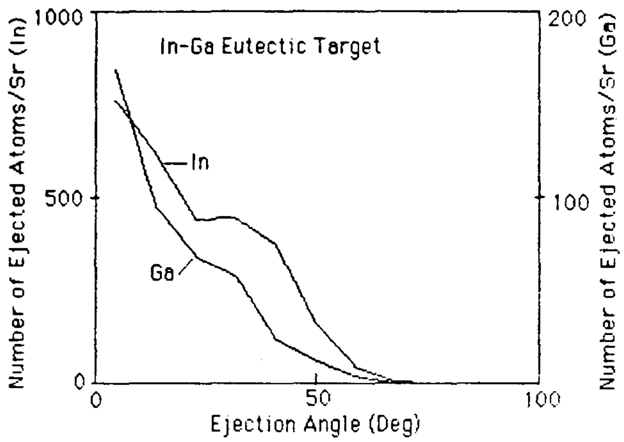

Figure 1
Angular Distributions of Sputtered Indium and Gallium Atoms

We observed very little difference in absolute yields for the two different splines used with the indium potentials, and we suspect that the yield problems is caused by improper depths for three potentials used. Further work is underway to investigate this possibility[4]. In addition, work also is underway to simulate the formation of liquid indium-gallium eutectic targets directly.

[4])Note added in proof:

Although changes in potential depth altered absolute yields slightly, a significant increase in yield for the two In case was obtained by increasing the number of time steps allowed during program execution. Owing to the low surface binding energy for In (and Ga), some low energy sputtered atoms were not counted in the early computer runs.

References

1. M.F. Dumke, PhD thesis, Caltech, 1982; M.F. Dumke et al., Surface Sci., 124, 407 (1983).
2. D.Y. Lo, M.H. Shapiro, T.A. Tombrello, Nucl. Inst. and Meth. B, submitted.
3. M.H. Shapiro, D.Y. Lo, P.K. Haff, T.A. Tombrello, Nucl. Inst. and Meth. B, in press; Caltech preprint BB-31 (1985).
4. M.H. Shapiro et al., Radiation Effects 89, 234 (1985).
5. M.H. Shapiro et at., Nucl. Inst. and Meth. B12, 137 (1985).
6. I.M. Torrens, Interatomic Potentials (Academic Press, New York, 1972).

# Chapter 5 - Collision Cascade in Liquid Indium

## 5.1 Introduction

Theoretical models of sputtering approach the sputtering process by breaking it down into three aspects:

1. Energy lost by the bombarding ion as it penetrates the target and the transferring of this energy to target atoms.
2. Development and nature of the collision cascade inside the target.
3. Final ejection of the sputtered atoms and their interaction with the target surface during the ejection process.

This chapter will be concerned with the development of the collision cascade and its relationship with the final spectra of sputtered atoms.

A major assumption in the Sigmund-Thompson analytic model of sputtering is that the collision cascade be fully randomized and isotropic during the time of ejection [1,2]. This assumption results in an expression for the differential sputtering yield that is decoupled in the variables representing the energy and ejection angle of the sputtered atoms (Eq. 1.18 of Chapter 1). Consequently, the shape of the energy spectrum is independent of ejection angles, and the shape of the angular spectrum is independent of ejection energies. Experiments capable of measuring energy and angular resolved neutral sputtering spectra (EARN) [3] have shown a shift of the energy spectrum to higher energies as the ejection angle becomes closer towards the normal and a broadening of the angular spectrum with lower ejection energies. Furthermore, the Sigmund-Thompson model predicts a universal $\cos\theta$ form for the angular spectrum. Deviations from this pure $\cos\theta$ form have been demonstrated repeatedly by MD simulations (Chapters 3, 4) and experiments [4,5].

Garrison made an *ad hoc* assumption of a cosine power momentum distribution for the collision cascade inside the target [6]. The reason behind introducing an anisotropic collision cascade is the spatial asymmetry that must exist because of the presence of a free surface. Target atoms near the surface will have a tendency to move in the direction of the outward surface normal. In the framework of the Thompson model, this assumption results in both a non-cosine angular distribution and a coupling of the angular and energy variables in a manner that agrees with experiments (Eq. 2 of App. 5.1). The objective of the present simulation is to determine the self-consistency of the Garrison model by correlating simulated collision cascade characteristics with the simulated, differential sputtering spectrum.

## 5.1 Summary

The collision cascade was monitored at several times during the sputtering simulation and was fitted by equations representing the cascade energy and angular distribution in the Garrison model (Eq. 5 of App. 5.1). Parameters resulting from the fit give a quantitative description of the cascade development (Tab. 2 of App. 5.1). The parameter **m** indicates the degree of spatial anisotropy, while **n** is related to the hardness of collisions between target atoms. Theoretically, **n** lies between 0 and 2, and increases with the hardness of collisions (Eq. 1.13 of Chapter 1). From the table we see that the angular anisotropy increases as the collision cascade develops and is finally carried away by the sputtered atoms. This process is also clear from plots of the cascade angular distribution (Fig. 3 of App. 5.1). The hardness of the collisions, on the other hand, increases monotonically with time. One explanation is that as the energy in the cascade dissipates, lower energy atoms see a harder region of the pair potential.

The simulated energy and angular resolved spectra (Fig. 1 and 2 of App. 5.1) agree with the predictions of Garrison's model [6] and EARN experiments [3]. The broadening of the angular spectra is less obvious in the simulated results because of low statistics (Fig. 2 of App. 5).

Consistency of Garrison's model is examined by obtaining the collision cascade parameters (**m** and **n**) from a fit of Garrison's expression for the differential sputtering yield (Eq. 2 of App. 5) to the simulated data. Simulated angle-integrated (over all angles) energy distribution and energy-integrated (over all energies) angular distribution were used for the fit. The integrated distributions were used to obtain better statistics. The fitting resulted in cascade parameters of **m** = 2.22 and **n** = 2.07. These values are larger than the values obtained directly from the simulated collision cascade (Tab. 2. of App. 5). This discrepancy indicates that the model is still not complete.

Some explanations are proposed for this inconsistency. One possibility is that the form assumed for the cascade distribution (Eq. 5 of App. 5) is not general enough. The expression assumes that the angle and energy variables are decoupled and that the deviation from isotropy is a simple cosine power law without an energy dependence. Another possibility is that the assumption of a planar surface potential is not valid. Additional ejection mechanisms may be contributing to the Jacobian transforming the collision cascade into the spectrum of sputtered atoms. Aside from these shortcomings, Garrison's model has enough free parameters and is capable of predicting trends in EARN sputtering data.

## Reference

1. P. Sigmund, Phys. Rev. **184**, 383 (1969).
2. M. W. Thompson, Phys. Rep. (Rev. Sec. of Phys. Let.) **69**, No. 4, 335 (1981).
3. J. P. Baxter, J. Singh, G. A. Schick, P. H. Kobrin, and N. Winograd, Nucl. Instr. and Meth. **B17**, 300 (1986).
4. Y. Qiu, J. E. Griffith, and T. A. Tombrello, Nucl. Instr. and Meth. **B1**, 118 (1984).
5. M. F. Dumke, T. A. Tombrello, R. A. Weller, R. M. Housley, and E. H. Cirlin, Surf. Sci. **124**, 407 (1983).
6. B. J. Garrison, Nucl. Instr. and Meth. **B17**, 305 (1986).

# SIMULATION STUDIES OF COLLISION CASCADES IN LIQUID In TARGETS[†]

D.Y. LO[1], M.H. SHAPIRO[2], T.A. TOMBRELLO[1], B.J. GARRISON[3] AND N. WINOGRAD[3]
[1]Division of Physics, Mathematics and Astronomy, Caltech, Pasadena, CA 91125, U.S.A.
[2]Physics Dept., California State University, Fullerton, CA 92634, U.S.A. and Division of Physics, Mathematics and Astronomy, Caltech, Pasadena, CA 91125, U.S.A.
[3]Chemistry Dept., Pennsylvania State University, University Park, PA 16802, U.S.A.

## ABSTRACT

Multiple interaction computer simulations have been used to determine the properties of collision cascades in liquid In targets induced by normally incident 5 keV $Ar^+$ ions. Below the first atomic layer the cascade becomes Thompson-like relatively quickly. However, within the first atomic layer the angular distribution of moving atoms became forward peaked by 150 fs and remained so until ~300 fs. Energy and angle resolved (EARN) spectra were calculated for the ejected atoms. The peak of the energy distribution shifted to lower energies at larger ejection angles, and the angular distributions became broader for lower energy particles. Both results agree with recent experimental data, and with a simple model proposed by Garrison. Our results suggest that the detailed structure of the surface layer is very important in the sputtering process.

## INTRODUCTION

In Thompson's model of sputtering [1] the distribution of ejected atoms is given by

$$\frac{d^2N(E,\theta)}{dE\,d\Omega} = \frac{AE\cos\theta}{(E+U)^{n+1}}. \tag{1}$$

where n depends on the atomic cross section and the nature of the collision cascade inside the target, U is the energy cost [2] to remove an atom from the surface, and A is a normalization constant. Deviations from the pure $\cos\theta$ dependence have been observed in previous experiments and simulations [3,4].

Mat Res Soc Symp Proc Vol 74 ©1987 Materials Research Society

Energy distributions are well described by (1) if U and n are considered free parameters, although U is close to the cohesive energy and n is near 2. The energy and polar angle dependencies are decoupled completely in (1). However, recent energy and angle resolved neutral atom (EARN) spectra of ejected atoms show a shift towards lower energy for the peak in the energy distribution as the polar angle becomes more grazing, and a broadening of the polar angle distribution with decreasing energy [5].

Garrison [6] has proposed a modified version of (1) to fit the EARN data, namely:

$$\frac{d^2N(E,\theta)}{dEd\Omega} = \frac{AE\cos\theta}{(E+U)^{m/2+n+1}}(U+E\cos^2\theta)^{m/2}. \qquad (2)$$

This formula with its additional free parameter m adequately predicts both the peak position shift in the energy distribution and polar angular distribution broadening. The parameters m and n depend on the nature of the collision cascade inside the target. (1) results from Thomson's assumption of an isotropic velocity distribution inside the target, while Garrison made the *ad hoc* assumption of a $\cos^m\theta$ velocity distribution within the target.

Our simulation studies are aimed at determining the nature of the velocity distribution within a liquid In target. However, on the time scale for the development of a collision cascade (a few hundred femtoseconds) the target can be considered an amorphous solid. Thus, our results should be comparable to those from polycrystalline targets.

The decoupling of angle and energy variables in (1) results from the assumption of an isotropic flux

$$\Phi_i(E_i,\theta_i)dE_id\Omega_i \propto \frac{1}{E_i^n}\frac{dE_id\Omega_i}{4\pi} \qquad (3)$$

inside the target. (The subscript i denotes variables inside the target.) To obtain the distribution of ejected atoms, the flux perpendicular to the surface is taken and subjected to the variable transformation $E_i \rightarrow E$ and $\theta_i \rightarrow \theta$ where E and $\theta$ are the energy and polar angle measured outside the range of a planar surface potential. Equation (1) then is obtained from

$$\frac{d^2N}{dEd\Omega} = \Phi_i(E_i,\theta_i)\cos\theta_i\frac{dE_i}{dE}\frac{d\Omega_i}{d\Omega}dEd\Omega, \qquad (4)$$

with $\Phi_i(E_i,\theta_i)$ as given by (3). Garrison assumed an anisotropic flux [6]

$$\Phi_i(E_i,\theta_i)dE_i d\Omega_i \propto \frac{\cos^m\theta_i}{E_i^n} dE_i d\Omega_i. \qquad (5)$$

Since $E_i$ and $\theta_i$ are still decoupled equation (2) can be obtained from (4).

The energy distribution integrated over the hemisphere then is

$$\frac{dN(E)}{dE} = \frac{\pi A}{b}\,\frac{1}{(E+U)^a}((U+E)^b - U^b), \qquad (6)$$

where $a = (m/2)+n+1$ and $b = (m/2)+1$. This energy distribution has a single peak at $E_p = U((a/n)^{1/b} - 1)$. Careful examination of (2) reveals that while the peak position in the energy distribution for a particular angle depends on n and is proportional to E, the separation between energy peak positions for different angles depends strongly on m. Peak positions generally decrease with n and their separations generally increase with m.

## SIMULATION MODEL

The multiple interaction (MI) code SPUT1 [7] was used for this study. Liquid targets consisting of 603 In atoms melted from a fcc structure and heated to a temperature of ~900 K [8] were bombarded with normally incident 5 keV Ar ions. Different liquid targets were generated by modeling the In target without the ion beam present. Atom velocities and positions were stored every picosecond, and the resulting target was used for 25 ion impacts at different locations. Each target was restored to its initial state before each impact in order to simulate the experimental conditions in [5] where the dose was very low. A total of 1000 impacts on 40 different targets were computed on the California State University Cyber-760 computer system.

Pair-wise additive potentials were assumed in the study. The atom-atom potential consisted of a Moliere core joined to a Morse well with a cubic spline. The ion-atom potential was a simple Moliere. Potential parameters were obtained by standard procedures [9-11]. The form of the potentials and the associated parameters are given in Table 1.

Table 1
Potential Parameters

| | |
|---|---|
| Ion-atom | |
| $V_{ij} = (A/r)[0.35e^{-0.3r/B} + 0.55e^{-1.2r/B} + 0.1e^{-6r/B}]$ | $r < r_a$ |
| $V_{ij} = 0$ | $r \geq r_a$ |
| $A = 12701.\ \mathrm{eV\,Å}$ $B = 0.09335\ \mathrm{Å}$ $r_a = 2.868\ \mathrm{Å}$ | |
| Atom-atom | |
| $V_{ij} = (A/r)[0.35e^{-0.3r/B} + 0.55e^{-1.2r/B} + 0.1e^{-6r/B}]$ | $r < r_a$ |
| $V_{ij} = C_0 + C_1 r + C_2 r^2 + C_3 r^3$ | $r_a \leq r < r_b$ |
| $V_{ij} = D_e[e^{-2b(r-r_e)} - 2e^{-b(r-r_e)}]$ | $r_b \leq r < r_c$ |
| $V_{ij} = 0$ | $r \geq r_c$ |
| $A = 34574.\ \mathrm{eV\,Å}$ $B = 0.08065\ \mathrm{Å}$ $C_0 = 89.151\ \mathrm{eV}$ $C_1 = -23.619\ \mathrm{eV/Å}$ $C_2 = -33.167\ \mathrm{eV/Å^2}$ $C_3 = 11.797\ \mathrm{eV/Å^3}$ $D_e = 0.343\ \mathrm{eV}$ $b = 1.014\ \mathrm{Å^{-1}}$ $r_e = 3.447\ \mathrm{Å}$ $r_a = 1.88\ \mathrm{Å}$ $r_b = 2.04\ \mathrm{Å}$ $r_c = 4.71\ \mathrm{Å}$ | |

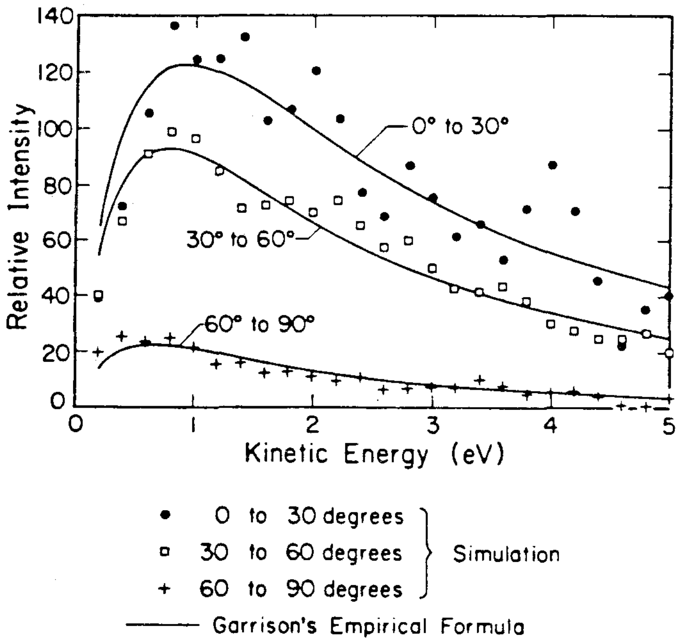

Fig. 1 Angle Resolved Energy Spectra

## RESULTS

Energy and polar angular distributions of ejected atoms were angle and energy resolved, respectively. Energy distributions were obtained for angular intervals of 0° to 30°, 30° to 60°, and 60° to 90°. Polar angular distributions were obtained for energy intervals of 0 to 2 eV, 2 to 4 eV, and 4 to 6 eV (figs. 1 and 2). The peak positions of the energy distributions clearly exhibit a shift toward higher energies with decreasing polar angles, while the polar angular distributions broaden with lower energies. These trends basically agree with the experimental EARN data [5] and the predictions of Garrison [6]. The distributions predicted by (2) with m = 2.22, n = 2.07, and U = 1.98 eV are shown in figs. 1 and 2 for comparison. The parameters m, n, and U were obtained by fitting the simulated angle-integrated energy distributions to (6). This resulted in a simulated angle-integrated energy distribution peak at 0.8 eV in comparison to the experimentally observed value of ~2 eV [5].

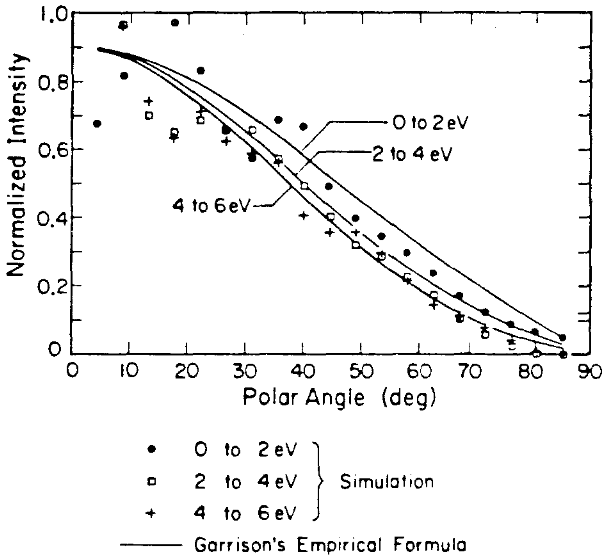

Fig. 2 Energy Resolved Angular Distributions

The energy and polar angular distributions of atoms with kinetic energy > 1 eV in the first and second surface layers of the target were sampled at various times throughout the collision cascade. The 1 eV cut-off excluded most of the atoms outside the collision cascade. The first layer distributions were fitted to the anisotropic flux of (3) which was assumed by Garrison. Since $d^2N_i/dE_i d\Omega_i = (2mE_i)^{-1/2} \Phi_i(E_i,\theta_i)$, $dN_i/dE_i$ was fitted to $A/E^{n+1/2}$ while $dN_i/d\Omega_i$ was fitted to $B\cos^m\theta + C$ where A, B, and C are constants. The finite bin size of the simulated distributions was accounted for by integrating the analytical expressions over each bin before fitting. All fitting was done by minimizing $\chi^2$ assuming that the uncertainty in the simulated distributions was governed by a Poisson distribution. The resulting values of m and n are tabulated in Table 2. The small values of $\chi^2_\upsilon$ are an indication that Poisson statistics overestimates the uncertainties in the simulated spectra.

Table 2
First Layer Flux Distribution Parameters

| Time (fs) | m | $\chi^2_\upsilon$ | n | $\chi^2_\upsilon$ |
|---|---|---|---|---|
| 100 | 0.52 (.25)* | 0.38 | 0.67 (.17)* | 0.47 |
| 150 | 1.4 (.65) | 0.38 | 0.75 (.10) | 0.42 |
| 200 | 1.1 (.27) | 0.30 | 1.0 (.10) | 2.2 |
| 250 | 1.5 (.42) | 0.65 | 1.4 (.10) | 3.8 |
| 300 | 1.1 (.35) | 0.63 | 1.8 (.12) | 2.3 |
| 400 | 0.46 (.22) | 0.56 | 2.4 (.21) | 1.8 |

*The quantities in parenthesis are the expected statistical uncertainties assuming a Poisson distribution.

The first layer angular distribution shows a definite forward peak by 150 fs and becomes nearly isotropic by 400 fs (Table 2 and fig. 3). The greatest anisotropy occurs at ~250 fs. This should be the most important distribution since all sputtered atoms must traverse the first layer, and most atoms are ejected near this time in the cascade development. The second layer angular distribution is isotropic from 100 to 300 fs, then becomes transversely peaked by 400 fs. This may be an artifact of the finite size and slab-like geometry of the target. The energy distribution parameter n increases monotonically with time and has roughly the same value for the first and second atomic layers. This reflects the steady degradation in average energy of the atoms as the collision cascade ages.

## DISCUSSION

Our results show that the presence of a free surface (neglected in the Thompson model) causes significant anisotropy in the first layer flux. This

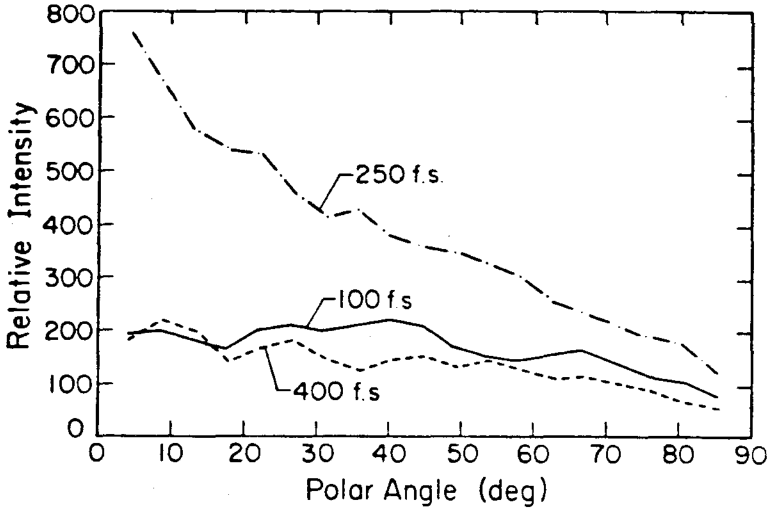

Fig. 3 Time Development of First Layer Angular Distributions

anisotropy diminishes quickly in the subsurface layers. The strong anisotropy in the surface layer portion of the collision cascade occurs at the time when the greatest number of atoms are ejecting. This has significant effects on the sputtered atom distributions. These effects have been seen both in recent experiments and the present simulations.

It is clear from our simulation that both the peak position shift in the energy distribution and the broadening of the angular distributions can be explained using pairwise interactions of the target atoms. However, the large discrepency between the energy peak position in the simulated spectra (0.8 eV), and the experimental value (~2 eV) may reflect some inadequacy in the pair potential model. Studies which include many body effects through the use of an effective medium model are now underway [12].

*Supported in part by the U.S. National Science Foundation [DMR83-06541(Caltech) and DMR83-06548 (CSUF)].

References

1. M.W. Thompson, Phys. Rept. 69, 337 (1981).
2. B.J. Garrison, N. Winograd, D.Y. Lo, T.A. Tombrello, M.H. Shapiro, and D.E. Harrison Jr., Surf. Sci. (1986) in press.
3. M.F. Dumke et al., Surf. Sci. 124, 407 (1983)
4. M.H. Shapiro, D.Y. Lo, P.K. Haff and T.A. Tombrello, NIM B13, 348 (1986).

5. J.P. Baxter, J. Singh, G.A. Schick, P.H. Kobrin, and N. Winograd, NIM B17, 300 (1986).
6. B.J. Garrison, NIM B17, 305 (1986).
7. M.H. Shapiro, Technical Rept. BB-1 Caltech (1983).
8. D.Y. Lo, T.A. Tombrello and M.H. Shapiro, NIM B17, 207 (1986)
9. I.M. Torrens, Interatomic Potentials. (Academic Press, New York, 1972).
10. L.A. Girifalco and V.G. Weizer, Phys. Rev. 114, 687 (1959).
11. C. Kittel, Introduction to Solid State Physics, 5th ed. (Wiley, N.Y., 1976).
12. B.J. Garrison, N. Winograd, D.Y. Lo, T.A. Tombrello, M.H. Shapiro, and D.E. Harrison, Jr., in preparation.

# Chapter 6 - Preferential Sputtering From Isotopic Mixtures

## 6.1 Introduction

Isotopes of a single element target will, in general, be sputtered with different degrees of preference. This phenomenon is interesting for several reasons. Preferential sputtering of isotopes is the simplest example of preferential sputtering of multicomponent systems. It allows the effects of mass difference to be separated from effects that are due to atomic numbers. Studying this phenomenon may also yield information on interatomic forces and sputtering mechanisms because their effects are amplified in the degree of preference for sputtering of one isotope over another. As a practical aspect, this phenomenon is important in the interpretation of SIMS data. Furthermore, it also may be partly responsible for anomalous isotopic compositions in extraterrestrial materials that have been subjected to ion irradiation in space.

The difference in preference for the sputtering of one isotope over another is best quantified by the isotopic fractionation **F**:

$$\mathbf{F}_{ij} = \left( \frac{C_j}{C_i} \frac{Y_i}{Y_j} - 1 \right). \qquad (6.1)$$

Here, $C_i$ is the target concentration and $Y_i$ the sputtering yield of the **i**-th isotope. The **i**-th isotope is, by convention, chosen to be the lighter mass so that an enhancement of the lighter isotope relative to target concentration will give a positive fractionation. Theory [1], simulations [2-4], and experiments [5-7] have all established this quantity to be at most a few percent, with an enrichment of the lighter isotope in all cases, and is independent of the isotopic composition. However, computer simulations have shown an ejection angle dependence by the fractionation effect [2-4], while theory predicts an isotopic fractionation independent of the ejection angle. Furthermore, the theory fails to account for ion mass effects that are present in simulation results [3,4].

Sigmund's random emission model of isotopic fractionation predicts an isotopic fractionation that is dependent only upon the relative mass of the isotopes and an adjustable parameter reflecting the hardness of the assumed binary atom-atom collisions [1]:

$$F_{ij} = \left(\frac{M_j}{M_i}\right)^{2m} - 1 \tag{6.2}$$

Here $M_i$ is the mass of the **i**-th isotope and **m** is a parameter in the power-law approximation to the atom-atom pair potential.

Furthermore this expression is isotropic in space. Major assumptions and consequences of this model are:

1. Collision cascades are fully isotropic, leading to isotopic fractionations that are independent of direction.
2. Memory of the incident ion is lost in a fully randomized cascade, leading to isotopic fractionations that are independent of the bombarding ion.
3. Isotopic fractionation is linear in mass difference at small mass differences with a slope that increases with decreasing hardness of the atomic collisions.

The objectives of this molecular dynamics study are:

1. Investigate the dependence of isotopic fractionation on mass difference for 3 component isotopic mixtures.
2. Determine isotopic fractionation for forwardly sputtered atoms (transmission sputtering), hence dependence of fractionation on ion direction relative to surface of ejection. Also investigate ion mass effect.
3. Examine the ejection angle dependence of isotopic fractionation and anisotropy of the collision cascade.
4. Simulate isotopic fractionation from liquid targets and compare with single crystal results.
5. Compare simulation with the Sigmund model.

## 6.2 Summary

Results of the simulated isotopic fractionation are summarized in Tab. 1 of App. 6. To test the consistency of Sigmund's model, the parameter **m** in Eq. 6.2 must first be obtained from the simulation model. The parameter **m** is related to the interatomic pair potential through the power-law approximation:

$$\phi(\mathrm{R}) \propto \frac{1}{\mathrm{R}^{m}}. \tag{6.3}$$

Here, $\phi$ is the pair potential and R is the interatomic separation. Since our atom-atom interaction includes an attractive part, it is not sufficient to fit the vacuum pair potential $\phi(\mathbf{R})$. Instead, we replace $\phi(\mathbf{R})$ by a displacement energy $\mathbf{E}_d(\mathbf{R})$ in Eq. 6.3. Here, $\mathbf{E}_d(\mathbf{R})$ is the energy of an atom as it moves toward a nearest neighbor in an fcc lattice. A value of $m = .19$ is obtained by fitting to $\mathbf{E}_d$ over the 0 to the 100 eV range where we think is relevant to sputtering (fig. 6-1).

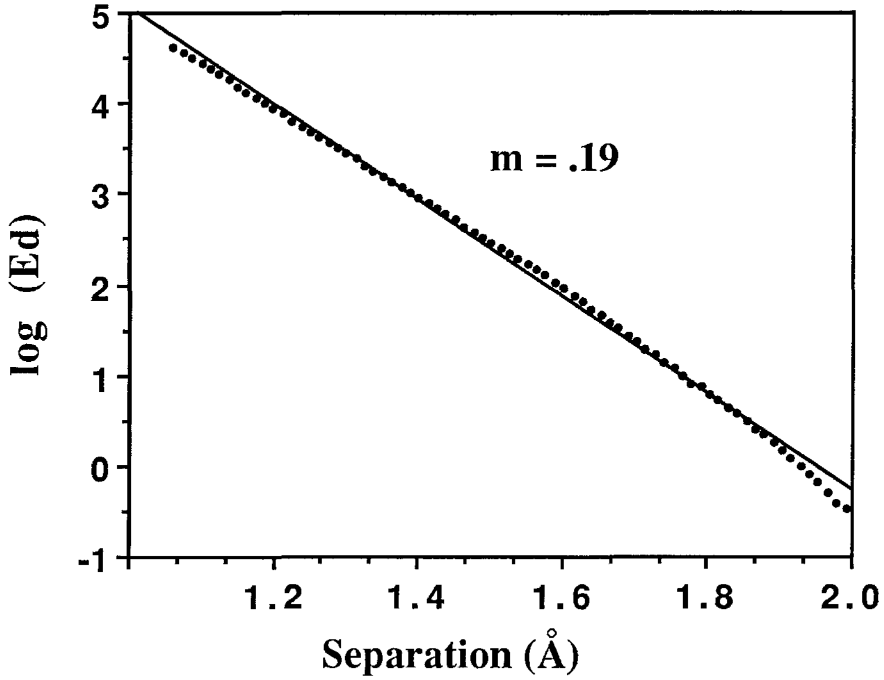

Figure 6-1: Power law fit to displacement energy.

Using this value of m, a comparison to the Sigmund models is made in Table 6.

For the 3-isotope systems, the simulated isotopic fractionations have a linear dependence on the mass difference within uncertainties. This is most apparent for the 3-isotope liquid target as shown in Figure 6-2.

Table 6: Comparison of simulated isotopic fractionations to theory.

| Target Description | | Mass (%) | Fractionation (mils) | |
|---|---|---|---|---|
| /Dimensions | Ion | Difference | Simulation* | Theory** |
| 3-isotope crystal<br>15x4x15 | $Ar^+$ | 10 | 27 ± 14 (12 ± 11) | 37 (19) |
| 3-isotope crystal<br>15x4x15 | $Ar^+$ | 11 | 21 ± 12 (31 ± 10) | 40(20) |
| 3-isotope crystal<br>15x4x15 | $Ar^+$ | 22 | 48 ± 15 (43 ± 11) | 78(39) |
| 2-isotope crystal<br>15x6x15 | $Ar^+$ | 25 | 67 ± 18 (36 ± 14) | 88(44) |
| 2 isotope liquid<br>14x6x14 | $Ar^+$ | 25 | 127 ± 22 (53 ± 21) | 88(44) |
| 2 isotope liquid<br>14x6x14 | $HAr^+$ | 25 | 71 ± 15 (50 ± 17) | 88(44) |
| 3-isotope liquid<br>14x6x14 | $Ar^+$ | 11 | 25 ± 22 (27 ± 13) | 40(20) |
| 3-isotope liquid<br>14x6x14 | $Ar^+$ | 17 | 78 ± 23 (78 ± 19) | 61(31) |
| 3-isotope liquid<br>14x6x14 | $Ar^+$ | 30 | 106 ± 28 (107 ± 17) | 105(51) |

* Values in parentheses are for forward sputtering.

** Values in parentheses are for the surface emission model.

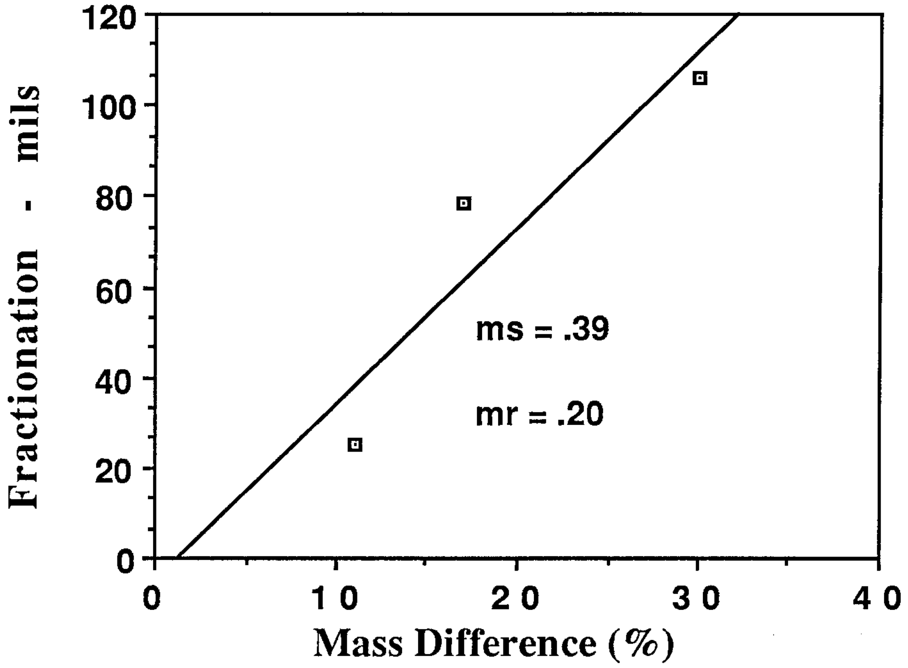

Figure 6-2: Linear fit of isotopic fractionation as a function of mass difference for the 3-isotope liquid target.

The simulated isotopic fractionation for the crystal targets have an ejection angle dependence with a greater enhancement of the lighter isotopes in the direction normal to the ejection surface (Tab. 1 and Fig. 1 of App. 6). Directional anisotropy is also observed in the collision cascade (Fig. 2 of App. 6).

As a summary, the following observations are made from this molecular dynamics study:

1. Collision cascades are highly anisotropic.

2. A larger enhancement of the lighter isotope in the backward sputs for the two-isotope targets.

3. Isotopic fractionation is angular dependent.

4. Anisotropy aspects of fractionation are different in liquid and crystal targets.

5. Isotopic fractionation depends on the ion mass.

6. Overall fractionation has a linear mass dependence and is consistent with the interatomic potential used here within the Sigmund framework.

## Reference

1. P. Sigmund, Nucl. Instr. and Meth. **B18**, 375 (1987).
2. W. Eckstein and J. P. Biersack, Appl. Phys. **A37**, 95 (1985).
3. M. H. Shapiro, P. K. Haff, T. A. Tombrello, and D. E. Harrison, Jr., Nucl. Instr. and Meth. **B12**, 137 (1985).
4. M. H. Shapiro, T. A. Tombrello, and D. E. Harrison, Jr., Nucl. Instr. and Meth. **B30**, 152 (1988).
5. L. M. Baumel, M. R. Weller, R. A. Weller, and T. A. Tombrello, Nucl. Instr. and Meth. **B34**, 427 (1988).
6. H. Gnaser and I. D. Hucheon, Phys. Rev. **B 35**, 877 (1987).
7. J. M. Fluit, L. Friedman, A. J. H. Boerboom and J. Kistemaker, J. Chem. Phys. **35**, 1143 (1961).

# Molecular Dynamics Simulation of Preferential Sputtering from Isotopic Mixtures*ζ.

Davy Y. Lo and T. A. Tombrello, Department of Physics, 200-36, California Institute of Technology, Pasadena, CA 91125, USA.
M. H. Shapiro, Department of Physics, California State University, Fullerton, CA 92634, USA

## Abstract

The non-stoichiometric sputtering of different isotopes from elemental targets containing two and three isotopes is simulated with molecular dynamics. Cu targets consisting of isotopes with artificially high mass differences ranging from 10% to 30% are bombarded with normally incident 5 keV $Ar^+$ ions. Liquid and single crystal targets are studied. Both backward and forward sputtering spectra are examined. Overall enrichments of the lighter isotopes in the sputtered material are observed in all cases with a consistent lower enrichment in the material sputtered forward for the liquid targets. Simulation results show a linear dependence of the isotopic fractionation (fractional change of the isotopic ratio in the sputtered atoms from stoichiometric value) on the mass difference in the three-isotope system within statistical uncertainties. A clear dependence of the isotopic fractionation on angle of emission with a larger enhancement of the lighter isotope in materials ejected toward the surface normal is observed for the crystal targets but not for liquids. For the liquid targets, a larger isotopic fractionation in the backward sputtering yield is seen. An ion mass dependence is also noted with a higher fractionation effect for the lighter ion.

* Supported in part by the U.S. National Science Foundation (DMR86-15641).

ζ To appear in Nuclear Instruments and Methods B, 1989.

Davy Y. Lo

## Introduction

At present the state of our understanding of isotopic fractionation accompanying sputtering is at best incomplete. We are still in need of a theoretical, computational, and experimental convergence. This is due in part to a lack of experimental data in the low ion fluence regime. Both theory and simulation focus on zero fluence limits because of simplicity; however, this regime is experimentally difficult to explore.

The theory under scrutiny is that of Sigmund [1], in which approximate analytic expressions based on linear cascade theory were derived for the zero fluence limit. Up to first order in the mass difference, the linear transport equations predict recoil cascade densities for each mass type to be decoupled from the mass of the initiating atom or ion. At this point any angular dependence in the collision cascade is ruled out even before explicitly assuming cascade isotropy. This also leads to isotopic fractionations that are independent of the bombarding ion. Previous molecular dynamics simulations by Shapiro have contested both claims [2,3]. In these simulations with two-isotope pseudo Cu crystal targets, an enrichment of the lighter isotope in the surface normal direction was clearly observed. Dependence on ion mass and energy was also shown. A further point of the Sigmund-Shapiro divergence lies in the overall observed isotopic fractionation, with the simulation predicting a much higher lighter isotope enrichment. Experimentally both ejection angle and incident ion dependence have been observed [4,5]. Recent observations with low ion fluence steps and subsequent extrapolation to zero fluence have shown a much higher isotopic fractionation than that predicted by Sigmund's theory (with any reasonable theory parameter) [6]. The zero fluence extrapolation of experimental data showed a ion-target relative mass dependence consistent with Shapiro's simulations. However, zero fluence angular data is still lacking, and as of this writing experiments are being performed in our group to determine the angular dependence of isotopic fractionation near zero fluence.

Davy Y. Lo

The present simulation will focus on several ideal systems that has no realistic experimental counterpart but may be compared directly with analytic theories. It is hoped that results from such a simulation can be extrapolated to understand or predict trends in experimental results and provide insight to the theorists. The isotopes used here are pseudo-Cu with mass differences three to eight times that of natural Cu. Both backward sputs and forward sputs (atoms ejecting from the ion's entrance and exit side, respectively) are examined. A three-isotope crystal is studied to determine the sensitivity of isotopic fractionation to the presence of a third isotope. Liquid targets are also studied to ascertain effects of random bulk and surface structure. Conceptually, isotopic sputtering experiments on liquid targets may prove interesting. Although depletion of one isotope component at the surface will not be immediately replenished as in the case of a Gibbsian segregated surface, thermal diffusion could serve to sustain a bulk isotopic concentration at the surface and facilitate zero fluence comparisons to theory or simulation.

## Molecular Dynamics Model

The state of the system is evolved by integrating Newton's equations of motion. All particle interactions are tracked at each time step. The code is based on Sputl [7] with a more stringent predictor-corrector pair and equipped to handle periodic boundary conditions.

The interaction used here is a pair potential approximation identical to that used in the previous isotopic sputtering simulations by Shapiro [2]. The atom-atom interactions consist of a Born-Mayer core splined to an attractive Morse potential, while the ion-atom interacts only through a repulsive Born-Mayer core.

The crystal target used in the three-isotope case is 15x4x15 (ie. a 15 by 15 layer square slab that is 4 layers thick) fcc single crystal. For the liquid runs, liquid slabs melted from a 14x6x14 fcc crystal are used. Atomic masses are assigned to each atom in a random fashion to model the isotopic mixture. For each isotope, a fixed number (corresponding to the desired concentration of that isotope) of atoms are chosen at random and assigned the isotopic mass. Selections of atoms for each isotope are done successively without replacement. Thus in a target of **N** atoms with **m** isotopes and $C_i$ atoms of the i-th isotopic species, a total of $N - C_m$ random numbers are used to assign masses to the whole target. Masses are reassigned before *every* impact. This assures a *constant* target stoichiometry. For the liquid runs, isotopic types are also permuted for each target configuration and impact parameter. This will insure unbiased sampling of local isotopic concentration fluctuations. The addition of this step appears to damp out fluctuations in the relative isotopic yields.

Melting of the Cu crystal structure is accomplished by assigning a Gaussian velocity distribution with a temperature high enough to melt the target [8]. The liquid targets are evolved under semi-periodic boundary conditions periodic in the (010) plane. The two surfaces normal to the beam direction have free boundaries. The semi-periodic boundary conditions are removed during the sputtering runs. The masses used during target evolution is that of real Cu (63.546 amu). A liquid state is determined by examining the atomic sites for long range order. This done both by visual inspection of the real lattice space and pair correlation functions. Typically it takes less than ten picoseconds after the initial temperature application before long range order disappears and a few tens of picoseconds after initial melting to obtain temperature equilibrium. The final equilibrium temperature is approximately 1600 K.

Ion impact parameters for the crystal runs are chosen to reflect the underlying symmetry in a way identical to previous simulations [2]. Each impact begins with a virgin target. For the liquid targets, 25 impact points are chosen to cover uniformly the 14x14 (25 Å x 25 Å) surface. At this density, impact point separations are well outside the ion-atom interaction cut-off of 1.5 Å. Each impact is exactly centered about the target by re-sectioning the target in accordance with the periodic boundary conditions under which it was evolved. After each set of 25 impact parameters the target is evolved for one picosecond to obtain a fresh target. At a simulated diffusion coefficient of 4.0 x $10^5$ $cm^2/s$, this is long enough to insure randomization of the atom positions relative to ion impact points.

For the three-isotope case, masses .9, 1.0, and 1.1 in units of Cu mass (63.546 amu) are assigned in equal abundance to the crystal atoms. This corresponds to pair mass differences (relative to the lighter mass) of 10%, 11%, and 22%. For the three-isotope liquid targets, masses of .9, 1.0, and 1.17 Cu mass were used again in equal abundance. Masses of .8 and 1.0 Cu mass in equal abundance were used in the two-isotope targets. Both theory, simulation, and experiments show that isotopic fractionation is insensitive to the target stoichiometry. Since the yields of each isotope are approximately the same (fractionation is a percentage effect), choosing an equal abundance for each isotope will optimize that statistics. All runs consist of $10^3$ impacts except in the three-isotope case where $1.2 \times 10^4$ impacts are used.

The bombarding ion is a 5 keV $Ar^+$ (39.948 amu) in all cases except for the heavy ion run with the liquid target where its mass is increased to 80.867 amu. This mass is chosen to reverse the ion-atom energy transfer bias from a light to a heavy isotope preference. The heavy $Ar^+$ will hereafter be designated as $HAr^+$.

## Overall Fractionation

Isotopic fractionation of one isotope relative to another is defined as:

$$(1) \qquad F_{ij} = \left(\frac{C_j}{C_i}\,\frac{Y_i}{Y_j} \quad - \quad 1\right)$$

Here $C_i$ is the target concentration and $Y_i$ the sputtering yield of the i-th isotope. The i-th isotope is, by convention, chosen to be the lighter mass so an enhancement of the lighter isotope relative to target concentration will give a positive fractionation. Fractionation results are summarized in table 1. Here we see an overall enrichment of the lighter species in all cases.

For the three-isotope target, fractionation is seen to depend linearly on the mass difference within statistical uncertainties (table 1). The fractionation in the backward sputs for the three-isotope crystal target is consistently lower by more than a factor of two compared to previous simulations with a two-isotope crystal [2]. This large discrepancy has been traced to the target lateral dimensions. The previous results were obtained from 14x4x14 fcc crystals. By increasing the lateral dimension to 15x15, the overall fractionation for a mass difference of 25% in a two-isotope system, is lower and agrees with the three-isotope result within uncertainties. Further increase of target dimensions to 16x4x16 and 15x6x15 showed no appreciable change in overall fractionation.

The two-isotope liquid runs show a consistently larger fractionation in the backward sputs as compared to the forward sputs in both the $Ar^+$ and $HAr^+$ bombardment. For $HAr^+$ bombardment, the fractionation in the backward sputs is lower by more than 40% compared with $Ar^+$ bombardment while the fractionation in the forward sputs showed no change. The backward sput fractionation agrees with previous simulation with crystal targets of similar lateral dimensions [2].

## Ejection Angle Dependence

Dependence of the isotopic fractionation on the polar angle of ejection is examined. The ejection angle is measured relative to the zenith of each ejection surface (backward and forward). The ejection angle range (0° to 90°) is partitioned into two bins. The partitioning angle is chosen about the median of the ejection angle spectra. Table 1 shows fractionation results of each run for partitioning angles of 30, 40, and 50 degrees. For partitioning angles close to the median, the uncertainties should be approximately $\sqrt{2}$ larger than the uncertainties for the total fractionation listed in Table 1.

Results show clearly a non-isotropic isotope effect for all the crystal target runs, with an enrichment of the lighter species in the zenith angles of ejection relative to the oblique directions for both the forward and backward sputs.

The liquid targets behave quite differently from the crystals and the results are sensitive to the bombarding ion mass. In the $Ar^+$ case, fractionation in the forward sputs is isotropic while the light isotope enrichment is enhanced in the oblique directions for the backward sputs. For the $HAr^+$ bombardment, a trend towards the converse is observed. The light isotope is enriched isotropically in the forward sputs while the backward sputs show an enhanced enrichment in the oblique angles of ejection.

The angular dependent fractionation effects can be seen directly in the angular spectra of sputtered atoms. The ejection angle spectra for the 22% mass difference isotope pair in the three-isotope run is compared with that for the two-isotope case in the $HAr^+$ on liquid Cu run (Figure 1).

## Discussion

Sigmund's random emission model of isotopic fractionation predicts an isotopic fractionation that is dependent only upon the relative mass of the isotopes and a adjustable parameter reflecting the hardness of the assumed binary atom-atom collisions [1]:

$$F_{ij} = \left(\frac{M_j}{M_i}\right)^{2m} - 1 \tag{2}$$

Here $M_i$ is the mass of the i-th isotope and m is a parameter in the power-law approximation to the atom-atom pair potential. Furthermore this expression is isotropic in space. One immediately notices that isotopic fractionation should vanish for hard spheres of the same radius. Intuitively, enrichment of the lighter species is possible even for sputtering of hard spheres since it will take fewer collisions for the lighter mass to reflect back towards the surface.

The value of $m$ that is appropriate for the potential used in the present simulation has been estimated in order to make a comparison with the expression above. Since our atom-atom interaction includes an attractive part, it is not sufficient to fit the vacuum pair potential to the power law $\phi(r) \propto r^{-1/m}$. Instead we fit the displacement energy of an atom as it is moved toward a nearest neighbor in a fcc lattice over the 0 to 100 eV range where we think is relevant to sputtering. A value of $m = .19$ is obtained. At this value, (2) predicts fractionations of .037, .040, .078, .088 for mass differences of 10%, 11%, 22%, and 25% respectively. Comparing to the simulated overall fractionation of the 15x15 (lateral dimensions) targets, these values lie outside of the uncertainties for four out of the seven cases (table 1). Sigmund's alternate surface emission model would involve replacing $m$ in (2) by $m/2$. The predicted fractionations are roughly one half of the random emission model and are within uncertainties of the simulated values in six out of the seven cases. Caveats as to this agreement with the surface emission model prediction must be given. First the fractionation is extremely sensitive to the potential parameter $m$. Extraction of $m$ from a non-power law potential is a rough estimate at best. A complete comparison with Sigmund's theory also requires comparing other predictions of the model (eg. differential sputtering yield) since $m$ is a universal model parameter.

The systematic correlation with the ion mass and beam direction is completely outside the prediction of Sigmund's theory. We note the clear dependence of isotopic fractionation on the angle of ejection. Furthermore this dependence is seen here to be coupled to the beam's direction relative to the ejection surface and the relative masses of the incident ion and target atoms. Both points to the invalidity of the fully randomized cascade assumption in *linear cascade theory*[9]. To investigate further target memory of the ion, we have time averaged the particle flux distributions inside the collision cascade for the liquid target runs. Time averages of the flux angular distribution taken over the first and second hundred femtoseconds of each impact for the $Ar^+$ bombardment case are shown in figure 2. We note that the asymmetric isotopic fractionation in the backward and forward sputs is reflected in the early flux and not in the late flux. The early flux is asymmetric in the forward and backward directions due to overall momentum conservation. After the first hundred femtoseconds, the net momentum imparted by the ion has been carried away by the forward sputs. Hence, the late flux is symmetric along the beam direction. The angular dependence of the particle flux clearly demonstrates the momentum anisotropy inside the cascade.

## Conclusion

In these simulations, strong angular anisotropy effects are observed both in the collision cascade and isotopic fractionation of the sputtered material. The angular anisotropy is exhibited by the flux of each isotope and their ratios. Isotopic fractionation dependences on the beam direction and ion mass clearly indicate that the random cascade assumption is inadequate. The early cascade flux is shown to be more relevant to the subsequent enhanced isotopic fractionation in the backward sputs. In these respects, the present simulation is in disagreement with Sigmund's theory of isotopic fractionation.

The overall isotopic fractionation prediction of Sigmund's surface emission model is within the uncertainties of the present simulation. The linear dependence on the mass difference in (2) is not violated in our simulation of a three-isotope system within statistical uncertainties.

The discrepancies between the overall fractionation in targets of different dimensions warrants further investigation. The large difference in the anisotropy effects between the liquid and crystal targets suggest further subtleties in the isotopic mass effect. Simulations that focus on a particular fractionation mechanism are needed to gain further understanding of the phenomena.

## Acknowledgements

We wish to thank the NSF for providing computation time on the Cray-XMP at the San Diego Supercomputer Center. Many thanks also goes to the physics department of California State University at Fullerton for free access to their computing facilities. Helpful suggestions through enjoyable conversations with Steve Spicklemire, Don E. Harrison, Jr., and Peter Sigmund are acknowledged.

The writing of this paper coincides with the passing of Don E. Harrison, Jr. who has given invaluable guidance to the works of this group. Don will be deeply missed by everyone.

Davy Y. Lo

**Reference**

1. P. Sigmund, Nucl. Instr. and Meth. **B18** (1987) 375.

2. M. H. Shapiro, P. K. Haff, T. A. Tombrello, and D. E. Harrison, Jr., Nucl. Instr. and Meth. **B12** (1985) 137.

3. M. H. Shapiro, T. A. Tombrello, and D. E. Harrison, Jr., Nucl. Instr. and Meth. **B30** (1988) 152.

4. W. A. Russel, D. A. Papanastassiou, and T. A. Tombrello, Radiat. Eff. **52** (1980) 41.

5. L. M. Baumel, M. R. Weller, R. A. Weller, and T. A. Tombrello, Nucl. Instr. and Meth. **B34** (1988) 427.

6. H. Gnaser and I. D. Hucheon, Phys. Rev. B 35 (1987) 877.

7. M. H. Shapiro, Technical Report **BB-1**, Caltech (1983).

8. D. Y. Lo, T. A. Tombrello, and M. H. Shapiro, Nucl. Instr. and Meth. **B17** (1986) 107.

9. P. Sigmund, Phys. Rev. **184**, (1969) 383.

**Table 1 - Isotopic Fractionation**

The sputtered atoms are partitioned into two angular bins corresponding to ejection angles θ greater than or less than the partitioning angle ψ. Fractionation in the two angular bins and for all angles are tabulated for both the backward and forward sputtering yields, with the forward case in parenthesis.

| Target Description /Dimensions | Ion | Mass (%) Difference | ψ (degrees) | Fractionation (‰) $\theta < \psi$ | $\theta > \psi$ | Fractionation(‰) Total |
|---|---|---|---|---|---|---|
| 3-isotope crystal<br>15x4x15 | $Ar^+$ | 10 | 30 | 67 (49) | 7.8 (-13) | 27 ± 14 (12 ± 11) |
| | | | 40 | 52 (25) | -13 (-18) | |
| | | | 50 | 38 (12) | -18 (-2.8) | |
| 3-isotope crystal<br>15x4x15 | $Ar^+$ | 11 | 30 | 78 (80) | -24 (-1.4) | 21 ± 12 (31 ± 10) |
| | | | 40 | 37 (49) | -26 (-6.5) | |
| | | | 50 | 17 (34) | 37 (8.3) | |
| 3-isotope crystal<br>15x4x15 | $Ar^+$ | 22 | 30 | 152 (133) | -16 (-14) | 48 ± 15 (43 ± 11) |
| | | | 40 | 90 (75) | -39 (-24) | |
| | | | 50 | 55 (46) | 18 (5.5) | |
| 2-isotope crystal<br>15x6x15 | $Ar^+$ | 25 | 30 | 112 (55) | 29 (22) | 67 ± 18 (36 ± 14) |
| | | | 40 | 105 (68) | -58 (-50) | |
| | | | 50 | 76 (52) | -119(-140) | |

**Table 1 - continued**

| Target Description /Dimensions | Ion | Mass (%) Difference | ψ (degrees) | Fractionation (‰) θ < ψ | Fractionation (‰) θ > ψ | Fractionation(‰) Total |
|---|---|---|---|---|---|---|
| 3-isotope liquid 14x6x14 | Ar⁺ | 11 | 30 | -21 (39) | 72 (13) | 25 ± 22 (27 ± 13) |
| | | | 40 | -14 (30) | 130 (15) | |
| | | | 50 | 6 (31) | 156 (-10) | |
| 3-isotope liquid 14x6x14 | Ar⁺ | 17 | 30 | 70 (60) | 89 (98) | 78 ± 23 (78 ± 19) |
| | | | 40 | 74 (63) | 93 (120) | |
| | | | 50 | 75 (70) | 116 (140) | |
| 3-isotope liquid 14x6x14 | Ar⁺ | 30 | 30 | 47 (101) | 168 (112) | 106 ± 28 (107 ± 17) |
| | | | 40 | 58 (96) | 235 (137) | |
| | | | 50 | 81 (104) | 289 (129) | |
| 2 isotope liquid 14x6x14 | Ar⁺ | 25 | 30 | 135 (21) | 133 (81) | 127 ± 22 (53 ± 21) |
| | | | 40 | 141 (29) | 112 (103) | |
| | | | 50 | 130 (39) | 166 (133) | |
| 2 isotope liquid 14x6x14 | HAr⁺ | 25 | 30 | 55 (54) | 92 (39) | 71 ± 15 (50 ± 17) |
| | | | 40 | 60 (49) | 105 (40) | |
| | | | 50 | 65 (48) | 130 (40) | |

Davy Y. Lo

**Figure Captions**

1. Un-normalized ejection angle distribution of backwardly sputtered atoms for the $HAr^+$ bombardment of the two-isotope liquid target and $Ar^+$ bombardment of the three-isotope crystal target. The two isotopes (25% mass difference) of the liquid target are labeled as 'light-liquid' and 'heavy-liquid' for the lighter and heavier isotopes respectively. Two isotopes (22% mass difference) in the three-isotope crystal target are labeled as 'light-crystal' and 'heavy-crystal' for the lighter and heavier isotope respectively. Here 0° is in the direction of the outward surface normal.

2. Angular distribution (normalized to solid angle) of the cascade flux inside the liquid target after $Ar^+$ bombardment average over the first and second hundred femtoseconds. The average over the first hundred femtoseconds is labeled as 'light-100' and 'heavy-100' for the lighter and heavier isotopes respectively. The average over the second hundred femtoseconds are labeled by the '200' suffix. Here 180° is in the incident direction of the ion beam.

Figure 1 - Angular Spectra of Sputtered Atoms

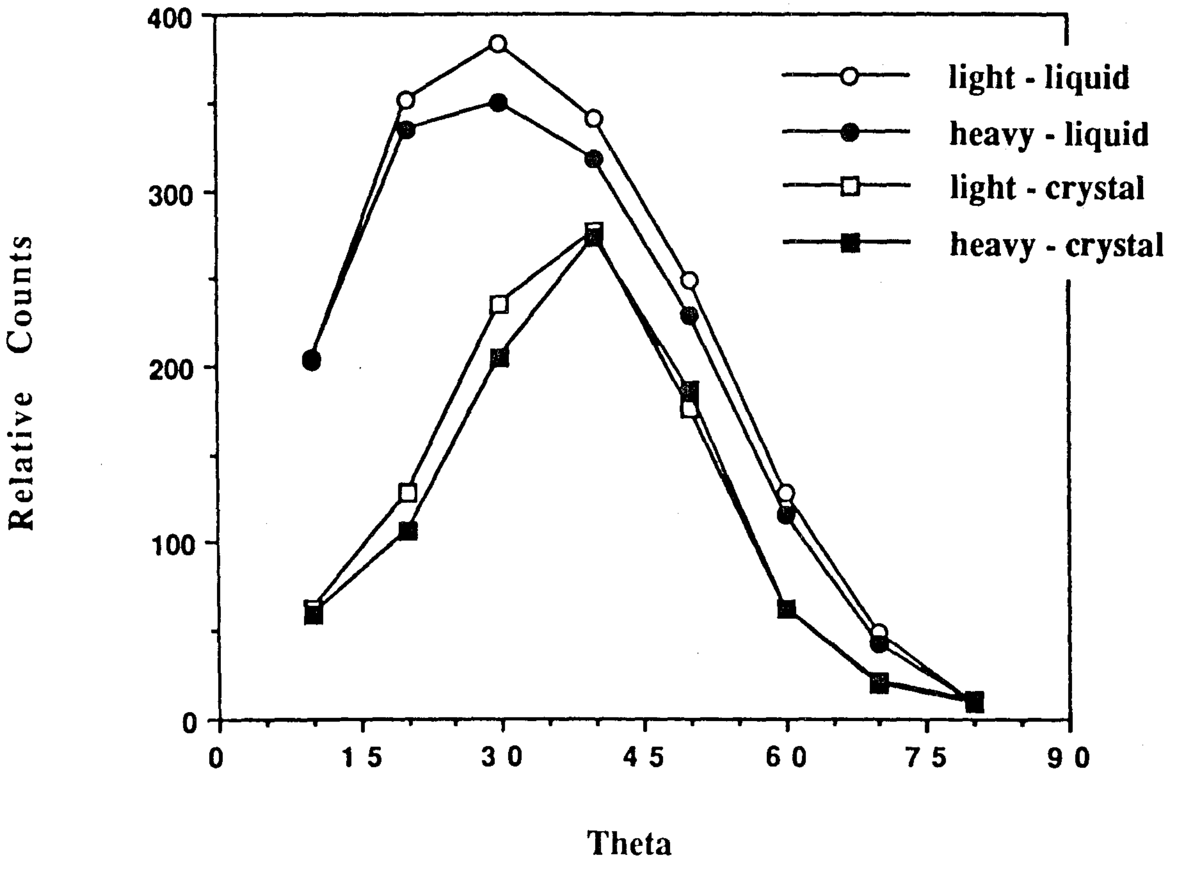

Figure 2 - Cascade Flux Angular Distribution

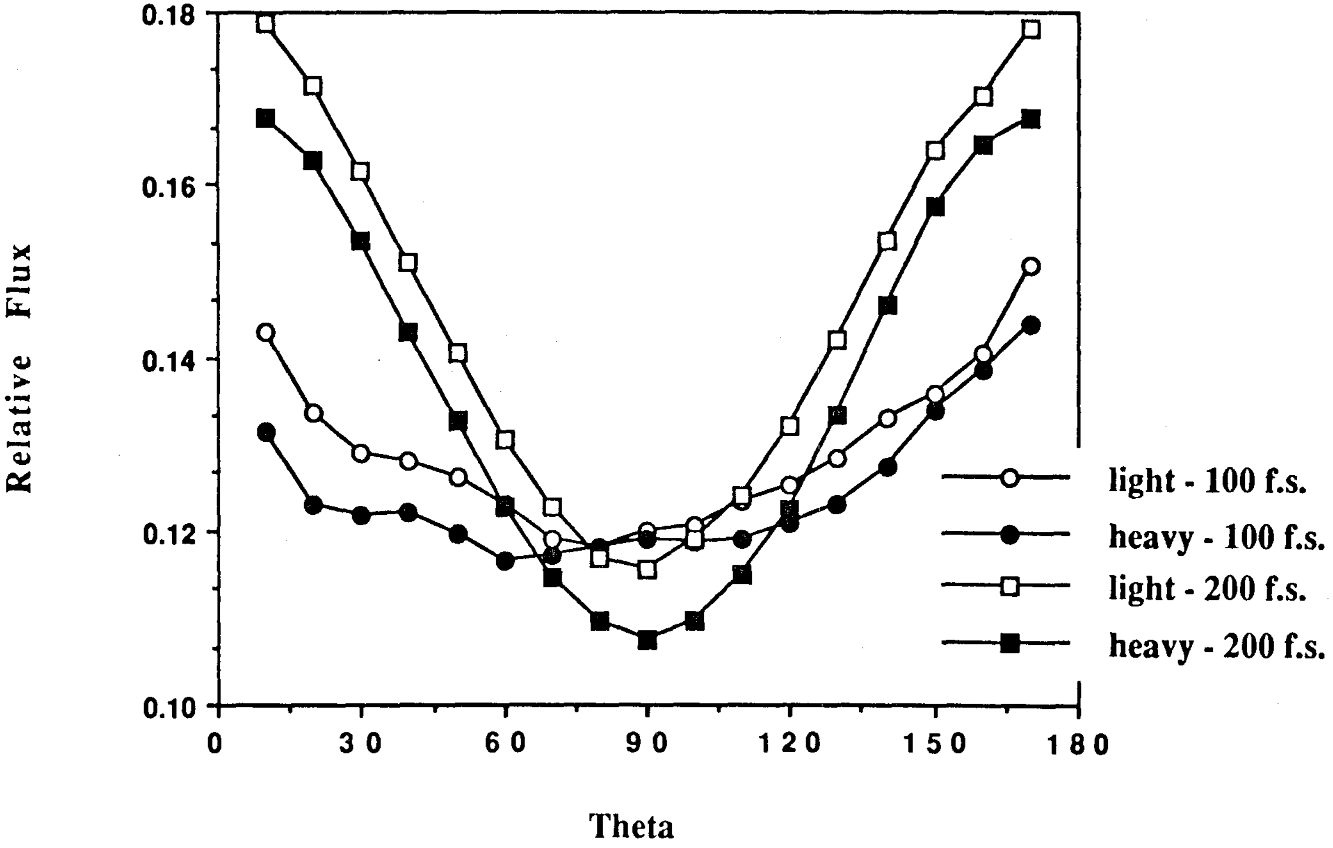

# Chapter 7 - Sputtering with Many-Body Interactions

## 7.1 Introduction

Computer simulations of sputtering have generally used pair potentials to describe the forces between atoms. Pair potential models assume that the total potential energy of a system of atoms may be expressed as a sum of two-body terms. This assumption completely neglects the many-body forces that are due to the presence of electrons. The electronic effects are important in processes where the electron cloud is disturbed from equilibrium and, in particular, in surface ejection during sputtering.

To include these many-body effects, we will use the Embedded- Atom Method (EAM) of Daw and Baskes [1]. In the EAM framework, the total potential energy of a system of atoms is, in addition to the usual pairwise sum of pair interactions, a sum over each atomic site **i** of an embedding function that is a function only of the unperturbed electron density at each site:

$$(7.1) \qquad E = \Sigma_i F_i(\Sigma_{i \neq j} \rho_{ij}) + \tfrac{1}{2}\Sigma_{i \neq j} \phi_{ij}$$

Here, **E** is the total potential energy, **F** is the embedding function, $\phi$ is a purely repulsive pair interaction, and $\rho$ is the free-atom electron density.

We have modified this method for energy ranges appropriate for sputtering calculations and have constructed EAM functions for Rh and Cu. We have also developed a molecular dynamics code that utilizes EAM and successfully have applied it to a simulation of sputtering from Cu single crystals.

The goal of this study is to obtain EAM functions that are capable of quantifying experimental EARN sputtering data from Rh single crystals. EAM functions are also applied to the simulation of sputtering from Cu as a comparison to pair potential results and to observe trends in the resulting sputtering spectra that are also present in the Rh case to establish the universal effects of many-body interactions.

## 7.2 EAM Function Fitting Procedure

For applications in which relatively low energies (~eV) are involved, $F(\rho)$ and $\phi(r)$ may be obtained from equilibrium experimental data such as sublimation energy, elastic constants, and vacancy formation energy [2]. However, for processes in which higher energies are involved, in particular, sputtering, the equilibrium experimental data are hardly adequate since these processes are in general far from equilibrium. For such applications we require the combination $\mathbf{F}$ and $\phi$ to satisfy a semiempirical two atom interaction $\mathbf{V(r)}$ in addition to the experimental equilibrium data. $\mathbf{V(r)}$ is related to $\mathbf{F}$ and $\phi$ by:

$$(7.2) \qquad V(r) = 2\,F(\rho(r)) + \phi(r)\ .$$

$\mathbf{V(r)}$ is obtained by splining a modified Moliere function core to an attractive Morse potential. The Moliere screening radius is adjusted to fit experimental sputtering (or ion scattering) data, while the Morse parameters are obtained from experimental diatomic ground state binding energy, vibrational frequency, and equilibrium separation [3].

Rose et al. [4] showed that the energy equation of state $\mathbf{U}$ may be written as a universal function of the lattice length scale $\mathbf{a}$. In terms of $\mathbf{F(\rho)}$ and $\phi(\mathbf{r})$, the energy per atom for a crystal is:

$$(7.3) \qquad U(a) = F(\Sigma_i \rho(r_i)) + 1/2\, \Sigma_i\, \phi(r_i)\ .$$

Here the sum is over all neighbors of site in a lattice of length scale $\mathbf{a}$. Given $\mathbf{r}$, $\mathbf{F}$ is uniquely determined by $\phi$. By parametrizing $\phi(\mathbf{r})$ and writing the elastic constants and vacancy formation energy in terms of **F**, $\phi$ and $\rho$ [1], we can determine $\phi(\mathbf{r})$ by a least-squares fit with (7.2) as a constraint. Once $\phi$ is determined, **F** is obtained by varying the lattice length scale about the equilibrium value (we used ±10%). So far, $\mathbf{F}(\rho)$ and $\phi(\mathbf{r})$ have been determined in their respective domains about equilibrium. For large $\rho$, we let **F** approach infinity linearly. The linearity of **F** at large $\rho$ will make the interactions exclusively two-body in high energy collisions. For small $\rho$, **F** is given by (7.2). The $\mathbf{F}(\rho)$ in the two regions are joined smoothly by a spline to obtaine the final $\mathbf{F(r)}$. Now, $\phi(\mathbf{r})$ is obtained for all **r** from (7.2). This procedure yields a combination of $\mathbf{F}(\rho)$ and $\phi(\mathbf{r})$ that fits to (7.2) exactly for all **r** and to (7.3) exactly about the equilibrium while fitting to other experimental equilibrium data in a least-squares way.

## 7.3 Summary

A rigorous test of interatomic potentials used in sputtering simulations are the energy and angular resolved neutral (EARN) sputtering spectra. Results from the sputtering simulations using EAM functions obtained in a matter described above are compared to experimental EARN data (Fig. 2 and 3 of App. 7.1).

The energy distribution (Fig. 2 of App. 7.1) obtained using the EAM functions is clearly capable of reproducing the experimentally measured energy distributions. Comparisons are made to both the angular integrated energy distribution and the energy distribution of sputtered atoms in the Wehner spot. Although the EAM functions result in a narrower angular distribution in comparison to experiment, it has the correct peak position and is clearly superior to the result obtained using pair potentials.

The signature provided by the experimental energy and azimuthally resolved polar angle distribution are compared with simulation results using EAM and pair potentials (Fig. 3. of App. 7.1). Here, the pair potential gives a better agreement of the relative intensities of atoms ejecting into different azimuthal angles in the 10-20 eV bin. However, the shape and peak positions are clearly better reproduced by the EAM functions.

The basic trend in the Rh simulations is for the EAM function to produce broader energy and angular distributions with peak positions at higher energies and angles of ejection, respectively, when compared with the pair potential results. The broader energy distributions with peaks at higher energies are again seen in the Cu simulation results for all three low index faces (Fig. 2 of App. 7.2). The broadening is due to EAM functions and is less dramatic in the energy-integrated angular distributions (Fig. 3. of App. 7.2). The difference with the Rh simulation results may be that the broadening is characteristic of the energy and/or azimuthal resolution. However, a clear shift of the angular distribution peak is clearly seen relative to the pair potential results.

Some explanations are attempted to account for these trends that are due to EAM interatomic potentials. Contour plots of the surface potential energy experienced by an escaping atom show that the EAM function gives a much less corrugated potential surface (Fig. 4 of App. 7.1). The energy at the first sign of decorrugation occurs at -1 eV for the pair potential compared to -3 eV in the EAM case. This means that the actual binding energy for planar diffraction (Snell's law) of a surface atom is much larger for EAM potentials. These differences between the surface potentials would explain both the trend for angular and energy distributions peaking at higher ejection angles and energies, respectively.

The EAM approach to interatomic potentials in sputtering simulations is clearly very promising. Further investigations by systematically varying the EAM functions are needed to improve our understanding and ability to reproduce experimental EARN sputtering data quantitatively.

## Reference

1. M. S. Daw and M. I. Baskes, Phys. Rev. **B 29**, 6443 (1984).

2. S. M. Foiles, M. I. Baskes, and M. S. Daw, Phys. Rev. **B 33**, 7983 (1986).

3. K. P. Huber and G. Herzberg, *Molecular Spectra and Molecular Structure*, Van Nostrand Reinhold Co., New York, (1979).

4. J. H. Rose, J. R. Smith, F. Guinea, and J. Ferrante, Phys. Rev. **B29**, 2963 (1984).

PHYSICAL REVIEW B VOLUME 37, NUMBER 13 1 MAY 1988

# Many-body embedded-atom potential for describing the energy and angular distributions of Rh atoms desorbed from ion-bombarded Rh{111}

B. J. Garrison, N. Winograd, D. M. Deaven, and C. T. Reimann
*Department of Chemistry, Pennsylvania State University, University Park, Pennsylvania 16802*

D. Y. Lo and T. A. Tombrello
*Division of Physics, Mathematics and Astronomy, California Institute of Technology, Pasadena, California 91125*

D. E. Harrison, Jr.
*Department of Physics and Chemistry, Naval Postgraduate School, Monterey, California 93943*

M. H. Shapiro
*Division of Physics, Mathematics and Astronomy, California Institute of Technology, Pasadena, California 91125*
*and Department of Physics, California State University, Fullerton, California 92634*

(Received 8 September 1987; revised manuscript received 21 December 1987)

In this paper, we show that many-body interactions are important for describing the energy- and angle-resolved distributions of neutral Rh atoms ejected from keV-ion-bombarded Rh{111}. We compare separate classical-dynamics simulations of the sputtering process assuming either a many-body potential or a pairwise additive potential. The many-body potential is constructed using the embedded-atom method to describe equilibrium properties of the crystal, parameters from the Molière potential to describe close encounters between energized atoms, and parameters from a $Rh_2$ potential to aid the description of the desorption event. The most dramatic difference between the many-body potential and the pair potential is in the predicted kinetic energy distributions. The pair-potential kinetic energy distribution peaks at ~2 eV, whereas the many-body potential predicts a broader peak at ~4 eV, giving much better agreement with experiment. This difference between the model potentials is due to the predicted nature of the attractive interaction in the surface region through which all ejecting particles pass. Variations of the many-body-potential parameters are examined in order to ascertain their effect on the predicted energy and angular distributions. A specific set of parameters has been found which leads to excellent agreement with recent experimental trajectory measurements of desorbed Rh atoms.

## I. INTRODUCTION

The development of many-body interaction potentials to describe the forces among large ensembles of atoms (e.g., solids or liquids) is presently in its infancy. Over the years investigators have sought to find systems and scattering regimes where these types of potential functions may be expressed in a mathematically tractable form. One such process is the ejection of atoms due to 500–5000 eV particle bombardment of solids (i.e., sputtering). In this case atoms are ejected from the solid with a kinetic energy $E_{\text{kin}}$ distribution which maximizes at 2–10 eV and which decreases as $E_{\text{kin}}^{-2}$ up to energies which are a significant fraction of the energy of the incident particle. The complex atomic motion subsequent to the ion-bombardment event is clearly initiated by close encounters between colliding atoms in the solid. These types of interactions may provide an excellent model system for developing an accurate many-body interaction potential.

Since 1960 particle bombardment events have been simulated by computer models which assume pairwise additive potential functions.[1] The simplest approach is to assume that the interactions are purely repulsive and that the collision dynamics can be described by the binary collision approximation where each particle is allowed to interact with only the nearest atom at a given time.[2] On the other hand, we believe that at the energies at which most particles eject, 2–10 eV, simultaneous interactions are not negligible and in fact play a dominant part in controlling the collision dynamics.[3-7] Due to computational restrictions, our full lattice descriptions have thus far been limited to pairwise additive potentials, although attractive interactions have been included.

These potentials have been quite successful at elucidating mechanisms of particle ejection, and at allowing calculation of semiquantitative aspects of the sputtering process.[4] However, a quantitative comparison between theory and experiment has been hindered by a scarcity of detailed experimental data. The computer simulations using single crystal targets yield direct information concerning the trajectories of ejecting neutral atoms. Early experiments were capable only of examining energy-integrated or angle-integrated neutral distributions from damaged targets or of examining trajectories of secondary ions. The motion of the ions could be detected with high sensitivity but the distributions had to be corrected for the image forces created by the charge.[8] A new method based on the multiphoton resonance of neutral atoms after they have desorbed from the target surface has recently been developed. The technique is capable of measuring the energy- and angle-resolved neutral (EARN) distributions of sputtered atoms[9-11] with sensitivity sufficient to avoid surface damage. These experiments provide the best trajectory data yet available and force a critical test of assumed interaction potentials and scattering dynamics.

In a previous study we described the EARN distribution of Rh atoms ejected from Rh{111} with a computer simulation using pairwise additive interaction potentials.[7] Although the overall trends of azimuthal anisotropies and relative intensities of angular peaks were well described, the position of the peaks and the peak widths in both the polar angle and energy distributions differed between the experimental and calculated results. Variation of the parameters in the potential within physically reasonable bounds did not significantly improve agreement.

In this paper we present the first use of many-body potentials to describe the ejection of atoms from solid surfaces due to keV ion bombardment. The potential is derived from the embedded-atom method (EAM) of Daw and Baskes.[12,13] This many-body potential significantly improves the agreement between the measured and calculated peak positions and widths in the energy and angular distributions of Rh atoms ejected from Rh{111}. Several variations of the potential are examined to determine the influence of selected parameters on the calculated distributions. The results show that the EAM approach yields excellent agreement with the expected kinetic energy distributions for all potentials tested. However, the angular distributions are influenced by a number of parameters. We especially examine the difference between calculated trajectories in the surface region when using an EAM potential as compared to earlier pair-potential calculations.

## II. DESCRIPTION OF THE CALCULATION

Our prescription for modeling the ion-bombardment process has been described in detail elsewhere for the $Ar^+$ ion bombardment of Rh{111}.[7] The critical difference in the present study is that a many-body EAM potential has been used to describe the Rh metal interaction. The EAM utilizes an ion-core representation of the metal atom embedded into the surrounding electron sea.[12-14] The energy for the $i$th atom is given by

$$E_i = F\left[\rho_i = \sum_j \rho_{\text{atomic}}(r_{ij})\right] + \frac{1}{2}\sum_j \phi(r_{ij}) , \qquad (1)$$

where $r_{ij}$ is the distance between the $i$th atom and the $j$th atom. The first term is the embedding function, which is the energy of the interaction of the ion core with the electron sea of density $\rho_i$. The embedding function is characteristic of a particular atom type and is assumed not to depend on the source of the electron density. Thus the embedding function for Rh is transferrable from one environment to another if the electron density is known. For convenience, this density is assumed to be the instantaneous sum of the atomic electron densities of the other atoms at the position of the atom of interest. Since these densities depend only on the distance between the atoms forces are easily extracted for dynamics simulations. The second term is short ranged and is the ion-core repulsion at a distance of separation, $r_{ij}$, of the two cores. It is of interest that the EAM has been successfully applied to describing bulk properties at thermal energies and even to predicting surface reconstructions.[12,16] However, to our knowledge it has not been applied to systems where parts of the solid actually dissociate as is the case with evaporation and ion-induced desorption.

The embedding functions are empirically derived, and as a consequence the $F(\rho)$ and the $\phi(r)$ terms must be systematically evaluated. Foiles, Baskes, and Daw have developed a prescription for fitting these functions to equilibrium properties of the metal of interest.[14] To describe the ion-bombardment process, it is necessary to consider that atomic positions may be displaced far from their equilibrium values. The energetics of an atom as it ejects from the surface, and the details of close encounters with other atoms are also important, indicating that a slightly different fitting procedure is necessary. Our approach, as described in the Appendix, is basically the same as that of Foiles, *et al.* except that the potential form also incorporates parameters appropriate for $Rh_2$ (i.e., in the low-density regime) and for the repulsive wall which is important during close encounters (i.e., in the very-high-density regime).

A number of embedding functions for Rh with different repulsive walls and attractive regions were used for simulations of the EARN distributions. We found that, to reproduce the experimental energy distributions, the value of the surface binding energy for the EAM potential must be $\geq 5$ eV. Here we have chosen to use Eq. (1) to define the energy of an atom in the surface region. This definition results in a value of the surface binding energy which is less than the true energy cost to remove an atom from the substrate.[17-19] Since the density regimes appropriate for the surface region and for $Rh_2$ overlap, we are not able at this stage to utilize the spectroscopic constants for the dimer and also obtain a surface binding energy of $>5$ eV. By adjusting these values, however, as described in the Appendix, potential forms were found that fit the experimental angular distributions in the 20–50 eV range (EAM-C), and in the 10–20 eV range (EAM-D). Two other potentials, (EAM-A and EAM-B), that are approximately linear combinations of EAM-C and EAM-D, are also tested in this work. The details of the determination of EAM-A are given in the Appendix. In summary, our present strategy for finding a representative many-body potential consists of utilizing the previously developed formalism to calculate forces of atoms near equilibrium positions, and then semiempirically adjusting the potential shapes appropriate for close encounters and for dissociations until the function provides a physically accurate representation of the experimental results.

The EAM form of the total potential energy expression can be obtained in a purely empirical way,[20] but its validity can be more rigorously justified by deriving it as an approximation method in formal effective-medium theory.[21] The derivation is based on the replacement of the effective-medium expression for the energy of an atom embedded in an arbitrary host with the energy of the atom in a homogeneous electron gas. In the effective-medium prescription, the density is determined self-consistently. In the EAM the density of the homogeneous electron gas is used to approximate the true density. The EAM replaces a functional of the host electron density with a function of the electron density at a point. In this context the EAM "embedding function" is interpreted as the cohesive energy of the atom in jellium. The pairwise additive term can be obtained with first-order perturbation theory on the jellium system with an external potential representing the host.[21] For proper physical interpretation, the EAM "embedding function" must have a low-density limit of zero, unlike the hypothetical jellium limit which reflects the formation of a negative ion for chemically active elements in the limit of extremely low jellium density. We note that Norskov[22,23] has shown that a second correction term reflects the difference between the one-electron spectrum of an atom embedded in jellium and the same atom embedded in a solid host. This correction accounts for the hybridization or band energy resulting from the formation of relatively delocalized states in the solid. The keV ion-bombardment process studied in this work causes severe local disruptions of the equilibrium lattice and leads to atomic desorption. Since the hybridization energy during this process is likely to differ significantly from that of a uniform lattice, the knowledge of the uniform lattice one-electron spectrum is insufficient to correct for hybridization effects during the desorption event. In principle, this correction could be made by calculating the instantaneous band structure at each simulation timestep,[24] but this completely circumvents any computational advantages of the semiempirical form. Therefore, we employ the EAM form [Eq. (1)] in its original form as a parametrized mathematical representation of the potential energy hypersurface which includes many-body terms in a convenient but theoretically justified manner.

### III. RESULTS AND DISCUSSION

Highly reliable trajectory information is now available over all angle and kinetic energy domains for Rh atoms desorbed from ion-bombarded Rh{111}. To act as a standard subset of reference data for our computer simulations, we have chosen to select angle-integrated kinetic energy distributions of the ejected Rh atoms and polar angle distributions along three azimuthal directions of the {111} crystal face (Fig. 1) for three secondary particle energy ranges. These data, as well as computer simulations of these trajectories using pair potentials, have been reported previously.[7]

The most dramatic difference observed between the pair potential and the EAM potential is in the predicted distributions arising in the angle-integrated energy distributions. As shown in Fig. 2, the distributions from experiment and calculations using the EAM-A interaction are in excellent agreement while the calculated distribution using pair potentials is significantly different. The peaks in the polar angle distributions as calculated from the EAM-A potential (Fig. 3) are also found to increase by about 10° from those predicted by the pair potentials. The improved agreement in the energy distributions is fairly consistent among all the EAM potentials tested but, as discussed herein, the angular distributions are dependent upon the specifics of the EAM potential parameters. It is important to note that the azimuthal anisotropies (i.e., the ratio of the intensities in the $\phi=-30°$, $+30°$, and $0°$ directions) are well described by the pair potential. In addition, the intensity in the normal direction ($\theta-0°$) increases relative to the intensity at $\theta\approx40°$ as the ejected Rh atom kinetic energy (KE) increases in both the experiment and pair-potential distributions.

Is this improved agreement in the predicted KE distributions fortuitous or is there a sound basis for it? It has been clear to us in the past that the pair-potential description in the surface region is inadequate partly due to the changing number of nearest-neighbor atoms at the

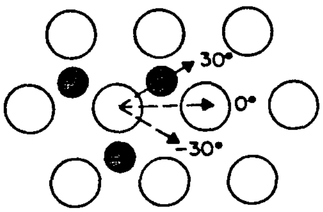

FIG. 1. Rh{111} crystal face. The open circles are first-layer atoms and the solid circles represent second-layer atoms. The azimuthal directions of $\phi=-30°$, $0°$, and $30°$ are shown.

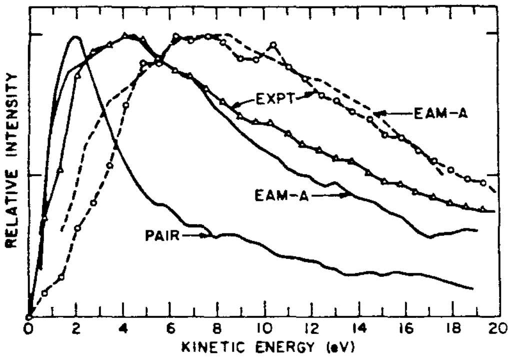

FIG. 2. Experimental and calculated kinetic energy distributions. In all cases the curves are peak normalized. The two experimental curves are the angle-integrated distribution and one at $\phi=-30°$ and $\theta=40\pm3°$. The EAM-A curves are the angle-integrated distribution and one at $\phi=-30°$ and $\theta=38\pm7.5°$. *Only the angle-integrated distribution is shown for the pair-potential calculation.* The angle-integrated distributions are shown as solid lines and the ones at $\theta\approx40°$ are dashed lines.

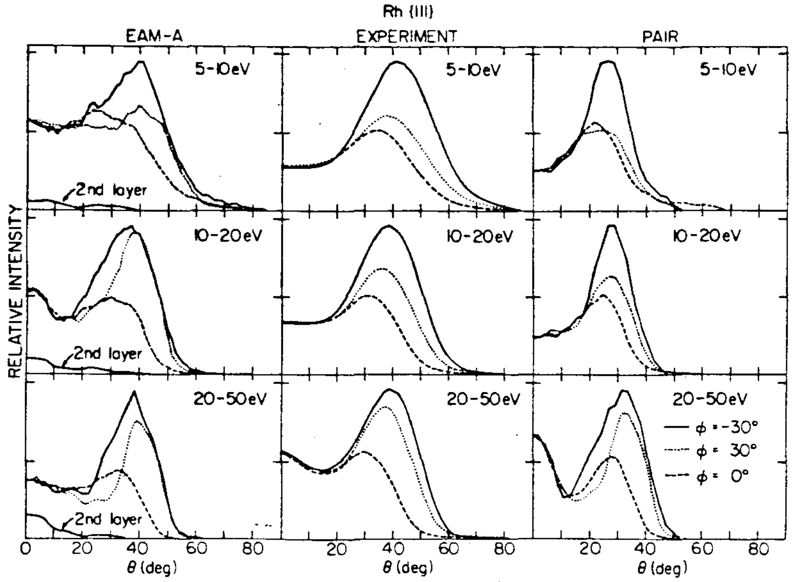

FIG. 3. Polar angle distributions for various azimuthal angles for fixed secondary kinetic energy of the Rh atoms. In each frame the data are normalized to the $\phi=-30^\circ$ peak intensity. For the calculated data the full width at half maximum (FWHM) of the resolution is 15° in the polar angle. A constant solid angle is used in the histogramming procedure. The experimental resolution is approximately the same. The surface normal corresponds to $\theta=0^\circ$. The curve marked 2nd layer is the polar distribution along $\phi=-30^\circ$ for the ejected second-layer atoms.

interface. Satisfactory solutions to this regime were not forthcoming partially since we did not have the detailed data that exposed the nature of the deficiencies. Contour plots of the energy of one atom ejecting from a site in the Rh{111} surface for the pair and the EAM-A and EAM-C potentials are shown in Fig. 4. There are several features apparent in these plots which have important implications for the particle-ejection process. The surface binding energy of the EAM potentials is larger (5.1–5.3 eV) than that of the pair potential (4.1 eV), even though all of the potentials have been fit using the bulk heat of atomization of Rh of 5.75 eV. It is often suggested that the peak in the KE distribution is proportional to the energy cost to remove an atom from the surface,[17–19] providing a logical explanation for the fact that the peak in the EAM energy distributions occurs at a higher value than for the pair potential. In addition, the EAM potentials are relatively flat in the attractive portion of the entire surface region. There is a 3–4 eV attraction for the ejecting atom even above a neighboring atom. The pair potential has only ~1 eV overall attraction. Thus, particles ejecting at more grazing angles will experience a larger attraction to the surface when moving under the influence of the EAM potential than when moving under the influence of the pair potential. This effect will shift the peak in the KE distribution toward larger values and will bend particles further away from the surface normal, moving the peak in the polar distributions to higher values of $\theta$. Our feeling is that the more planar descrip-

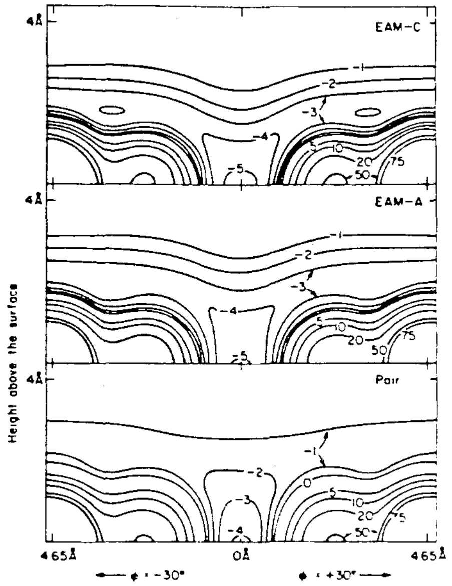

FIG. 4. Contour plots of the potential energy [in eV from Eq. (1)] of a Rh atom ejecting from a Rh{111} surface for the pair potential, EAM-A and EAM-C. The ordinate is the height of the atom above the surface (Å). The abscissa is the position of the atom (Å) along the surface in the $\phi=\pm30^\circ$ azimuths.

tion of the surface region is more realistic and thus the EAM potential is more appropriate than pair potentials in the surface region.

The larger effective surface binding associated with the EAM description results in fewer particles ejected with low KE's. To a first approximation, then, the change in the features in the energy distribution are a result of a decrease in the magnitude of the peak intensity, resulting in a more prominent high KE tail. This increased binding energy also dramatically affects the total yield. For the pair-potential calculation the calculated yield is 6.1 Rh atoms per incident Ar particle, while for EAM-A the yield is 3.7 atoms per Ar atom. This lower value is closer to the range of experimental yields (see, for example, Ref. 25) than the pair-potential value. Note also that the ratio of the yields between the two methods of calculation is $6.1/3.7=1.6$ whereas the ratio of surface binding energies is only 5.1/4.1 or 1.2. Transport theories of sputtering suggest that the yield is inversely proportional to the binding energy.[25] From our calculations it is clear that the nature of the potential surface also influences the expected yield.

The energy distributions of the atoms that eject into the peak of the polar distribution along $\phi=-30^\circ$ (often called the "spot") are also shown in Fig. 2. The agreement between the experimental and EAM-A distributions is remarkable. This energy distribution peaks at $\sim 7$ eV whereas the angle-integrated distributions peak at $\sim 4$ eV. In this energy regime the particles that eject into this "spot" are "hotter" than the particles ejected in other directions.

The angular distributions for three other Rh EAM potentials are given in Fig. 4. Although numerous other potentials were tested, these four (EAM-A, -B, -C, -D) yield the most reasonable distributions and provide a base for determining the parameters which most influence the experimental results. We have subjectively chosen several features of the angular distributions that are important to describe. The first is the shift in azimuthal anisotropy as the Rh atom KE increases. At 5–10 eV (Fig. 3) the $\phi=-30^\circ$ experimental intensity is greater than for the other two azimuths. For 20–50 eV the $\phi=\pm 30^\circ$ intensities are almost equivalent and of greater intensity than the $\phi=0^\circ$ case. The second is that the peak in the $\phi=\pm 30^\circ$ directions should be observed at about 40°. (The peak position along $\phi=0^\circ$ is always less due to increased blocking in this direction.) Finally, in the 20–50 eV range the intensity in the direction normal to the surface ($\theta=0^\circ$) should be approximately half of the peak intensity. From our calculations using pair potentials we believe that a significant fraction of the intensity of the particles ejected in the normal direction at 20–50 eV is due to second-layer atoms that are focused by the three surface atoms surrounding it.[7] Since we ultimately want to examine adsorbates that can either bond directly above a second-layer atom or above a third-layer atom, it is important to be able to describe the ejection of the second-layer atoms reasonably well. Note that the overall ejection is dominated by the first-layer ejection, but in the specific energy and angle space in question the second-layer ejection is important. With these criteria, potential EAM-B is not considered satisfactory since the normal emission intensity at 20–50 eV is too low and the polar angle peak in the 5–10 eV range is $\sim 30^\circ$. Potential EAM-C is deficient since the normal emission is too intense in all energy ranges. Potential EAM-D exhibits weak normal emission in the 20–50 eV range, the polar angle peak position is $< 35^\circ$ and the 5–10 eV azimuthal angle distributions are almost isotropic.

Ultimately it is desirable to correlate critical features of the potentials with specific parts of the EARN distributions. This goal is complicated by the fact that the attractive part of the surface potential not only influences the ejection process but also influences the effective size of the atoms. For second-layer ejection the energy barrier that the atom must overcome in moving through the first layer is also important. Finally, the potential influences the dynamics of all of the motions that give rise to energizing an ejecting atom. Given these complexities we have chosen to examine three slices of the potential surface. The first slice is shown in Fig. 4 and indicates the energy required to remove a first-layer atom from the solid from various positions. The second slice is shown in Fig. 5 and indicates the energy of an atom [Eq. (1)] in the second layer as a function of the distance to another second-layer atom. This representation provides an indication of the magnitude of the interaction between atoms within the solid. The final slice is shown in Fig. 6 and indicates the energy of a second-layer atom as it moves upward through the threefold hollow site in the first layer.

We first examine the effect of the magnitude of the barrier on the trajectories of atoms escaping from the second layer. As shown in Fig. 6, potentials EAM-A and EAM-C are constructed with the lowest barriers and, as is evi-

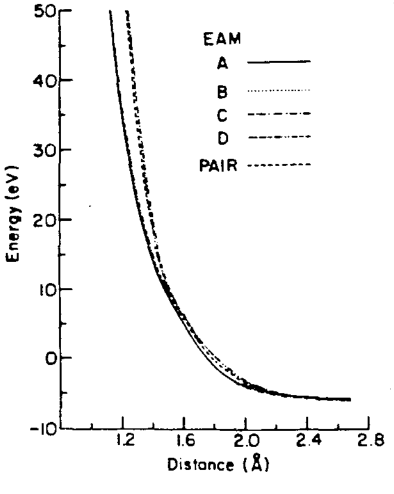

FIG. 5. Energy of an atom in the second layer as a function of the distance to another atom in the second layer for the various potentials. The equilibrium separation is 2.69 Å.

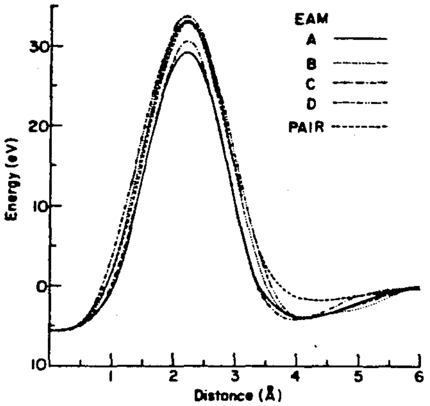

FIG. 6. Energy of an atom in the second layer as it moves vertically through the threefold hollow site in the first layer and towards the vacuum.

dent from Figs. 3 and 7, these barriers result in the largest amount of second-layer ejection for the 20–50 eV particles. As this barrier height is increased as with EAM-B and EAM-D, the second-layer ejection is effectively suppressed. The energy spectrum normal to the surface and the percentage of atoms that eject from below the top layer are particularly sensitive to the barrier height.

The size of the atoms as given by the curves in Fig. 5 also aid in interpreting the EARN distributions. As described in the Appendix, the short-ranged interaction in these EAM potentials is described by the Moliére potentials.[26] There has been considerable debate in the literature as to the appropriate value for the Firsov screening length.[27] We have tested the sensitivity of the potentials to this parameter. For EAM-B, -C, and for the pair-potential calculation, the full Firsov screening length is used. Comparison of results of simulations of keV ion scattering from surfaces has suggested that smaller screening lengths may be more appropriate.[27] Therefore, for EAM-A, -D the Firsov screening length is scaled by 0.9. As a consequence of these changes, for energies above ~10 eV (Fig. 5) potentials EAM-B, -C describe effectively larger atoms than EAM-A, -D. For the low-energy region the atoms represented by EAM-B, -D are bigger than EAM-A, -C.

The size of the interactions influences the peak position in the polar angle distribution. The larger the effective size of the atoms, the more the ejecting atom will be deflected towards the surface normal. For example, the angular distributions resulting from trajectories calculated using EAM-B, -D exhibit peak positions closest to the normal. It is EAM-B, -D that are largest in the lower-energy regime, the regime which is apparently most important in determining the polar angle of maximum intensity.

The most serious discrepency between experimental and calculated angular distributions for all of the EAM potentials is that the calculated angular distributions for 5–10 eV and 10–20 eV particles appear to have a $\cos^n\theta$ background ($n \approx 2-3$) that is not apparent in the experimental distributions nor in the calculated pair-potential distribution. Although the reasons for this discrepancy are not yet clear, it is possible that this background is related to the degree of smoothness in the surface of the

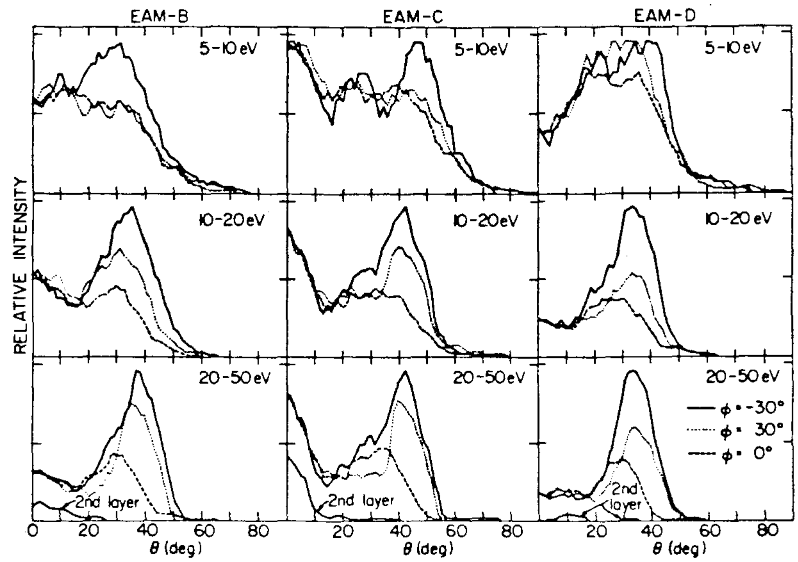

FIG. 7. See the caption to Fig. 3.

EAM potentials. It is possible that future improved descriptions of the surface electron density will further improve the agreement between experiment and theory.

## IV. CONCLUSIONS

The energy and angular distributions of Rh atoms ejected from a Rh{111} surface due to keV-Ar-atom bombardment have been modeled with classical dynamics simulations and a many-body EAM potential. We find that the EAM potential significantly improves the agreement between calculated and experimental distributions over previous simulations using a pairwise additive potential. The important differences between the pair and EAM potentials occur in the surface region where the EAM potential predicts a larger surface binding energy and a more planar potential. This effect causes fewer atoms to eject with low kinetic energy and results in an energy distribution which is broader and which peaks at a larger energy than that calculated with the pair potential.

It is apparent that a many-body potential is necessary to quantitatively describe the EARN distributions although the EAM-A potential does not provide a perfect description of the experimental scattering data. Within the embedded-atom method a different prescription for obtaining $F(\rho)$ and $\phi(r)$ may improve the fit. Perhaps a different many-body potential is more appropriate. In any event, a more detailed understanding of how various parts of the potential surface influence the scattering events will undoubtedly improve our understanding of the interaction potential.

## ACKNOWLEDGMENTS

The authors greatly appreciate the assistance of M. Daw, S. Foiles, and M. Baskes who provided their computer code for determining forces with the EAM potentials and some embedding functions that were used in the evaluation of the appropriateness of EAM potentials for sputtering. The financial support of the National Science Foundation, the Office of Naval Research, the Air Force Office of Scientific Research, the Foundation Research Program of the Naval Postgraduate School, the Shell Corporation, and the IBM Corporation is gratefully acknowledged. B.J.G. additionally appreciates support from the Camille and Henry Dreyfus Foundation. The Pennsylvania State University supplied a generous grant of computer time for these calculations.

## APPENDIX: Determination of $F(\rho)$ and $\phi(r)$

The electron density-dependent part of the total energy $F(\rho)$ was obtained in this work by a fitting procedure that yields a tabulation of $F(\rho)$ over a large number of closely spaced points in $\rho$ space from which an interpolation scheme may be used to evaluate $F(\rho)$ during the dynamics simulation. The specific fitting procedure followed is summarized herein.

(1) A cubic spline of the spherical atomic density function $\rho(r)$ for rhodium was defined using the following input data:

$$\rho(r)=\begin{cases}0, & r\geq 4.23\ \text{Å}\\ \rho_{\text{SCF}}(r), & 0.56\ \text{Å}<r<4.23\ \text{Å}\\ \text{linear with negative slope}, & r<0.56\ \text{Å}\ ,\end{cases}$$

where $\rho_{\text{SCF}}(r)$ is a spherically averaged[13] self-consistent-field density function.[28] The splined region near $r=0$ where $\rho_{\text{SCF}}(r)$ vanishes is necessary to allow the definition of a cubic spline for an inverse density function $r(\rho)$. The local density and the summed nuclear repulsion energy at a lattice site are then

$$\rho(a)=\sum_{m=1}^{n}\rho[r_m(a)],\quad \phi(a)=\sum_{m=1}^{n}\phi[r_m(a)]\ ,$$

where $a$ is the face centered cubic (fcc) lattice constant, $n$ is the number of neighbors, and $r_m(a)$ is the distance to the $m^{\text{th}}$ neighbor. In this work, $n$ was large enough to include all neighbors inside a 4.23 Å cutoff range.

(2) An effective pair interaction was constructed representing the energy of an isolated rhodium dimer

$$V(r_{\text{dimer}})=\begin{cases}V_{\text{Morse}}\ (r_{\text{dimer}}), & r_{\text{dimer}}>1.9\ \text{Å}\\ \text{cubic spline}, & 1.48\ \text{Å}r_{\text{dimer}}\leq 1.9\ \text{Å}\\ V_{\text{Molière}}\ (r_{\text{dimer}}), & r_{\text{dimer}}<1.48\ \text{Å}\ .\end{cases}$$

The Morse potential was of the form

$$V_{\text{Morse}}(r)=D_e(e^{-2\beta(r-r_0)}-2e^{-\beta(r-r_0)})F(r)\ ,$$

where $F(r)$ is a Tersoff function[29] designed to switch the potential smoothly to zero at the cutoff distance 4.23 Å,

$$F(r)=\begin{cases}\frac{1}{2}\left[1-\sin\pi\left[\frac{r-4.23\ \text{Å}+\delta}{2\delta}\right]\right], & r\geq 4.23\ \text{Å}-2\delta\\ 1, & r<4.23\ \text{Å}-2\delta\ .\end{cases}$$

The original goal was to use the spectroscopic values of the $Rh_2$ to determine $D_e$, $\beta$, and $r_0$ as then the absolute yield of sputtered $Rh_2$ species could be predicted. Unfortunately, the region of $\rho$ space that is important for the dimer is also important for the surface region, and values of $D_e$, $\beta$, and $r_0$ appropriate for the dimer resulted in potentials with surface binding energies $<5$ eV. As discussed in the text, these potentials did not predict the peak position in the experimental energy distribution, and thus at this time we use $D_e$, $\beta$, and $r_0$ as parameters. The value of $\delta$ used was 0.772 Å. The Molière potential $V_{\text{Molière}}$ is described in Ref. 26.

(3) A region of $\rho$ space $(\rho_1, \rho_2)$ containing the equilibrium density $\rho_0$ of solid fcc rhodium was defined by a ±10% contraction (expansion) of the lattice constant around its equilibrium value of 3.80 Å. Given $\phi(r)$, $F(\rho)$ may be defined in this region by using the universal equation of state described by Rose *et al.*[30] to determine the

total energy of the solid and requiring equality between this and the EAM total energy expression:

$$E(a)=-E_s(1+a^*)e^{-a^*}=F[\rho(a)]+\tfrac{1}{2}\phi(a)\ ,$$

where

$$a^*=\left[\frac{a}{a_0}-1\right](9B\Omega/E_s)^{1/2}\ .$$

Here, $E_s$ is the equilibrium sublimation energy, $a_0$ is the equilibrium lattice constant, $B$ is the bulk modulus, and $\Omega_0$ is the equilibrium volume per atom.

(4) A trial nuclear repulsion $\phi(r)$ was chosen to have the form[14]

$$\phi(r)=\frac{Z(r)^2}{r}\ ,$$

where

$$Z(r)=Z_0(1+\epsilon e^{r\nu})e^{-\alpha r}\ .$$

The crystal elastic constants $c_{11}$, $c_{12}$, $c_{44}$, and the vacancy-formation energy $E_{1v}^{f}$ may be calculated given $F(\rho)$ and $\phi(r)$.[14] Using the definition of $F(\rho)$ in step (3) and the trial $\phi(r)$, the adjustable parameters $\alpha$, $\epsilon$, and $\nu$ in $\phi(r)$ were fit using a nonlinear least squares technique to the reasonable elastic constants and the vacancy formation energy of fcc rhodium. Since $c_{11}$ and $c_{12}$ are related through the bulk modulus which appears in the equation of state, the fit was made to $c_{11}$, $c_{44}$, and $E_{1v}^{f}$. The parameter values used in this work were $\alpha=2.105$, $\epsilon=2.510$, and $\nu=1.387$.

(5) The final $F(\rho)$ was defined as a cubic spline of a composite of three functions

$$F(\rho)=\begin{cases}\tfrac{1}{2}[V(r_{\text{dimer}})-\phi(r_{\text{dimer}})]\ , & \rho\le\rho_1\\ E(a)-\tfrac{1}{2}\phi(a), & \rho_1\le\rho\le\rho_2\\ \text{linear}, & \rho>\rho_2\ .\end{cases}$$

In the $\rho\le\rho_1$ region, the inverse atomic density function $r(\rho)$ must be used to relate $\rho$ space and $r_{\text{dimer}}$-space. In the $\rho_1\le\rho\le\rho_2$ region, the relation of $\rho$ to the lattice constant $a$ as defined in step (1) is needed.

(6) The final $\phi(r)$ is expressed as a cubic spline defined from points in

$$\phi(r)=V(r)-2F[\rho(r)]\ .$$

This step is necessary to make the EAM total energy expression consistent with the effective pair of interaction, $V(r)$. This definition of $F(\rho)$, $\rho(r)$, and $\phi(r)$ ensures that dimerlike species interact with an effective pair potential $V(r_{\text{dimer}})$, and also that the bulk behavior is properly described. In addition, we have control over the size of the short-ranged close encounter region.

---

[1] J. B. Gibson, A. N. Goland, M. Milgram, and G. H. Vineyard, Phys. Rev. **120**, 1229 (1960).

[2] M. T. Robinsen and I. M. Torrens, Phys. Rev. B **9**, 5008 (1974).

[3] D. E. Harrison, Jr., J. P. Johnson III, and N. S. Levy, Appl. Phys. Lett. **8**, 33 (1966).

[4] B. J. Garrison and N. Winograd, Science **216**, 805 (1982).

[5] M. H. Shapiro, P. K. Haff, T. A. Tombrello, D. E. Harrison, Jr., and R. P. Webb, Radiat. Eff. **89**, 243 (1985).

[6] D. Y. Lo, M. H. Shapiro, and T. A. Tombrello, Mater. Res. Soc. Symp. Proc., **174**, 449 (1987).

[7] B. J. Garrison, N. Winograd, C. T. Reimann, and D. E. Harrison, Jr., Phys. Rev. B **36**, 3516 (1987).

[8] R. A. Gibbs, S. P. Holland, K. E. Foley, B. J. Garrison, and N. Winograd, Phys. Rev. B **24**, 6178 (1981).

[9] J. P. Baxter, G. A. Schick, J. Singh, P. H. Kobrin, and N. Winograd, J. Vac. Sci. Technol. **4**, 1218 (1986).

[10] G. A. Schick, J. P. Baxter, J. Singh, P. H. Kobrin, and N. Winograd, in *Secondary Ion Mass Spectrometry-SIMS V*, Vol. **44** of *Springer Series in Chemical Physics* edited by A. Benninghoven, R. J. Colton, D. S. Simons, and H. W. Werner (Springer-Verlag, New York, 1986), p. 90.

[11] N. Winograd, P. H. Kobrin, G. A. Schick, J. Singh, J. P. Baxter, and B. J. Garrison, Surf. Sci. **176**, 1817 (1986).

[12] M. S. Daw and M. I. Baskes, Phys. Rev. Lett. **50**, 1285 (1983).

[13] M. S. Daw and M. I. Baskes, Phys. Rev. B **29**, 6443 (1984).

[14] S. M. Foiles, M. I. Baskes, and M. S. Daw, Phys. Rev. B **33**, 7983 (1986).

[15] B. W. Dodson, Phys. Rev. B **35**, 880 (1987).

[16] S. P. Chen, A. F. Voter, and D. J. Srolovitz, Phys. Rev. Lett. **57**, 1308 (1986).

[17] B. J. Garrison, N. Winograd, D. Lo, T. A. Tombrello, M. H. Shapiro, and D. E. Harrison, Jr., Surf. Sci. **180**, L129 (1987).

[18] M. W. Thompson, Philos. Mag. **18**, 377 (1968).

[19] R. Oliva, R. Kelly, and G. Falcone, Nucl. Instrum. Methods **B19–20**, 101 (1987).

[20] M. W. Finnis and J. E. Sinclair, Philos. Mag. A **50**, 45 (1984).

[21] M. Manninen, Phys. Rev. B **34**, 8486 (1986).

[22] J. K. Norskov, Phys. Rev. B **26**, 2875 (1982).

[23] K. W. Jacobsen, J. K. Norskov, and M. J. Puska, Phys. Rev. B **35**, 7423 (1987).

[24] R. Car and M. Parrinello, Phys. Rev. Lett. **55**, 2471 (1985).

[25] P. Sigmund, Phys. Rev. **184**, 383 (1969).

[26] I. M. Torrens, *Interatomic Potentials* (Academic, New York, 1972).

[27] B. Poelsma, L. K. Verheij, and A. L. Boers, Surf. Sci., **64**, 554 (1977).

[28] E. Clementi and C. Roetti, *Atomic Data and Nuclear Data Tables* (Academic, New York, 1974) Vol. 14, Nos. 3 and 4, p. 231.

[29] J. Tersoff, Phys. Rev. Lett., **56**, 632 (1986).

[30] J. H. Rose, J. R. Smith, F. Guinea, and J. Ferrante, Phys. Rev. B **29**, 2963 (1984).

# Theoretical studies of ion bombardment: Many-body interactions

Davy Y. Lo, Tom A. Tombrello, and Mark H. Shapiro
*Division of Physics, Mathematics, and Astronomy, California Institute of Technology, Pasadena, California 91125*

Barbara J. Garrison and Nicholas Winograd
*Pennsylvania State University, University Park, Pennsylvania 16802*

Don E. Harrison, Jr.
*Department of Physics, U.S. Naval Postgraduate School, Monterey, California 93940*

Many-body forces obtained by the embedded-atom method are incorporated into the description of low-energy collisions and surface ejection processes in molecular dynamics simulations of sputtering from metal targets. Bombardment of small, single-crystal Cu targets (400–500 atoms) in three different orientations ({100}, {110}, {111}) by 5-keV Ar$^+$ ions have been simulated. The results are compared to simulations using purely pairwise additive interactions. Significant differences in the spectra of ejected atoms are found.

## I. INTRODUCTION

Computer simulations of sputtering generally have used pair potentials to describe the forces between atoms.[1] Pair potential models assume that the total potential energy of a system of atoms may be expressed as a sum of two-body terms. The pair potential model has been successful in describing bulk properties such as heat of sublimation, bulk modulus, and thermodynamic equations of state.[2] This is surprising because atoms are not point particles. However plausible this may be in cases where the atomic density is macroscopically uniform, the pair potential approximation is rather dubious for processes that involve extreme local nonuniformity of atomic densities such as vacancy formation, surface diffusion, and atomic ejection during sputtering. Pair potential approximations are qualitative at best in other processes that involve surfaces such as fracture, surface segregation, and surface reconstruction. Attempts have been made to include electronic effects by introducing a density-dependent term to the total energy.[3,4] Since the atomic density is only unambiguously defined as an averaged quantity, this method still does not properly account for local density variations.

A simple example will illustrate the many-body forces in atomic interactions. The forces between two isolated atoms consist of the mutual repulsion of the ion cores and the attractive force of the chemical bond which depends directly on the electron distribution. Introduction of a third atom will disturb the original electron distribution and thereby change the force between the first two atoms. The extent of this many-body effect will therefore depend on the polarizability of the atoms. In particular, it will be important in metals. We can always write the total energy as a sum of pair potentials but it will not consistently describe the forces in particular atomic configurations.

This is seen when we compare a pair potential fitted to experimental bulk Cu data with a dimer potential fitted to experimental diatomic data. The bulk Cu potential has a well depth of 0.34 eV (Ref. 2) while the potential energy of a Cu dimer in vacuum has a minimum of 2.03 eV (Ref. 5). The two pair potentials are drastically different. In the case of sputtering from metals the ejection process at the surface will involve dynamical multimer atomic configurations where the many-body effect should play an important role.

To include these many-body effects, we will use the embedded-atom method (EAM) of Daw and Baskes[6] to describe atomic interactions in a molecular dynamics simulation of sputtering. Recent molecular dynamics simulation of sputtering from the (111) face of Rh single crystal employing EAM interactions compared favorably to experimental data.[7] We have simulated the sputtering of Cu single crystals by 5-keV Ar$^+$ ions in the three low-index orientations ({111}, {110}, {100}) using many-body interactions. The resulting spectra of sputtered atoms will be compared to simulations using purely two-body interactions.

## II. INTERACTION POTENTIALS

In the EAM framework, the total potential energy of a system of atoms is, in addition to the usual pairwise sum of pair interactions, a sum over each atomic site $i$ of an embedding function that is a function only of the unperturbed electron density at each site:

$$E=\sum_i\left[F_i\Big(\sum_{j\neq i}\rho_{ij}\Big)+\frac{1}{2}\sum_{j\neq i}\phi_{ij}\right]. \tag{1}$$

Here $E$ is the total potential energy, $F$ is the embedding function, $\phi$ is a purely repulsive pair interaction, and $\rho$ is the free-atom electron density (Fig. 1). Furthermore the embedding function depends only on the atomic species in question. This description includes many-body effects which are not well understood in sputtering processes. Since the electron density at each atomic site may be unambiguously defined and the resulting force expressed for each atom is as simple as in the pair potential model, it is possible to incorporate EAM into our molecular dynamics sputtering code without a formidable increase in computation time.

For applications where relatively low energies ($\sim$eV) are involved, $F(\rho)$ and $\phi(r)$ may be obtained from equilibrium experimental data such as sublimation energy, elastic con-

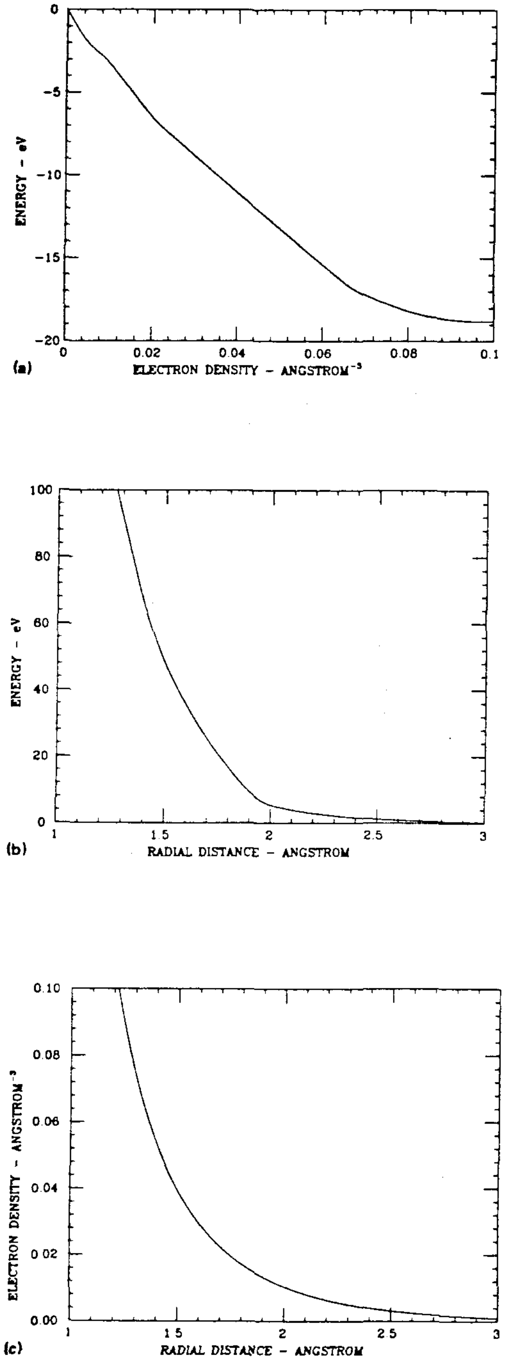

FIG. 1. (a) Embedding function, (b) EAM pair interaction, and (c) free Cu atom electron density.

stants, and vacancy formation energy.[8] However, for processes where higher energies are involved, in particular sputtering, the equilibrium experimental data are hardly adequate since these processes are in general far from equilibrium. For such applications we require the combination $F$ and $\phi$ to satisfy a semiempirical two-atom interaction $V(r)$ in addition to the experimental equilibrium data. $V(r)$ is related to $F$ and $\phi$ by

$$V(r) = 2F(\rho(r)) + \phi(r). \tag{2}$$

$V(r)$ is obtained by splining the Moliere function core to an attractive Morse potential. The Moliere screening radius was taken to be the standard Thomas–Fermi screening radius while the Morse parameters were obtained from experimental diatomic ground-state binding energy, vibrational frequency, and equilibrium separation.[5]

Rose *et al.*[9] showed that the energy equation of state $U$ may be written as a universal function of the lattice length scale $a$. The function $U$ depends on the equilibrium lattice constant, sublimation energy, and bulk modulus parametrically. In terms of $F(\rho)$ and $\phi(r)$ the energy per atom for a crystal is

$$U(a) = F\Big(\sum_i \rho(r_i)\Big) + \frac{1}{2}\sum_i \phi(r_i). \tag{3}$$

Here the sum is over all neighbors in a lattice of length scale $a$. $\rho(r)$ was taken from the Hartree–Fock–Slater calculations of Clementi and Roetti.[10] Given $\rho$, $F$ is uniquely determined by $\phi$. By parametrizing $\phi(r)$ (Ref. 8) and writing the elastic constants and vacancy formation energy in terms of $F$, $\phi$, and $\rho$,[6] we can determine $\phi(r)$ by a least-squares fit with Eq. (3) as a constraint. Once $\phi$ is determined, $F$ is obtained by varying the lattice length scale about the equilibrium value. So far $F(\rho)$ and $\phi(r)$ have been determined in their respective domains about equilibrium. For large $\rho$, we let $F$ approach a negative constant (this is rather arbitrary since $\phi$ will be much larger than $F$). The linearity of $F$ at large $\rho$ will make the interactions exclusively two body in high-energy collisions. For small $\rho$, $F$ is given by Eq. (2). The $F(\rho)$ in the two regions are joined smoothly by a spline to obtained the final $F(\rho)$. Now $\phi(r)$ is obtained for all $r$ from Eq. (2). This procedure yields a combination of $F(\rho)$ and $\phi(r)$ that fits to Eq. (2) exactly for all $r$ and to Eq. (3) exactly about the equilibrium while fitting to other experimental equilibrium data in a least-squares sense. Detailed descriptions of the embedded-atom method and fitting of embedded-atom functions to experimental data in the equilibrium region can be found in Refs. 6 and 8.

The exclusively two-body calculation employed a pair potential consisting of the same Moliere core joined by a cubic spline to an attractive Morse function. The Morse function was fitted to the elastic constant $C_{11}$ and the same universal equation of state:

$$U(a) = \frac{1}{2}\sum_i \psi(r_i). \tag{4}$$

Here the sum is over all neighbors of a lattice site as in Eq. (2) and $\psi(r)$ is a Morse function with three parameters. The parameters were adjusted to optimize the fit over a range of length scale variations. It should be noted that the pair potential used in this paper is different from the one used in a previous molecular dynamics simulation of sputtering from Cu.[11] The pair potential used here has a larger core and its Morse parameters are obtained by fitting to a universal equation of state rather than by the traditional method.[2]

## III. SIMULATION RESULTS

The sputtering yields of the EAM calculations are generally lower than that of the pair potential by a factor of 0.71 even though the surface binding energy (SBE) at the surface hole sites are slightly lower in the EAM case (Table I). Here SBE is defined as the energy required to move an atom for an unrelaxed surface hole site to infinity instantaneously. These values of SBE agree reasonably well with the calculations by Jackson.[12] The lack of correlation between the yield and SBE among the different faces is due to their crystalline nature, but this does not explain why EAM gives a lower yield. The relative yields between faces are identical for EAM and pair potential calculations. The ratios of pair potential yield to EAM yield for the three faces are all equal indicating that relative face yields are insensitive to the many-body effect.

The energy distributions of sputtered atoms (integrated over all angles) in the EAM case follow the trend of being dramatically broader while peaking at much higher energies [Figs. 2(a)–2(c)]. Similar results were also obtained by recent molecular dynamics simulations of sputtering from Rh.[7,13] The peak position in the EAM cases is higher by more than a factor of 2 as compared to the pair potential calculations although the SBE's in the two cases are identical. Theoretical[14,15] and experimental[16] studies advocate a peak position at around 0.7 of the experimental heat of sublimation. With an experimental sublimation energy of 3.54 eV for Cu, the pair potential calculation gave a lower peak position than anticipated.

The slow decay of high-energy components in the EAM case would indicate that harder collisions are taking place in the subsurface collision cascade according to Thompson's model of sputtering.[17] However, many-body effects above the surface may play a more important role in contributing to the broadening. Both the distribution broadening and higher peak positions indicate that the EAM approach affects the ejection process in a way that is more subtle than a simple rescaling of atomic binding.

TABLE I. Top: Total sputtering yields. Bottom: Binding energy at surface hole site (SBE).

| Face/yield | Pair | EAM |
|---|---|---|
| 111 | 7.66 (2.87)[a] | 5.38 (2.76)[a] |
| 110 | 2.67 | 1.95 |
| 100 | 3.69 (1.38) | 2.59 (1.33) |
| **Face/SBE (eV)** | **Pair** | **EAM** |
| 111 | 4.74 | 4.17 |
| 110 | 4.15 | 3.90 |
| 100 | 4.58 | 4.21 |

[a] These are normalized to the respective 110 face yields.

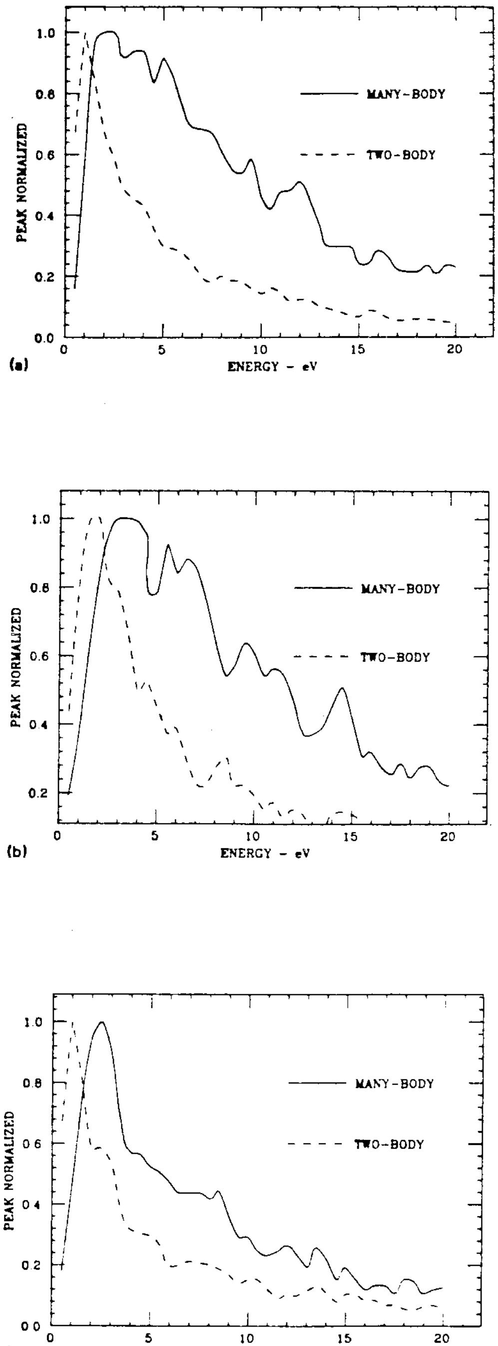

FIG. 2. (a) Energy distribution of sputtered atoms for {111} face, (b) energy distribution of sputtered atoms for {110} face, and (c) energy distribution of sputtered atoms for {100} face.

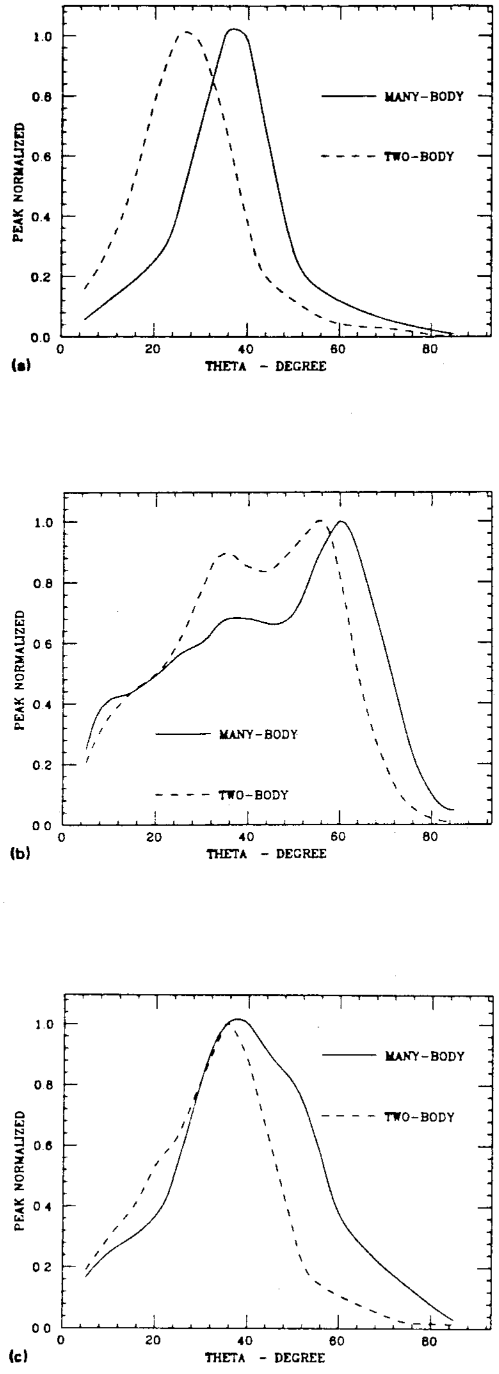

FIG. 3. (a) Polar angular distribution of sputtered atoms for {111} face, (b) polar angular distribution of sputtered atoms for {110} face, and (c) polar angular distribution of sputtered atoms for {100} face.

The differences in the polar angular distribution (integrated over all energies) of sputtered atoms between the two interactions is most notable for the {111} face and less so for the other two faces [Figs. 3(a)–3(c)]. The angular distribution peak position is 12° higher and has a much smaller central spot in the EAM case for the {111} face. The fact that large differences occurred only for the {111} face suggest a changing EAM atomic core size with atomic configuration and a smaller EAM atomic core in surface close-packed configurations.

## IV. CONCLUSION

Both the angular and energy spectra calculated with EAM for Cu follow the general trend of recent experimental data[16] and an EAM molecular dynamics simulation[7] for Rh. No attempts such as parametrizing the Thomas–Fermi screening radius have been made to reproduce experimental Cu sputtering data. The important result is that experimental bulk metal data alone are not sufficient to determine interaction potentials for sputtering simulations. Two different rational approaches to describing the dynamics of sputtering capable of reproducing experimental bulk metal properties gave very different spectra of sputtered atoms. Conversely, the detailed data on the energy and angular distributions of sputtered atoms (such as Ref. 16) may contain a great deal of information on atomic interactions at the surfaces of solids and liquids. This is contrary to the commonly held view that a simple effective surface binding energy suffices in describing sputtering phenomena.[18] We make no claim that the EAM approach is the best choice for a comprehensive theory; however, its predictions are distinctively different than those from pair potentials, which indicates that sputtering predictions are sensitive to details of the atomic interaction used.

## ACKNOWLEDGMENT

This work was supported in part by the National Science Foundation, Grant No. DMR84-21119.

[1] D. E. Harrison, Jr., Radiat. Eff. **70**, 1 (1983).

[2] L. A. Girifalco and V. G. Weizer, Phys. Rev. **114**, 687 (1959).

[3] R. A. Johnson, Phys. Rev. B **6**, 2094 (1972).

[4] M. I. Baskes and C. F. Melius, Phys. Rev. B **20**, 3197 (1979).

[5] K. P. Huber and G. Herzberg, *Molecular Spectra and Molecular Structure* (Van Nostrand Reinhold, New York, 1979).

[6] M. S. Daw and M. I. Baskes, Phys. Rev. B **29**, 6443 (1984).

[7] B. J. Garrison, N. Winograd, D. M. Deaven, C. T. Reimann, D. Y. Lo, T. A. Tombrello, D. E. Harrison, Jr., and M. H. Shapiro, Phys. Rev. B (submitted).

[8] S. M. Foiles, M. I. Baskes, and M. S. Daw, Phys. Rev. B **33**, 7983 (1986).

[9] J. H. Rose, J. R. Smith, F. Guinea, and J. Ferrante, Phys. Rev. B **29**, 2963 (1984).

[10] E. Clementi and C. Roetti, *Atomic Data and Nuclear Data Tables* (Academic, New York, 1974).

[11] M. H. Shapiro, P. K. Haff, T. A. Tombrello, D. E. Harrison, Jr., and R. P. Webb, Radiat. Eff. **89**, 234 (1985).

[12] D. P. Jackson, Radiat. Eff. **18**, 185 (1973).

[13] B. J. Garrison, N. Winograd, C. T. Reimann, and D. E. Harrison, Jr., Phys. Rev. B **36**, 3516 (1987).

[14] B. J. Garrison, N. Winograd, D. Y. Lo, T. A. Tombrello, M. H. Shapiro, and D. E. Harrison, Jr., Surf. Sci. **180**, L129 (1987).

[15] R. Kelly, Nucl. Instrum. Methods B **18**, 388 (1987).

[16] J. P. Baxter, G. A. Schick, J. Singh, P. H. Kobrin, and N. Winograd, J. Vac. Sci. Technol. A **4**, 1218 (1986).

[17] M. W. Thompson, Philos. Mag. **19**, 377 (1968).

[18] P. Sigmund, Phys. Rev. **184**, 383 (1969).

# MOLECULAR DYNAMICS SIMULATION OF SPUTTERING WITH MANY-BODY INTERACTIONS[†]

Davy Y. Lo*, Tom A. Tombrello*, Mark H. Shapiro*, and Don E. Harrison Jr.**
*Division of Physics, Mathematics, and Astronomy, 200-36 California Institute of Technology, Pasadena, CA 91125
**Department of Physics, US Naval Postgraduate School, Monterey, CA 93940

## ABSTRACT

Many-body forces obtained by the Embedded-Atom Method (EAM) [4] are incorporated into the description of low energy collisions and surface ejection processes in molecular dynamics simulations of sputtering from metal targets. Bombardments of small, single crystal Cu targets (400-500 atoms) in three different orientations ({100}, {110}, {111}) by 5 keV $Ar^+$ ions have been simulated. The results are compared to simulations using purely pair-wise additive interactions. Significant differences in the spectra of ejected atoms are found.

## Introduction

Computer simulations of sputtering generally have used pair potentials to describe the forces between atoms [1]. Pair potential models assume that the total potential energy of a system of atoms may be expressed as a sum of two-body terms. The pair potential model has been successful in describing bulk properties such as heat of sublimation, bulk modulus, and thermodynamic equations of state [2]. This is surprising because atoms are not point particles. However plausible this may be in cases where the atomic density is macroscopically uniform, the pair potential approximation is rather dubious for processes that involve extreme local non-uniformity of atomic densities such as vacancy formation, surface diffusion, and atomic ejection during sputtering.

A simple example will illustrate the many-body forces in atomic interactions. The forces between two isolated atoms consist of the mutual repulsion of the ion cores and the attractive force of the chemical bond which depends directly on the electron distribution. Introduction of a third atom will disturb the original electron distribution and thereby change the force between the first two atoms. The extent of this many-body effect will therefore depend on the polarizability of the atoms. In particular, it will be important in metals. We can always write the total energy as a sum of pair potentials, but it will not consistently describe the forces in particular atomic configurations. This is seen when we compare a pair potential fitted to experimental bulk Cu data with a dimer potential fitted to experimental diatomic data (figure1). The bulk Cu potential has a well depth of .34 eV [2] while the potential energy of a Cu dimer in vacuum has a minimum of 2.4 eV [3]. The two pair potentials are drastically different. In the case of sputtering from metals, the ejection process at the surface will involve dynamical multimer atomic configurations where the many-body effect should play an important role. The inability of pair potentials to describe bulk and multimer energetics is also a drawback in multimer ejection studies.

To include these many-body effects, we will use the Embedded- Atom Method (EAM) of Daw and Baskes [4] to describe atomic interactions in a molecular dynamics simulation of sputtering. Recent molecular dynamics simulation of sputtering from the (111) face of Rh single crystal employing EAM interactions compared favorably to experimental data [5]. We have simulated the sputtering of Cu single crystals by 5 keV $Ar^+$ ions in the three low index orientations ({111}, {110}, {100}) using many-body interactions. The resulting spectra of sputtered atoms will be compared to simulations using purely two body interactions.

Mat. Res. Soc. Symp. Proc. Vol. 100 ©1988 Materials Research Society

† Supported in part by the National Science Foundation [DMR84-21119]

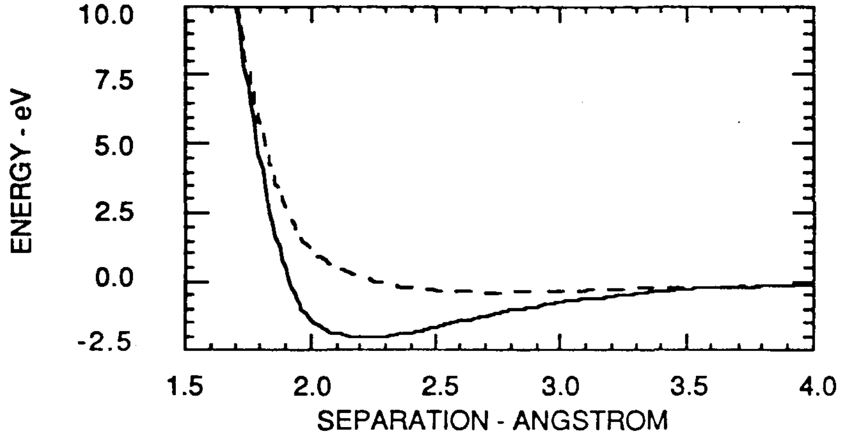

**Figure 1** - Pair potential for the bulk (solid line) as compared to that of a gaseous diatomic molecule (dashed line)

### Interaction Potentials

In the EAM framework, the total potential energy of a system of atoms is, in addition to the usual pair-wise sum of pair interactions, a sum over each atomic site i of an embedding function that is a function only of the unperturbed electron density at each site:

$$E = \Sigma_i [F(\Sigma_{j \neq i} \rho_{ij}) + \tfrac{1}{2}\Sigma_{j \neq i} \phi_{ij}] \tag{1}$$

Here E is the total potential energy, F is the embedding function, $\phi$ is a purely repulsive pair interaction, and $\rho$ is the free atom electron density. Furthermore the embedding function depends only on the atomic species in question. This description includes many-body effects which are not well understood in sputtering processes. Since the electron density at each atomic site may be unambiguously defined, and the resulting force expression for each atom is as simple as in the pair potential model; it is possible to incorporate EAM into our molecular dynamics sputtering code without a formidable increase in computation time.

For applications where relatively low energies (~eV) are involved, $F(\rho)$ and $\phi(r)$ may be obtained from equilibrium experimental data such as energy equation of state, elastic constants, and vacancy formation energy [6]. Detailed descriptions of the embedded-atom method and fitting of embedded-atom functions to experimental data in the equilibrium region can be found in references [4] and [6]. However for processes where atomic densities are far from equilibrium, in particular sputtering, the equilibrium experimental data are hardly adequate. For sputtering applications we require the EAM interaction to agree with a Moliere potential description of high energy collisions while being consistent with experimental dimer data in the gaseous regime. This is accomplished by requiring the combination F and $\phi$ to satisfy a semi-empirical dimer interaction $\psi(r)$ in addition to the experimental equilibrium data. $\psi(r)$ is related to F and $\phi$ by:

$$\psi(r) = 2F(\rho(r)) + \phi(r) \qquad (2)$$

$\psi(r)$ is obtained by splining a Moliere function core to an attractive Morse potential. The Moliere screening radius was taken to be the standard Thomas-Fermi screening radius while the Morse parameters were obtained from experimental diatomic ground state binding energy, vibrational frequency, and equilibrium separation [3] (figure 1).

The exclusively two-body calculation employed an atom-atom pair potential consisting of the same Moliere core joined by a cubic spline to an attractive Morse function. The Morse function was fitted to the bulk modulus and the same energy equation of state.

A standard Moliere pair potential was used for the Ar-Cu interaction in both the EAM and two-body calculations.

### Simulation Results

The sputtering yields of the EAM calculations are generally lower than that of the pair potential by a factor of .71 even though the surface binding energy (SBE) at the surface hole sites are similar in the two cases (table 1). Here SBE is defined as the energy required to remove an atom from an surface hole site to infinity instantaneously (fast removal is more relevant considering a sputtering time scale of $10^{-15}$ s). Surface relaxation has been neglected since it does not affect SBE to any degree significant to sputtering [7]. These values of SBE agree reasonably well with the calculations by Jackson [7]. The lack of correlation between the yield and SBE among the different faces is due to their crystalline nature but this does not explain why EAM gives a lower yield. The relative yields between faces are identical for EAM and pair potential calculations. The ratio of pair potential yield to EAM yield for the three faces are all equal indicating that relative face yields are insensitive to the the many-body effect.

**Table I** - Total sputtering yields and binding energy at surface hole sites.

| Face/Yield | PAIR | EAM |
|---|---|---|
| 111 | 7.66 (2.87)* | 5.38 (2.76)* |
| 110 | 2.67 | 1.95 |
| 100 | 3.69 (1.38) | 2.59 (1.33) |

| Face/SBE (eV) | PAIR | EAM |
|---|---|---|
| 111 | 4.74 | 4.17 |
| 110 | 4.15 | 3.90 |
| 100 | 4.58 | 4.21 |

* These are normalized to the respective 110 face yields

The energy distributions of sputtered atoms (integrated over all angles) in the EAM case follow the trend of being dramatically broader while peaking at much higher energies (figure 2). Similar results were also obtained by recent molecular dynamics simulations of sputtering from Rh [5,8]. The peak position in the EAM cases is higher by more than a factor of two as compared to the pair potential calculations, although the SBE in the two cases are similar. Theoretical [9,10] and experimental [11] studies advocate a peak position at around .7 of the experimental heat of sublimation. With an experimental sublimation energy of 3.54 eV for Cu, the pair potential calculation gave a lower peak position than anticipated. The slow decay of high energy components in the EAM case would indicate that softer collisions are taking place in the sub-surface collision cascade according to Thompson's model of sputtering [12]. However, many-body effects above the surface may play a more important role in contributing to the broadening.

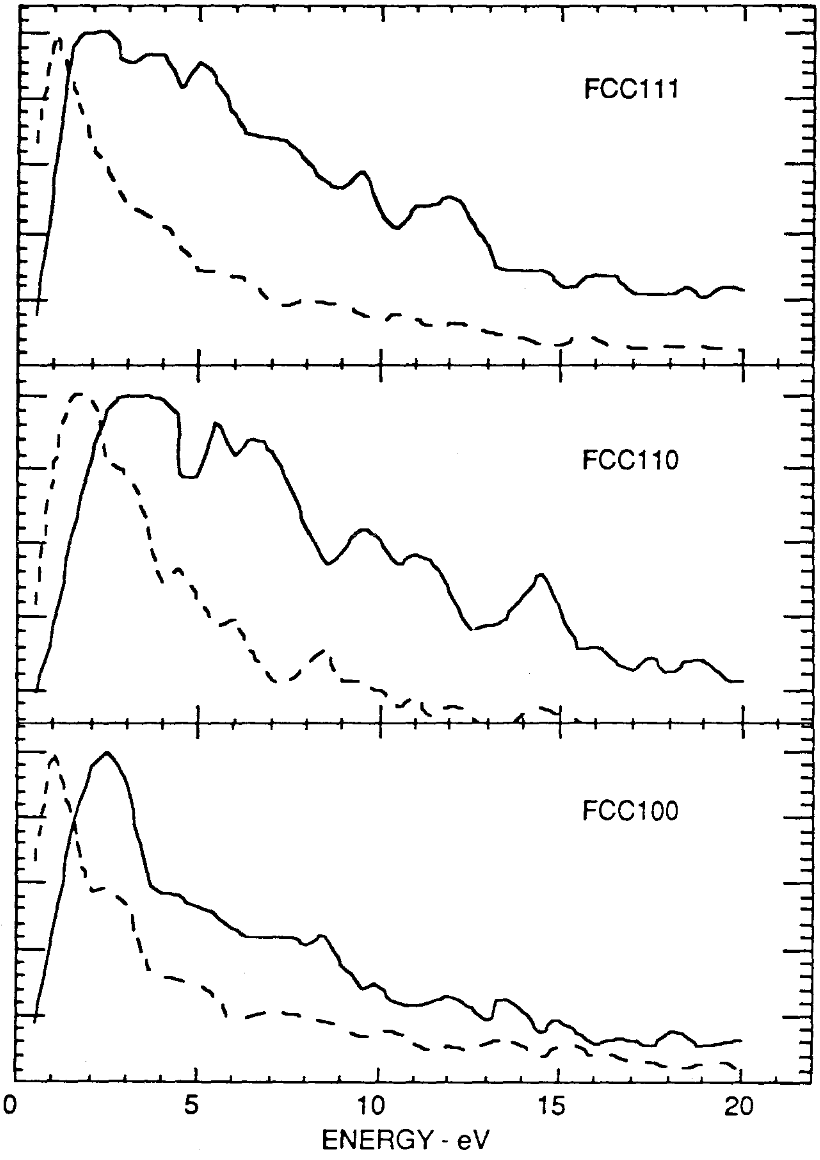

**Figure 2** - Energy distribution resulting from EAM (solid line) and pair potential (dash line) calculations. Each frame is peak normalized.

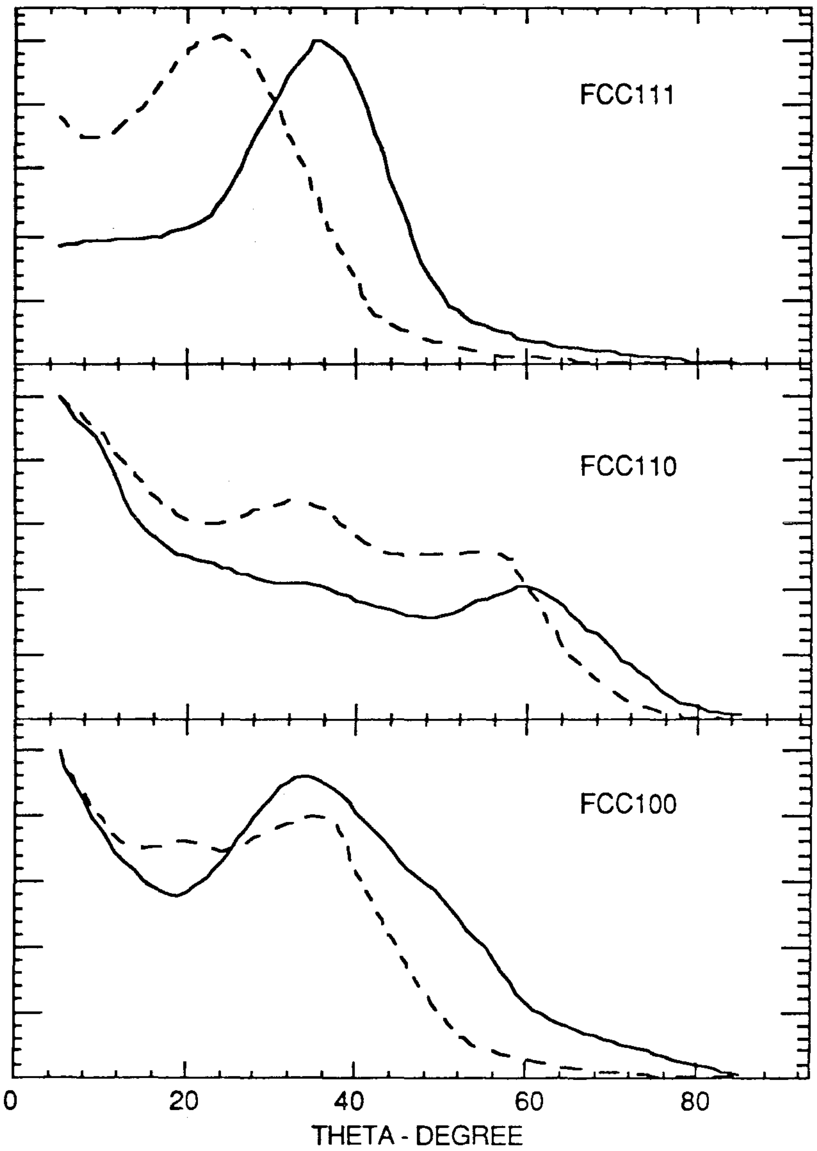

**Figure 3** - Polar angle distribution (constant solid angle) resulting from EAM (solid line) and pair potential (dash line) calculations. Each frame is peak normalized.

The difference in the polar angular distribution (integrated over all energies) of sputtered atoms between the two interactions is most notable for the {111} face and less so for the other two faces (figure 3). The angular distribution peak position is $10^0$ higher and has a much smaller central spot in the EAM case for the {111} face. The fact that large differences occurred only for the {111} face suggests a changing EAM atomic core size with atomic configuration and a smaller EAM atomic core in surface close-packed configurations.

Differences in the calculated sputtering spectra may not be attributed to a single feature of the EAM interaction. However, we think its description of the dynamics above the surface is an important one. Since the EAM interaction includes experimental dimer data, it will require more energy for an atom interacting, with dangling atoms above the disturbed surface to escape even though the SBE is comparable to the pair potential case. This is a plausible explanation for the differences in the sputtering yields and spectra calculated.

## Conclusion

Both the angular and energy spectra calculated with EAM for Cu follow the general trend of recent experimental data [11] and an EAM molecular dynamics simulation [5] for Rh. No attempts such as parametrizing the Thomas-Fermi screening radius have been made to reproduce experimental Cu sputtering data. The important result is that experimental bulk metal data alone are not sufficient to determine interaction potentials for sputtering simulations. Two different rational approaches to describing the dynamics of sputtering capable of reproducing experimental bulk metal properties gave very different spectra of sputtered atoms. Conversely, the detailed data on the energy and angular distributions of sputtered atoms (such as reference [11]) may contain a great deal of information on atomic interactions at the surfaces of solids and liquids. This is contrary to the commonly held view that a simple effective surface binding energy suffices in describing sputtering phenomena [13]. We make no claim that the EAM approach is the best choice for a comprehensive theory; however, its predictions are distinctively different from those of pair potentials, which indicates that sputtering predictions are sensitive to details of the atomic interaction used.

## References

1. D. E. Harrison, Jr., Radiat. Eff. **70**, 1 (1983).
2. L. A. Girifalco and V. G. Weizer, Phys. Rev. **114**, 687 (1959).
3. K. P. Huber and G. Herzberg, Molecular Spectra and Molecular Structure, (Van Nostrand Reinhold Co., New York, 1492).
4. M. S. Daw and M. I. Baskes, Phys. Rev. **B 29**, 6443 (1984).
5. B. J. Garrison, N. Winograd, D. M. Deaven, C. T. Reimann, D. Y. Lo, T. A. Tombrello, D. E. Harrison, Jr., and M. H. Shapiro, presented at SIMS IV, France, 1987.
6. S. M. Foiles, M. I. Baskes, and M. S. Daw, Phys. Rev. **B 33**, 7983 (1986).
7. D. P. Jackson, Radiat. Eff. **18**, 185 (1973).
8. B. J. Garrison, N. Winograd, C. T. Reimann, and D. E. Harrison, Jr., Phys. Rev. **B36**, 3516 (1987).
9. B. J. Garrison, N. Winograd, D. Y. Lo, T. A. Tombrello, M. H. Shapiro, and D. E. Harrison, Jr., Surf. Sci. **180**, L129 (1987).
10. R. Kelly, Nucl. Instr. and Meth. **B18**, 388 (1987).
11. J. P. Baxter, G. A. Schick, J. Singh, P. H. Kobrin, and N. Winograd, J. Vac. Sci. Tech. **4**, 1218 (1986).
12. M. W. Thompson, Phil. Mag. **18**, 377 (1968).
13. P. Sigmund, Phys. Rev. **184**, 383 (1969).